

AD-774 828

WEAR, FRICTION AND THERMAL FATIGUE OF  
GUN BARREL MATERIALS

W. M. Robertson

Rockwell International Corporation

Prepared for:

Army Weapons Command

21 December 1973

DISTRIBUTED BY:



National Technical Information Service  
U. S. DEPARTMENT OF COMMERCE  
5285 Port Royal Road, Springfield Va. 22151

AD-774828

SC558.4FR

WEAR, FRICTION AND THERMAL FATIGUE  
OF GUN BARREL MATERIALS  
FINAL REPORT

23 May 1973 thru 31 December 1973

General Order No. 558

Contract DAAF07-73-C-0582

Prepared for:

Department of the Army  
U.S. Army Weapons Command  
Watervliet Arsenal  
Watervliet, New York 12189

by:

W. M. Robertson  
Principal Investigator

Approved:

H. L. Marcus

H. L. Marcus  
Program Manager  
Science Center

Reproduced by  
NATIONAL TECHNICAL  
INFORMATION SERVICE  
U S Department of Commerce  
Springfield VA 22151



Science Center  
Rockwell International

170

## TABLE OF CONTENTS

	<u>Page</u>
List of Tables. . . . .	iii
List of Figures . . . . .	iv
Abstract. . . . .	1
1. Introduction and Objectives. . . . .	2
2. Test Materials and Experimental Procedure. . . . .	4
2.1 Coating, Liner and Substrate Materials . . . . .	4
2.2 Specimen geometry and Preparation . . . . .	8
2.2.1 Thermal Fatigue Specimen . . . . .	8
2.2.2 Plating Procedures . . . . .	9
2.3 Thermal Fatigue Testing . . . . .	12
2.3.1 Temperature Measurement and Control . . . . .	13
2.3.2 Strain measurement and Control . . . . .	16
2.3.3 Stress Measurement . . . . .	18
2.3.4 Failure criteria . . . . .	19
2.3.5 Selection of Temperature Cycling Ranges. . . . .	19
2.4 Materials Characterization. . . . .	21
2.5 High Temperature Mechanical Properties. . . . .	23
3. Results. . . . .	24
3.1 Test Specimens. . . . .	24
3.2 Initial Specimen Characterization . . . . .	27
3.2.1 Steel and Ta-10% W . . . . .	27
3.2.2 Plating Materials . . . . .	28
3.2.2.1 SEM & TEM Observations. . . . .	28
3.2.2.2 Auger Measurements. . . . .	29
3.3 High Temperature Mechanical Properties. . . . .	30
3.4 Thermal Fatigue Tests . . . . .	33
3.4.1 Thermal Fatigue Parameters . . . . .	36
3.4.2 Bare Steel Microscopic Results . . . . .	42
3.4.3 Chromium Plated Steel Microscopic Results. . . . .	45
3.4.4 Co/Cr Plated Steel Microscopic Results . . . . .	57
3.4.5 Tantalum-10 Tungsten Thermal Fatigue Tests . . . . .	64

## Table of Contents - continued.

	Page
4. Discussion . . . . .	68
4.1 Chromium Plate on Steel. . . . .	68
4.1.1 Observations for Cr plate in gun steel. . . . .	68
4.1.2 Cr plate analysis suggestions and future work .	70
4.2 Cobalt-Chromium plate on steel . . . . .	73
4.2.1 Observations on the Cr/Co plate combination . .	73
4.2.2 Cr/Co plate analysis suggestions and future work . . . . .	76
4.3 Test interpretation and Failure procedures . . . . .	79
5. Conclusions . . . . .	83
5.1 Bare Steel . . . . .	83
5.2 Chromium plate on Steel. . . . .	83
5.3 Chromium hardened cobalt plate on Steel. . . . .	84

## LIST OF TABLES

<u>Table</u>		<u>Page</u>
I	Steel Composition, Weight Percent	6
II	Composition of Ta-10W Alloy	7
III	Specimen Summary and Nominal Test Conditions	25, 26
IV	Iron Contamination of Chromium Plate	31
V	Flow Stress of Gun Steel	32
VI	Identification of Test Conditions for Specimens	34
VII	Test Parameters for Steel Thermal Fatigue Tests	37, 38 39, 40
VIII	Summary of Near Cr/Steel Interface Cracking and Deformation	53
IX	Test Parameters for Tantalum-10 Tungsten Thermal Fatigue Tests	66

## LIST OF FIGURES

<u>FIGURE</u>		<u>PAGE</u>
1	Steel thermal fatigue specimen	8
2	Tantalum-10% tungsten thermal fatigue specimen.	8
3	Thermal fatigue cycles for chromium plated specimen BB. a) Zero load (free expansion) cycle. b) Cycle showing load imposed to constrain diameter.	16
4	Stress versus temperature for specimen BB for the constrained thermal fatigue cycle of Fig. 3b.	20
5	Thermal fatigue cycle for bare specimen BK cycled above $A_1$ and below $M_s$ .	20
6	Optical micrographs of etched sections of a) as received gun steel, b) heated treated 4340 steel.	28
7	Transmission electron micrograph of as received gun steel.	28
8	Optical micrographs showing structure of as received Ta-10% W bar: a) section through bar; b) section along bar, arrow in direction of bar axis.	28
9	Scanning electron micrographs of electropolished sections of specimen BF, a Cr/Co plated specimen with no $Al_2O_3$ in the cobalt: a), b) as plated; c) after bakeout. Cr on top.	28
10	Scanning electron micrographs of electropolished sections of a), b) Cr/Co plated specimen, cobalt containing $Al_2O_3$ , specimen not baked, c), d) Cr plated steel specimen, baked. Cr on top.	28
11	Transmission electron micrograph of Co layer for Co/Cr plated specimen BE.	30
12	Dark field transmission electron micrograph of Co layer for Co/Cr plated specimen BE. Arrow at illuminated $Al_2O_3$ particles.	30
13	Flow stress versus strain rate at various temperatures for gun steel.	30
14	Scanning electron micrographs of sandblasted structure on the surface of specimen BK.	42

<u>FIGURE</u>		<u>PAGE</u>
15	Microstructure of specimen BV. a) Optical micrograph of inner surface; b) transmission micrograph of bulk structure; c) dark field view of carbide particle; d) diffraction pattern of area in b).	42
16	Microstructure of specimen BJ. Optical micrographs of a) outer surface; b) inner surface; c) transmission micrograph of bulk area; d) diffraction pattern of area c).	44
17	Optical micrographs of specimen BW. a) Outer surface; b) inner surface.	44
18	Scanning electron micrographs of the fracture surface of specimen BJ.	44
19	Microstructure of Specimen BK. a) Optical micrograph of bulk; b) transmission micrograph of bulk; c) diffraction pattern of area b).	44
20	Optical micrographs of specimen AY: a) away from hottest zone; b) center of hottest zone.	44
21	Optical micrographs of specimen BX: a) outer surface; b) inner surface.	44
22	Scanning electron micrographs of inner surface of specimen BK showing cracks and surface oxide particles.	46
23	Scanning electron micrographs of altered zone in the steel at chromium/gun steel interface seen in electropolished sections: a) For specimen BH, arrow at deepest penetration distance of zone of heavy etch; b) high magnification of region in (a), arrow at etch structure typical of bulk material; c) for specimen AU, arrow at deepest penetration distance of zone of heavy etch; d) high magnification of region in (c) showing heavily etched altered zone. Chromium at top.	48
24	Scanning electron micrographs of chromium/gun steel interface seen in electropolished sections of specimen AQ, cycled only below $A_1$ . No altered zone is observable in the steel at the interface. Chromium at top.	48
25	Scanning electron micrographs of chromium/gun steel interface seen in electropolished sections: a) & b) For specimen BL showing slight increase in depth of altered zone over that for specimen BH cycled for 10 cycles over the same temperature range; c) & d) showing expansion of the altered zone at point of passage of crack in the chromium into the gun steel. Arrow in (d) at micro-cracked region having increased chromium content.	48

<u>FIGURE</u>		<u>PAGE</u>
26	Transmission electron micrograph of chromium layer near to chromium/gun steel interface of specimen BL. The lath structure is apparently a single crystal of $\text{Cr}_7\text{C}_3$ .	50
27	Dark field transmission electron micrograph of region shown in Fig. 26 taken in matrix reflection of $\text{Cr}_7\text{C}_3$ .	50
28	a) Electron diffraction pattern of region shown in Fig. 26. In addition to the polycrystalline rings the matrix reflections of the crystal illuminated in Fig. 27 are visible. b) Comparison electron diffraction pattern taken in the Cr layer near the Cr/Co interface of specimen BR.	50
29	Transmission electron micrographs of gun steel comparing the steel near the steel/Cr interface of specimen BL (a) to that for thermally fatigued unplated gun steel specimen BG (b). Precipitate density in (a) is significantly decreased.	50
30	Electron diffraction patterns corresponding to the micrograph regions in Fig. 29: a) specimen BL; b) specimen BG.	50
31	Scanning electron micrographs of electropolished section of specimen BG showing apparent microcracking in altered zone not associated with Cr cracking. Arrow in (a) at region of high magnification in (b). Chromium at top.	52
32	Scanning electron micrographs of sections of fracture surfaces of specimen AU showing microcracked region in steel at Cr/steel interface: a) & b) region one, arrows in (b) define zone; c) & d) region two, arrows in (d) define zone.	52
33	Scanning electron micrographs of section of fracture surface of specimen BB. Arrows at Cr/steel interface. Cr on top.	52
34	Scanning electron micrographs of electropolished section of specimen AV. Connection between sub Cr plastic deformation zones can be seen associated with cracks in the Cr plate, blunted in the steel. Cr on top.	54
35	Scanning electron micrographs of electropolished section of specimen AU showing crack propagation into the steel after 25 test cycles. Cr on top.	54
36	Scanning electron micrograph of electropolished section of specimen BI showing crack blunting at Cr/steel interface. Cr on top.	54

<u>FIGURE</u>		<u>PAGE</u>
37	Scanning electron micrographs of electropolished section of specimen BL. In addition to the heavy deformation in the steel a pinch of steel can be seen in the Cr plate. Cr on top.	54
38	Scanning electron micrographs of electropolished section of specimen AQ. Crack propagation through the Cr/steel interface is seen for this test condition and little associated deformation is noted. Cr on top.	54
39	Scanning electron micrographs of electropolished section of specimen BB. No crack propagation through the interface is observed. Significant undermining is associated with crack blunting. Cr on top.	54
40	Scanning electron micrographs of electropolished section of specimen AA. No crack propagation is observed through the interface and also no associated deformation is detectable. Cr on top.	54
41	Montage of scanning electron micrographs of surface of Cr plate for specimen AV. Load axis is vertical.	56
42	Montage of scanning electron micrographs of surface of Cr plate for specimen BH. Load axis is vertical.	56
43	Montage of scanning electron micrographs of surface of Cr plate for specimen A. Load axis is vertical.	56
44	Scanning electron micrographs of the fracture surface of specimen AU. Cracking of the inside surface is seen in b, c and d.	56
45	Scanning electron micrograph of a segment of the fracture surface of specimen AU showing axial cracking in the Cr plate.	56
46	Scanning electron micrographs of the surface fracture and electropolished section of specimen AA. Crack pattern is essentially intrinsic to the electrodeposited Cr before thermal cycling.	56
47	Scanning electron micrographs of electropolished sections of Cr layer of specimen AU. Apparent zones of deformation are seen associated with the cracks in the Cr.	56
48	Scanning electron micrographs of section of fracture surface of specimen BB. a & b show blocky appearing fracture surface possibly associated with deformation zones in the Cr. The smooth cracking in c & d may be associated with an initial through crack in the Cr.	56

<u>FIGURE</u>	<u>PAGE</u>
49 Scanning electron micrographs of electropolished sections of specimen BR.	58
50 Scanning electron micrographs of electropolished sections of specimen BS. Cracks in Cr have been folded into the Co, effectively blunting them. Cr layer on top.	60
51 Scanning electron micrographs of electropolished sections of specimen AN. An extended zone of deformation is seen in the Co at the Cr/Co interface in association with cracking through the interface. Voids have formed both ahead of the crack and in localized aggregates of $\text{Al}_2\text{O}_3$ particles. Cr uppermost.	60
52 Scanning electron micrographs of electropolished sections of specimen AN showing deformation in Co at Cr/Co interface and apparent interface debonding. Cr layer at top.	60
53 Scanning electron micrographs of electropolished sections of specimen BO for a region with low $\text{Al}_2\text{O}_3$ content in the Co at the Cr/Co interface. Deformation is seen in the Co/Cr layer at top.	60
54 Scanning electron micrographs of electropolished section of specimen BR: a) and b) at a point of high $\text{Al}_2\text{O}_3$ concentration in the Co at the Cr/Co interface. No deformation is seen in the Co. Arrow in (b) at probable site of initial crack blunting in the Cr; c) and d) intermediate $\text{Al}_2\text{O}_3$ concentration showing reduced deformation. Cr layer on top.	60
55 Scanning electron micrographs of electropolished section of specimen BR illustrating a relationship between changes in $\text{Al}_2\text{O}_3$ density, seen by banding and changes in crack propagation direction. Cr layer at top.	60
56 Scanning electron micrographs of electropolished section of specimen BR. Arrow in (a) at plane of incipient Co debonding. Cr layer on top.	62
57 Scanning electron micrographs of sections of fracture surface of specimen BS. Arrow at delamination crack in the Co in (a). Site b, c and d 180° opposite site (a) and complete Co delamination has occurred there. Arrow in (b) at plane of lower lamination.	62
58 Scanning electron micrographs of electropolished section of specimen BR illustrating void formation in the Co (a) and Cr/Co fracture surface in (b).	62

<u>FIGURE</u>		<u>PAGE</u>
59	Scanning electron micrographs of electropolished section of specimen AN illustrating void formation in the non-ultrasonically deposited dispersion hardened Co. Voids are particularly associated with $\text{Al}_2\text{O}_3$ aggregations.	62
60	Scanning electron micrographs of inclusion in Cr at initiation site of crack in Fig. 60 (a), x-ray analysis indicating the inclusion to be primarily silicon (b). The bar spectrum is the matrix, i.e., Cr and the dot spectrum is that in the region of the particle.	62
61	Scanning electron micrographs of specimen BR: a) and b) electropolished section; c) Co fracture and Co/steel delamination interface at arrow; d) Cr/Co fracture surface. Cr on top illustrates void formation.	62
62	Scanning electron micrographs of electropolished section of specimen BR at Co/steel interface. No interface degradation is noted. Co on top.	64
63	Scanning electron micrograph of electropolished section of specimen BR at Co/steel interface showing crack blunting in steel. Co on top.	64
64	Scanning electron micrographs of electropolished section and fracture surface of specimen BR at region of massive tear in the steel. Particle at arrow in (a) is silicon as shown by x-ray analysis (c).	64
65	Scanning electron micrographs of magnified region of tear in Fig. 64.	64
66	Transmission electron micrograph of Co at Co/steel interface of specimen BR.	64
67	Dark field micrograph corresponding to Fig. 66. $\text{Al}_2\text{O}_3$ particles are illuminated.	64
68	Electron diffraction patterns: a) of Co at Co/steel interface of specimen BR; b) representative for Cr for specimen BR.	64
69	Representative transmission electron micrograph of Cr on specimen BR.	64
70	Representative dark field micrograph of Cr of specimen BR showing columnar deposition structure.	64

## ABSTRACT

Thermal fatigue tests were performed on the following materials: gun steel; 4340 steel; chromium plated gun steel; gun steel plated with a composite plate of chromium over alumina dispersion hardened cobalt; 4340 steel plated with the composite chromium-cobalt plate; and tantalum-10% tungsten. Temperatures were cycled over various ranges from a minimum of 350°F to a maximum of 1535°F. The tubular test specimens were heated by induction and cooled by passing air through the tube center. Diametral strain was measured and constrained to follow a preset temperature strain relation which provided either 0.2% or 0.8% plastic compressive strain in the specimen at the maximum temperature of the cycle. Loads required to maintain the preset strain were measured and time to specimen failure was determined.

Extensive characterization of failure mechanisms of the tested materials was carried out using optical microscopy, scanning electron microscopy and transmission electron microscopy. Failure mechanisms of the plated materials were identified as being due to the following: cracking of chromium plate; crack propagation from the chromium plate into the cobalt; carbide formation at the chromium/steel interface; and tearing in the steel where a crack penetrates the chromium-steel or cobalt-steel interface. Failure in bare steel and in tantalum-10% tungsten occurred principally by cracking from the inner tube surface. The application of these results to the optimization of wear resistant coatings on gun barrels is discussed.

## 1. INTRODUCTION AND OBJECTIVES

The current U. S. Army requirement for development of higher performance gun weapons and guns with increased operational life has generated a need to improve resistance to gun bore surface erosion. For many current or proposed gun systems gun barrel bore surface erosion is or will be the limiting factor in determining gun tube life. Although the basic environmental parameters which contribute to erosion and wear, such as bore surface temperature, dynamic pressure loading and projectile impact loading, are known, the response of present or candidate gun bore materials to these conditions has not been completely characterized in a systematic way.

The objective of this effort has been to define, for three selected gun bore surface materials, the material failure mechanisms in a stringent controlled thermal fatigue environment that can be expected to determine their ultimate resistance to erosion. Furthermore the objective has been to rank the recognized failure mechanisms with respect to overall importance and to use this insight to suggest informed approaches to further optimization of the materials under consideration. The overall approach to this end has been to utilize detailed post thermal fatigue materials characterization of the selected bore surface materials. This has relied on the unique capability at the Science Center to provide controlled thermal fatigue testing of materials and an extensive array of analytic equipment for post fatigue degradation determinations. Several significant discoveries have been made in this effort which will have a substantial impact on the selection of future courses of optimization for the chromium plate gun steel combination

in current use by the U.S. Army and for the chromium/dispersion harden cobalt coating on steel under consideration. This work was accomplished under contract to Watervliet Arsenal over the period of June to December, 1973.

## 2. TEST MATERIALS AND EXPERIMENTAL PROCEDURE

### 2.1 Coating, Liner and Substrate Materials

The effect of thermal fatigue on three gun bore surface coating, or liner, materials was investigated in this study: chromium plate; a composite coating of chromium on alumina dispersion hardened cobalt; tantalum-10% tungsten alloy. Chromium plate on gun steel is the standard wear resistant coating/barrel material combination currently used by the U. S. Army. The composite coating of chromium on dispersion hardened cobalt is currently being considered and tested by Watervliet Arsenal and the tantalum-10% tungsten alloy is a potential future gun barrel liner material. Two substrate materials were utilized, gun steel and 4340 steel. The material combinations subjected to thermal fatigue environments and then characterized were as follows:

1. Gun steel
2. 4340 steel
3. Chromium plate on gun steel substrate
4. Chromium/cobalt plate on 4340 steel substrate
5. Chromium/cobalt plate on gun steel substrate
6. Tantalum-10% tungsten alloy

The impetus for thermal fatigue characterization of the steels was to establish a comparative data basis for analysis of their plated counterparts. The gun steel was obtained from Watervliet Arsenal as sections cut from gun barrel forgings. One lot of material was received in the form of rough

machined cylinders one inch in diameter by five inches long. A second lot was received as gun barrel sections of 4.1 inches (105 mm) inside diameter by 6 inches outside diameter by 6 inches long, with a wall thickness of one inch. Prior to receipt, the gun steel forgings had been austenitized for 12 hours at 1525° F, water quenched, and then tempered for 14 hours at 1055° F. The hardness (measured on the material as received) was Rockwell C 40.

The 4340 steel was obtained as 7/8 inch diameter rod, in the annealed condition. The compositions of this material and the gun steel are listed in Table I. After machining into thermal fatigue specimens, the 4340 steel was austenitized at 1500° F for an half hour, water quenched, and tempered at 900° F for one hour, to achieve a final hardness of Rockwell C 39. The tempering treatment on the 4340 steel was selected to give a final hardness comparable to that of gun steel. To determine this temperature small disk specimens were austenitized at 1500° F for one half hour, water quenched and then the separate specimens were tempered for one hour at each of the temperatures, 600, 800, 900, 1,000 and 1200° F. The 900° F temper was found to give a final hardness most nearly matching that of the gun steel.

The tantalum-10% tungsten alloy was purchased from Fansteel Metals, who sell it under the name "Fansteel-60 Metal." It was received in the form of a 0.625 inch diameter rod by 55 inches long, in the as-formed (unannealed) condition. No heat treatment or further working was done on this material except for the machining to make thermal fatigue specimens. The composition of the material is given in Table II.

Table I  
Steel Composition, Weight Percent

<u>Element</u>	<u>Gun Steel Ht. No. C439</u>	<u>4340 Steel</u>
C	0.31	0.42
Mn	0.59	0.74
P	0.008	0.008
S	0.009	0.010
Si	0.15	0.29
Ni	2.12	1.71
Cr	0.97	0.76
Mo	0.46	0.22
V	0.11	--
Cu	--	0.19

Table II

Composition of Ta-10 W Alloy

<u>Element</u>	<u>Amount</u>
	(Wt ppm, except W)
W	9.3 Wt. pct.
C	14
O	48
N	11
H	5
Cb	260
Zr	< 20
Mo	< 20
Ti	< 20
Fe	< 20
Ni	< 20
Cr	< 10
V	< 20
Co	< 20
Ta	Balance

## 2.2 Specimen Geometry and Preparation

2.2.1 The Thermal Fatigue Specimen. The basic test specimen used in this effort was a thermal fatigue specimen of a configuration compatible with the thermal fatigue test equipment available at the Science Center. The standard specimen geometry used to fatigue both the steel materials is shown in Fig. 1. For the coated steel tests the selected coating materials were simply electroplated on to steel specimens of this standard geometry. The thermal fatigue specimen used for the tantalum-10% tungsten is illustrated in Fig. 2. The differences between the two thermal fatigue specimen forms were dictated by diameter limitations on the as-received tantalum-10% tungsten material and by machining requirements set by the hardness of the tantalum alloy. The hole through the center of each specimen provides the conduit by which each is cooled for the cool down portion of each thermal cycle. Heating is accomplished by induction. The gage section of the two specimen geometries is identical: it consists of a hollow tube of wall thickness 0.025 inch with outside diameter 0.25 inch. Considerable care was taken to ensure that the tube wall thickness was always uniform around the specimen circumference. The steel specimen geometry provides a larger end diameter which is internally threaded to transmit the load from the test machine to the specimen. Fabrication of this specimen requires a starting rod of about 7/8 inches in diameter. The tantalum-10% tungsten specimen geometry has a smaller end diameter than the steel specimen, and the mounting is externally threaded. This alloy is quite difficult to machine. By using a smaller specimen end, it was possible to start with a rod only 5/8 inches in diameter and reduce the required machining. Steel loading fixtures were designed and fabricated

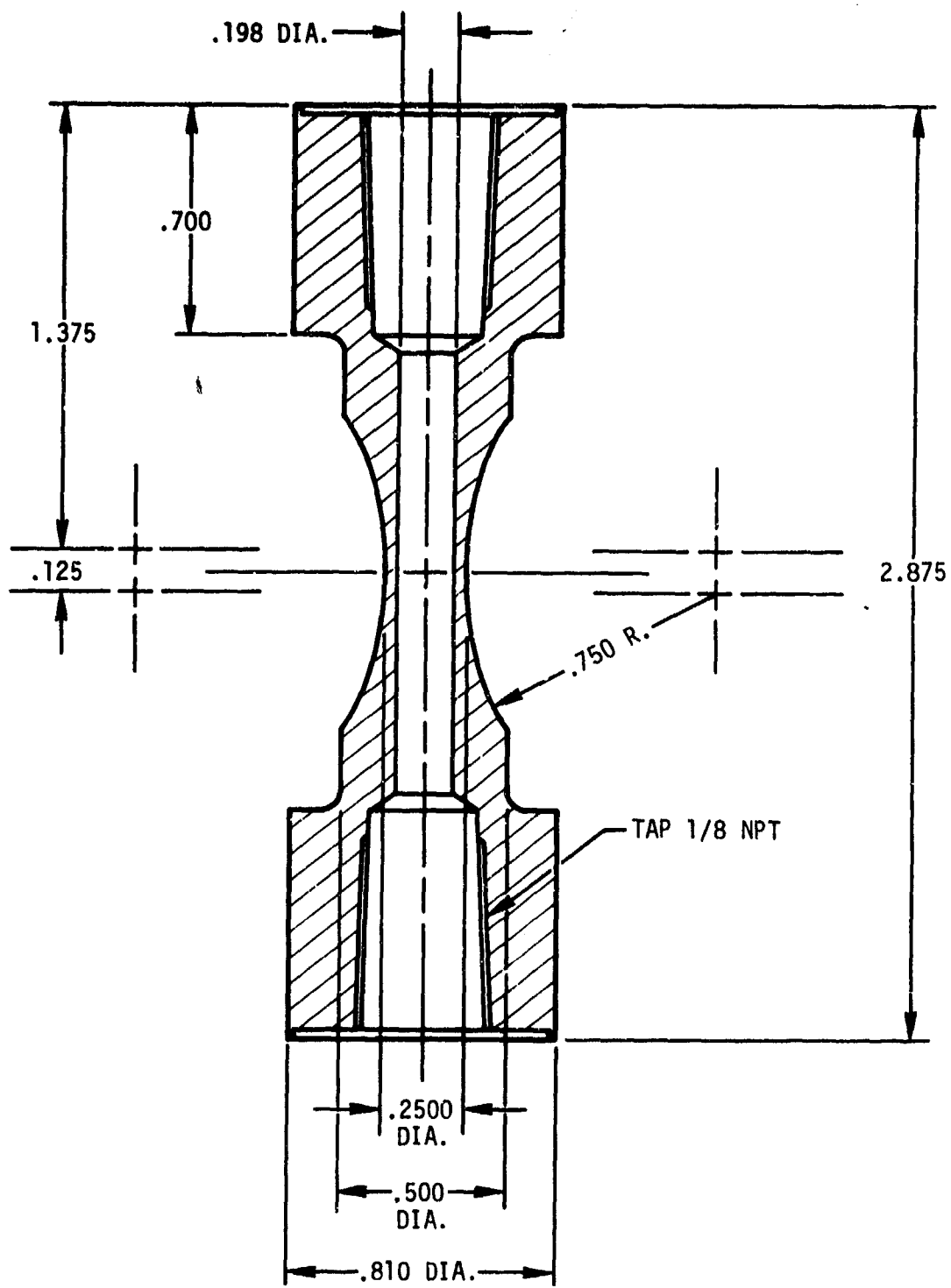


Fig. 1 Steel thermal fatigue specimen.

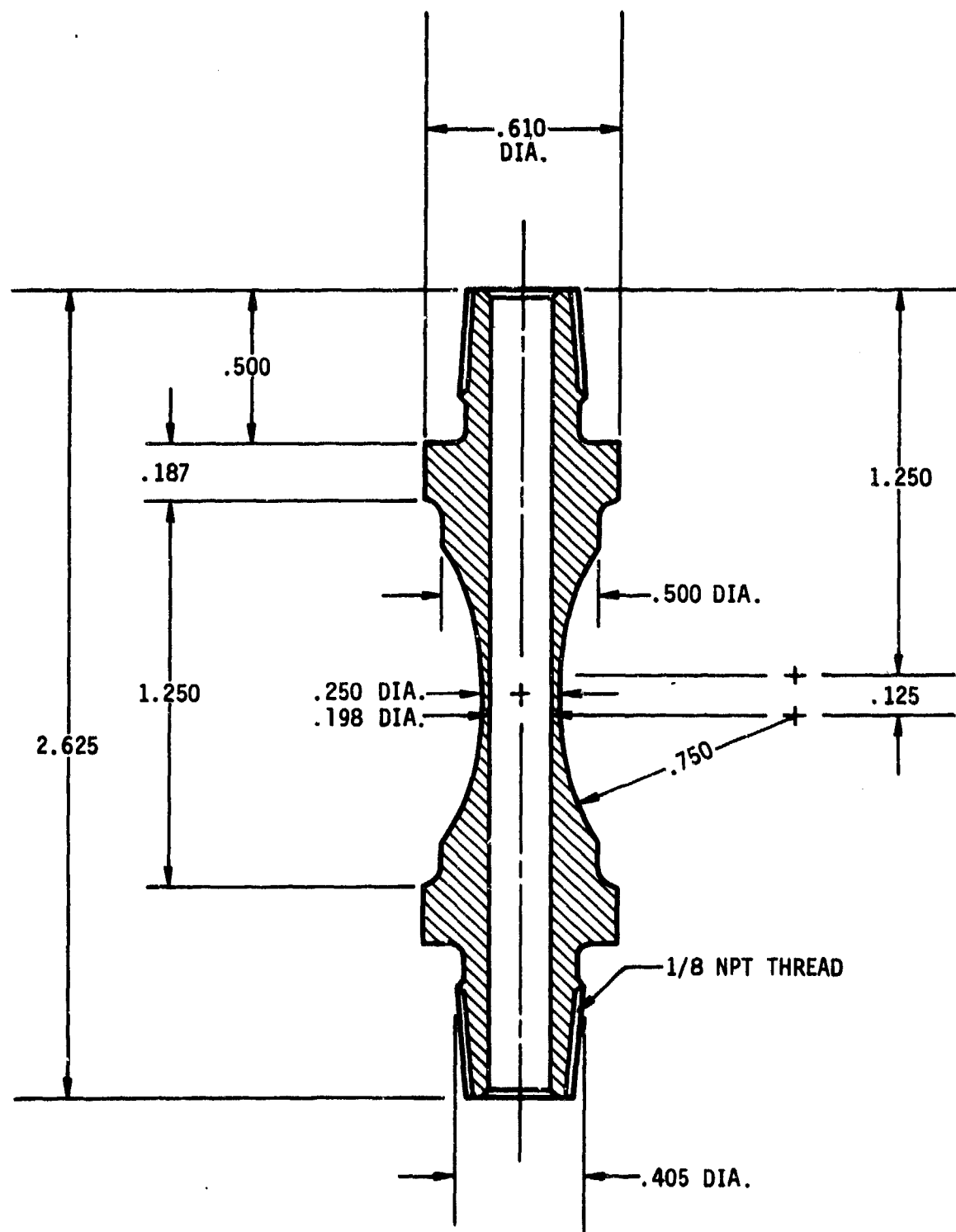


Fig. 2 Tantalum-10% tungsten thermal fatigue specimen.

for the tantalum-10% tungsten specimens to match the different specimen geometry to the load train of the testing machine. Since the thermal fatigue specimens are required to support both tensile and compressive loads during the thermal cycling, it was essential to design the specimen ends and loading train so no hysteresis or "slop" could occur on cycling from tension to compression.

2.2.2 Plating Procedures. To provide thermal fatigue test specimens in the plated steel combinations selected, specimens of gun steel and 4340 steel were electroplated with chromium or with a composite plate of chromium over alumina-dispersion hardened cobalt. The plating procedures utilized were more or less consistent with the plating practices for these materials used at Watervliet Arsenal. To apply the chromium plate to steel the following procedure was used:

1. The ends of the steel thermal fatigue specimen were masked off with a non-conducting lacquer.
2. The specimen was electropolished for 10 minutes at 2 amps per square inch (anodic) in a solution of 50 volume percent  $H_2SO_4$  and 50 volume percent  $H_3PO_4$  at 110° F.
3. The specimen was rinsed with water and transferred quickly to a conventional chromium bath with a composition of chromic anhydride ( $CrO_3$ ) at 33 ounces per gallon, sulfuric acid at 0.33 ounces per gallon and the remainder water, with a Baume density scale reading of 21.5 at room temperature.
4. The specimen was reverse-etched at 2 amps per square inch for 2 minutes at 130° F.

5. The specimen was plated (cathodic) at 2 amps per square inch for approximately 4½ hours at 130° F to achieve 0.005 inch thickness of chromium deposit.
6. The specimen was post-heat-treated at 750° F for 4 hours in air to remove hydrogen.

The procedure used to produce the composite cobalt ( $Al_2O_3$ ) chromium plating is as follows:

Steps 1 through 3 of the chromium plating procedure were followed.

4. The steel specimen was reverse etched at 2 amps per square inch for 1 minute at 130° F in the chromium solution.
5. The specimen was water rinsed and then immersed in an activating solution of 15%  $H_2SO_4$  in water (at room temperature) for 30 seconds.
6. The specimen was quickly transferred to a cobalt plating bath with the composition cobalt sulfate,  $CoSO_4 \cdot 6H_2O$ , 250 g/l; cobalt chloride,  $CoCl_2 \cdot 6H_2O$ , 40 g/l; boric acid, 35 g/l; pH, 3 to 4. Plating is done for two hours at 130° F at a current density of 50 amps per square foot.
7. Alon C powder, produced by Cobot Corporation, was used as a source of aluminum oxide to provide dispersion hardening of the cobalt. To obtain the desired aluminum oxide dispersion in the electrodeposit, aluminum oxide powder was dispersed in the bath at a concentration of 35 grams liter of electrolyte. The cobalt plating bath was prepared by mixing the above chemicals in distilled water and then by dummying for

two hours at room temperature using a cobalt rod anode and a steel dummy cathode at a current density of 5 amps/ square foot, to remove impurities. The Alon C powder was then mixed into the electrolyte and stirred for 24 hours, using a magnetic stirrer. The cobalt plating was done with the stirrer operating to hold the alumina powder in suspension.

8. During the plating process, large amounts of hydrogen are discharged at the cathode, tending to form bubbles on the electro-plate which then cause pits to form in the deposit. Two methods are available to remove these bubbles and reduce the extent of pitting. One is to rotate the specimen during plating which agitates solution sufficiently to remove the bubbles. A second is to ultrasonically agitate the plating solution during deposition. Two specimens tested in this effort were electroplated at Watervliet using specimen rotation to achieve smooth plating. At the Science Center all the plating of cobalt was done using ultrasonic agitation by immersing the container holding the plating electrolyte in the water bath of a commercial ultrasonic cleaning apparatus. Plating with ultrasonic agitation produces a fine dispersion of  $Al_2O_3$  particles in the cobalt, while the other technique yields non-uniform localizations of the  $Al_2O_3$ . The consequence of this is discussed in the results section
9. After cobalt plating, the specimen was water rinsed.
10. The specimen was immersed in a fresh chromium plating bath with the current on at entry. The specimen was plated as in step 5 of the chromium plating procedure for 1.5 hours to obtain a chromium plate over the cobalt plate of 0.0015 inch thickness.

11. The plated specimens were heat treated at 750° F for 4 hours in air to remove hydrogen.

### 2.3 Thermal Fatigue Testing

Thermal fatigue cycling was carried out using an MTS electrohydraulic testing machine with 70,000 pounds load capacity. The associated electronics available at the Science Center permit the machine to be operated either in load control using a preset load program or in strain control using a preset strain program. The free expansion tests described below were performed under load control with the load set at zero. The constrained tests described were performed under strain control. The apparatus is equipped with a Lepel induction heating unit for specimen heating. Electronics for temperature measurement and control with the associated circuitry have been developed at the Science Center. The thermal fatigue specimen and most of the load train of the testing machine are enclosed in an air-tight chamber. Before any specimen heating takes place, this chamber is thoroughly flushed with dry nitrogen. Thus, all testing for this work took place with the exterior of the specimen protected by dry nitrogen. Although this apparatus had previously been used for thermal fatigue testing of several materials, it had not been used with steel or tantalum. It was, thus, necessary to develop new test procedures for these materials. Three measurements are required to conduct thermal fatigue tests and to analyze the results: these are the specimen temperature, the instantaneous specimen strain, and the applied load. Test procedures for the new steel and tantalum-10% tungsten geometries were modified and improved as the initial results for these specimens were analyzed. Thus, some of the tests were obtained before a final optimum test procedure had been developed. In the discussion below, this optimum procedure will be emphasized with some note of the initial methods

used. Measurement and control of the three basic test quantities noted above is addressed.

2.3.1 Temperature Measurement and Control. In situ specimen temperature measurements were made using fine wire chromel-alumel thermocouples spot-welded to the center of each test specimen. Two thin couples were fastened on each side of the gage section. The strain measurements (described later) were made on the cross section of the specimen, 90° away from the points at which thermocouples were attached. The outputs from the four thermocouples were combined and averaged to obtain the specimen temperature. This temperature signal is fed to electronics which are used to control the induction power input to the specimen and determine maximum and minimum temperatures for each thermal fatigue cycle. The temperature signal is also used to determine the strain level in the specimen. The gage section of the test specimen was sand-blasted before attaching the thermocouples and this was found to give much better thermocouple adherence. Specimens were heated by placing two flat induction coils around the gage section. These coils were spaced about one-half inch apart and were symmetrically placed with respect to the center of the gage section. A section about one-half inch long in the center of a test specimen could be heated without significantly raising the temperature of the ends. Coils having two turns each were used with steel specimens and gave sufficient electromagnetic coupling to permit rapid heating to any desired temperature. Induction coils do not couple as well to the tantalum-10% tungsten, so for these the coils used had four turns. The induction heater utilized had an operating frequency of 400 kHz; the calculated depth of maximum heating by the induced current was about 0.010 inch. With a wall thickness of 0.025

inch, the induction heater thus gave a reasonably uniform heating rate to the entire specimen cross-section. Because the specimen received its maximum heating in the center of the gage section, the temperatures decreased fairly rapidly on moving toward the specimen ends. In some of the initial test runs, the thermocouples were placed about 1/8 inch away from the specimen center, and it was later found that the measured temperature was about 50° F lower than the peak instantaneous specimen temperature. The couples were positioned in the specimen center on subsequent runs. Cooling was accomplished by blowing compressed dry air through the tubular center of the specimen. The air flow is controlled by valves which open near the start of a cooling cycle and closed at the end of the cooling cycle. An air reservoir is placed in the cooling line to cushion the air flow so that a sudden blast does not hit a hot specimen. With this reservoir in the line air flows continuously throughout the heating and cooling cycle, with a higher flow rate during the cooling portion of the cycle. In the initial tests, cooling was accomplished by injecting water into the air line at a desired time in the cooling cycle. This use of water was found to be undesirable for several reasons. Water would condense in the tubing ahead of the specimen after a few cycles and then drops of liquid water would be carried into the hot specimen. These drops would rapidly cool one spot of the specimen, causing it to suddenly contract and cause large tensile spikes in the load. The load versus time curve was quite irregular with water cooling. On examining the interior of steel specimens which had been water cooled, it was found that thick layers of rust and oxide had formed on the interior surface. Additionally, though water injection did provide very rapid cooling, an early series of tests established that with rapid cooling the specimen

had a tendency to form wrinkles in its cross-section. A somewhat slower cooling did not produce wrinkling. Such wrinkling is thought to be due to temperature gradients in the specimen wall due to the rapid internal cooling. To eliminate the problems caused by water injection in the cooling air, the next cooling additive tried was Freon 11. This provided nearly as rapid cooling as the water injection and did not cause irregular loading due to droplet impingement. However, examination of a Freon tested steel specimen in the scanning electron microscope revealed that the inner surface and all fracture faces were covered with a heavy layer of corrosion products. These were determined by energy dispersive X-ray analysis to consist of metallic chlorides which undoubtedly formed due to the decomposition of the Freon 11 to yield chlorine.

Finally, it was decided to cool with air alone. This gives a somewhat slower cooling rate, but one which was satisfactory to the present tests. It was found that a somewhat faster cooling rate could be achieved by passing the air through a cooling coil immersed in dry ice and acetone. This tended, however, to condense out and freeze any small amount of water present in the air, eventually blocking the lines and reducing the rate of air flow and this was abandoned.

Figure 3 (the curves marked TEMP) shows the heating and cooling rates achieved with induction heating and air cooling. For the particular test illustrated by Fig. 3, the maximum heating rate was about 150° F per second and the maximum cooling rate about 90° F per second. The cooling rate falls very markedly as the temperature falls and becomes very low as the temperature gets less than about 600° F. To obtain more rapid cooling rates in this low temperature regime, it is necessary to cool the air stream or to

inject a liquid into the air.

2.3.2 Strain Measurement and Control. The key element in performing constrained thermal fatigue tests is the accurate measurement and control of the instantaneous strain during the thermal cycle. In the present tests, changes in the specimen diameter at the center of the specimen were used for the measurement of the specimen strain during test. The strain measuring device is described in detail in Appendix A. It consists of two quartz arms attached at their midpoint to a pivot member. One end of each arm has a knife edge which rests on the gage diameter of the specimen. To keep the knife edges from cutting into the specimen at peak temperature, small quarter circle sections of quartz tube are attached to the strain measuring device. The quartz tube sections are, in turn, attached to the specimen using vacuum grease. This has always successfully held the tubes in place during the heating and cooling cycle. At the opposite end of the quartz arms is attached a clip-on strain gage made with special low elastic modulus arms to reduce the forces exerted by the gage on the specimen. The entire device is calibrated with a micrometer and is sensitive to a diameter change of considerably less than 0.001 inch. In Fig. 3a, the measured diameter change on heating from 480° F to 1250° F is 0.00136 inch, illustrating the high measurement sensitivity. This device was developed by P. J. Stocker of the Science Center in work funded by the Science Center. The first application of this device was on the present contract.

The means of selecting and controlling the operating strain is illustrated by Fig. 3. The specimen was first cycled over the desired temperature range, in this case 480° F to 1250° F, under zero load and the diameter change measured, being in this case 0.00136 inch, as noted above. The

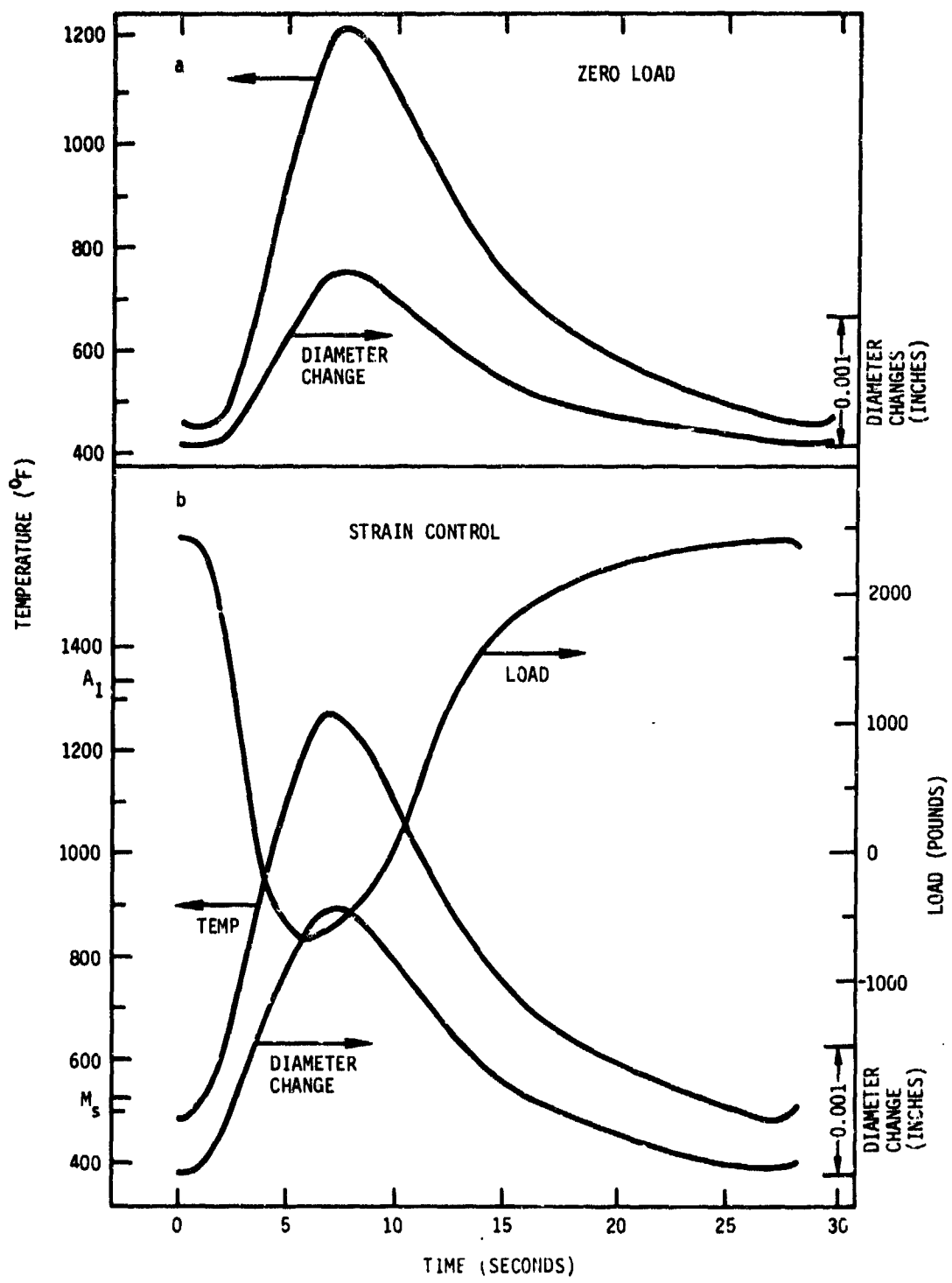


Fig. 3 Thermal fatigue cycles for chromium plated specimen BB. a) zero load (free expansion) cycle. b) Cycle showing load imposed to constrain diameter.

original specimen diameter was 0.250 inch, with a chromium plate of 0.0063 inch, giving a total diameter of 0.2626 inch. Thus, the strain due to thermal expansion is 0.52%.

The electronics of the MTS electrohydraulic testing machine used allow the strain to be controlled by requiring that the strain signal be a certain fraction of the temperature signal over a desired temperature and strain range. In the present case, it was decided that the specimen diameter should be required to expand by nominally 0.2% over the temperature range of 480-1250° F in addition to the thermal strain of 0.52%. Figure 3b shows that on setting the various span signals necessary to operate in strain control, the diameter change over the 480-1250° F range achieved was 0.00198 inch, corresponding to a strain of 0.75%. Thus, the specimen received 0.23% diameter strain in addition to the thermal strain. Note in Fig. 3b that the upper temperature of the thermal cycle had increased to 1275° F, so that the total diameter change over the entire thermal cycle was 0.00207 inch, part of which is due to thermal expansion and part due to the imposed strain. In this case it was desired that the specimen be in compression at the highest temperature. Consequently, specimen diameter was forced to become larger than it would due to thermal expansion alone. If it had been desired that the stresses be tensile at high temperature, then the diameter could have been forced to become smaller than it would have been due to thermal expansion alone.

In cases where the material undergoes a phase transformation during the thermal cycle, the specimen diameter does not change smoothly with temperature as seen in Fig. 3a, but suddenly increases or decreases in diameter over a short temperature range near the phase transformation temperature.

In this case, the maximum and minimum specimen diameters can not be used to set the constrained amount of strain. Instead, the slope of a plot of diameter versus time is scaled to the slope of the temperature-time plot. In the absence of a phase transformation, this calculation gives the same result as for the use of the maximum and minimum diameters.

Some of the initial tests were carried out using nominally imposed diametral strains of 0.8% in addition to the thermal strain. This peak strain was found to give, however, what appeared to be quite short failure times, with failure occurring in 25 cycles or less, in some cases. In the later runs the imposed diametral strain was fixed at a nominal value of 0.2% in addition to the thermal strain; this gave considerably longer thermal fatigue lives. This was felt to be desirable because it provided more chance for specimen failure to be caused by the plating failure rather than to result from substrate material failure alone.

2.3.3 Stress Measurement. One of the results of the thermal fatigue measurement is the stress developed as the specimen is thermally cycled under constraint. The loads (which correspond to the stress born by the specimen) were measured by the load cell of the MTS testing machine. During the unconstrained (free expansion) cycles of each specimen, used to determine the strain due to thermal expansion, the load was controlled at zero; this was the case for Fig. 3a. During the actual test, when the specimen was constrained, quite high loads were developed. For each specimen tested, the measured loads achieved an equilibrium for each temperature in only a few cycles and subsequently changed only slowly as cycling proceeded. During the lower temperature portion of the cycle, a high tensile load developed. As the temperature increased, the loads decreased and then became

compressive during the high temperature portion of the cycle. Figure 4 shows stress versus temperature for the thermal cycle of Fig. 3b.

**2.3.4 Failure Criteria.** In performing the thermal fatigue tests, many of the specimens were run to failure. For some of the tests the point of failure was quite marked. The specimen broke sharply, usually at a low temperature, where the loads were tensile. For some of the longer lived specimens, however, there is no specific point at which the specimen could have been said to have failed. In these cases, the compressive and tensile loads would gradually decrease toward zero. Failure was deemed to have occurred when the load had decreased to a small fraction of the load observed in the early cycles, and the test was stopped at this point. The load had usually dropped to less than half the initial load in these cases.

**2.3.5 Selection of Temperature Cycling Ranges.** The thermal fatigue cycling was conducted over a range of temperature defined by some maximum temperature  $T_{\max}$  and some minimum temperature  $T_{\min}$ . For the steel specimens, there are two temperature points characteristic of phase transformations in the steel, which have determined the thermal cycling ranges of interest. These two temperatures are the martensite start temperature,  $M_s$ , and the lowest temperature for austenite formation,  $A_1$ . A heat treated alloy steel at room temperature consists of tempered martensite. When this material is heated above  $A_1$  ( $1340^{\circ}\text{F}$ ), it will begin to transform to the face centered cubic austenite phase. This transformation is complete for steels with 0.4% carbon when the temperature exceeds approximately  $1450^{\circ}\text{F}$ . On cooling this material it will remain as austenite until the temperature falls below  $M_s$ , which is about  $525^{\circ}\text{F}$  for gun steel and 4340 steel. (These steels have

such high hardenability that they will not transform to pearlite or bainite even on cooling much more slowly than the rates used in these tests.) At and below  $M_s$  the steel transforms to the body centered tetragonal martensite structure which persists down to low temperature. On transforming from martensite to austenite on heating, the lattice unit cell contracts and the volume per unit weight decreases. Conversely, on transformation from austenite to martensite on cooling, the value increases and the specimen expands.

Three temperature ranges were selected for the thermal cycling. The first of these had  $T_{max}$  less than  $A_1$  and  $T_{min}$  less than  $M_s$ . In this range, the steel structure remains as tempered martensite throughout the thermal fatigue cycle, with some further tempering of the martensite occurring during the high temperature portion of each cycle. The second cycling range used had  $T_{max}$  greater than  $A_1$  and  $T_{min}$  greater than  $M_s$ . On cycling over this range, the steel transforms to austenite on the first cycle and remains austenite during subsequent cycles since the temperature never drops below  $M_s$ . On ending the test, the temperature would drop below  $M_s$  on cooling to room temperature so the final structure is martensite.

The third cycling range used had  $T_{max}$  greater than  $A_1$  and  $T_{min}$  less than  $M_s$ . In this range, the steel transforms to austenite on each heating cycle and then transforms back to martensite on each cooling cycle. The final structure ends as martensite.

In Fig. 3b the temperature, diameter change, and load curves shown correspond to cycling in the first temperature range, where the temperature is always below  $A_1$ . In Fig. 5 is shown a corresponding plot for cycling through the third temperature range, above  $A_1$  and below  $M_s$  on each cycle.

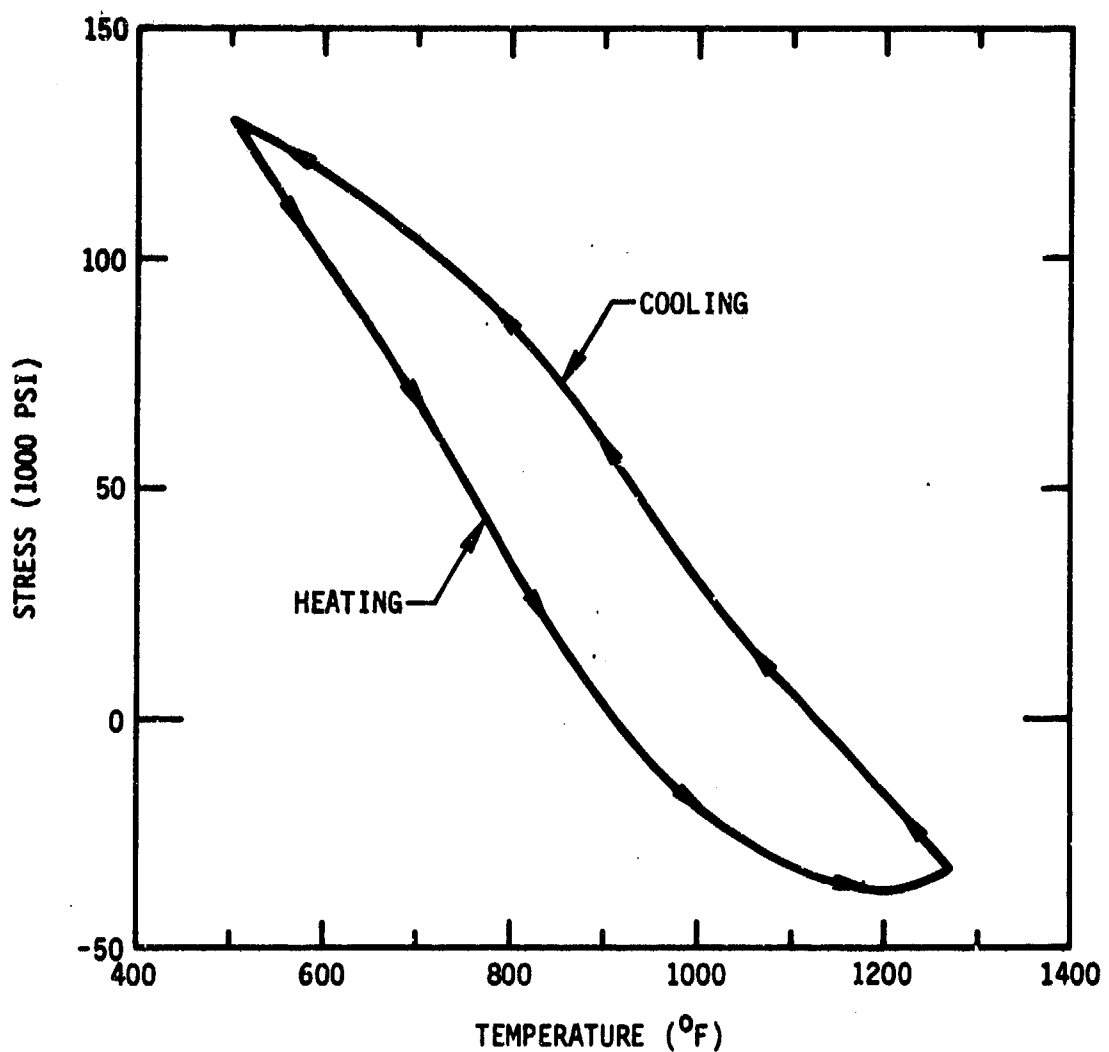


Fig. 4 Stress versus temperature for specimen BB for the constrained thermal fatigue cycle of Fig. 3b.

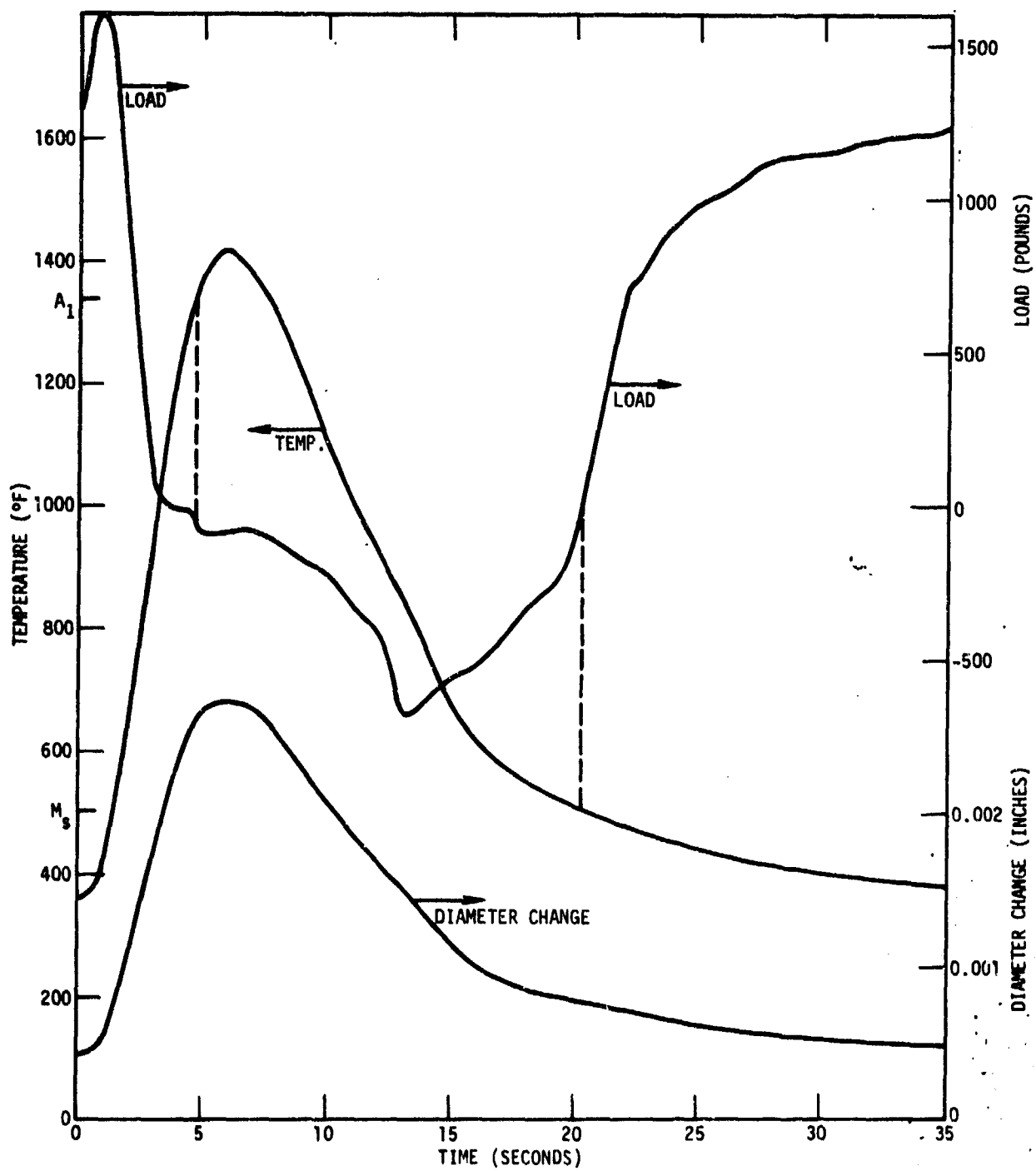


Fig. 5 Thermal fatigue cycle for bare specimen BK cycled above  $A_1$  and below  $M_s$

In this case, on reaching  $A_1$ , the volume of the material in the specimen decreases and the testing machine applies more compressive load to maintain the diameter on the preset strain curve. As the specimen cools, the loads remain compressive until  $M_s$  is reached, at which temperature the volume increases and the machine applies a tensile load to maintain the smaller diameter required by the strain curve. For cycling through the second range temperature, where the temperature is above  $M_s$  after the first cycle, the time record of load is similar to Fig. 3b, except that on the first cycle an effect occurs at  $A_1$  when the material first becomes austentic.

#### 2.4 Materials Characterization

The specimen materials were characterized before and after testing, using several techniques including optical microscopy and scanning and transmission electron microscopy. Microstructures were determined by optical microscopy. The steel and tantalum-10% tungsten materials were mounted in plastic, mechanically polished using alumina powder, and then etched for microscopic examination. The steels were etched in Nital (2%  $HNO_3$  in methanol) for periods ranging from a few seconds to about three minutes. The tantalum-10% tungsten was etched using a solution of 60ml lactic acid, 20ml  $HNO_3$  and 20ml HF. Plated cobalt layers were electropolished in a solution of 50%  $H_3PO_4$ -50%  $H_2O$  for about three minutes at a voltage of 1.5 volts. Etching was accomplished by lowering the polishing voltage to less than one volt.

To prepare specimens for transmission electron microscopy, small sections were cut from various test specimens. They were ground to a thickness of 0.001 inch and then electropolished at room temperature, using

a solution of 8 parts acetic acid and 1 part perchloric acid. This polishing technique was applied to chromium plated and cobalt chromium plated specimens as well as to bare steel specimens. Specimen preparation for the thermal fatigue specimens was complicated both by the fact that the materials were usually heavily microcracked and because optimum polishing conditions are a function of the fatigue history.

For examination by scanning electron microscopy (SEM) thermal fatigue specimens were sectioned after testing using an abrasive cut-off wheel. For specimens which had fractured during fatigue, one side of the fracture surface was cut off for direct examination. In addition, for all specimens examined, sections were cut parallel to the longitudinal axis of the specimen through the wall thickness. These were electropolished, using the perchloric acid-acetic solution above, to examine the interface regions of the chromium-steel, chromium-cobalt and cobalt-steel layers. Energy dispersive X-ray methods were used to determine chemical compositions and contaminants of the various layers and of various particles and inclusions observed. Before the SEM examination, the cut specimens were washed in acetone to remove any traces of grease and other soluble contaminants.

Some of the plated specimens were examined for surface contaminants using Auger electron spectroscopy (AES). The specimens were cleaned in acetone and mounted in a high vacuum AES chamber. The composition of the surface layer was determined by AES, and then successive layers were sputtered off using argon ions bombardment. The composition of each layer after sputtering was measured by AES. By this sputtering method, material is removed at the rate of about 10 Angstroms per minute. For the specimens

examined, sputtering was continued for depths of up to 320 Angstroms from the surface.

### 2.5 High Temperature Mechanical Properties

High temperature mechanical properties of the gun steel were determined in the range of 1200 to 1500° F. Small cylindrical specimens cut 0.125 inches in diameter by 0.5 inches long, were inserted in a compression test fixture in a high temperature vacuum furnace mounted on an Instron testing machine. The vacuum was established and the furnace was stabilized at the desired temperature. The specimens were loaded in compression at a constant cross-head speed. The observed behavior was that the load initially increased and then leveled off at a constant value characteristic of the crosshead speed. After the load had leveled off, the crosshead speed was then increased or decreased and the process continued until the desired range of strain rate had been covered. The steady state stress was calculated from the load and the original cross sectional area. The strain rate was calculated from the crosshead speed and the original sample length. The total deformations obtained were not large, so the use of the original specimen dimensions, rather than the instantaneous dimensions, introduced only a negligible error into the calculated results.

### 3. RESULTS

A large number of specimens were fabricated and then tested over the contract period by several different methods. The results of these tests and the subsequent specimen characterizations are presented in the following sections. In section 3.1 a table showing the various specimens tested is presented and other results are later described in terms of this table. In section 3.2 some results of the prethermal fatigue characterization of specimen materials are presented. The results of the high temperature mechanical properties test on gun steel are in section 3.3. Finally the thermal fatigue results are given. These are broken into a presentation on, first, bare steel, then chromium plated steel, then cobalt-chromium plated steel, and finally tantalum-10% tungsten. For purposes of conciseness chemical symbols will be used to identify the tested materials in the following section: cobalt (Co); chromium (Cr); tantalum (Ta); tungsten (W). A phrase "Co layer" should be understood to imply cobalt dispersion hardened with  $\text{Al}_2\text{O}_3$  unless otherwise specified.

#### 3.1 Test Specimens

Table III lists the specimens fabricated for this investigation with a brief summary of their history. The order in which the specimens are listed is of no particular significance. Each specimen was assigned identification letters when it was first cut from the raw stock. Table III indicates the value of  $T_{\min}$  and  $T_{\max}$  over the principal testing range for each specimen. When  $T_{\max}$  is less than  $1340^{\circ}\text{F}$  ( $A_1$ ), the specimen underwent no phase transformations during test. When  $T_{\max}$  is above  $1340^{\circ}\text{F}$  and  $T_{\min}$  is above  $525^{\circ}\text{F}$

Table III.  
Specimen Summary and Nominal Test Conditions

Specimen Letters	Material (1)	Type (2)	Plate (3)	Temp. (°F)	Constraint (%) (4)	Cooling (5)
AA	4340	TF	Cr	300-1360	0	
AB	GS	TF	Bare	various	0	W
AC	GS	TF	Cr	not tested		W
AD	GS	TF	Cr	not tested		
AE1	GS	D	Cr	hardness test for Cr		
AE2	GS	D	Cr	hardness test for Cr		
AF1	GS	D	Crare	not tested		
AF2	GS	D	Bare	not tested		
AG	GS	TF	Bare	accidentally destroyed in test		
AI	GS	TF	Bare	various	0	W
AJ	GS	TF	Bare	450-1400	0	
AK	GS	TF	Bare	300-1340	0	W
AL1-AL12	GS	CS	Bare	High temperature flow stress		
AM	GS	TF	Co+Cr	300-1250	0.8	F
AN	GS	TF	Co+Cr	300-1250	0.8	F
AO	GS	TF	Cr	unsatisfactory plate		
AP	GS	TF	Cr	325-1250	0.8	F
AQ	GS	TF	Cr	325-1250	0.8	F
AR	GS	TF	Bare	400-1250	0	W
AS	GS	TF	Bare	640-1440	large	W
AT	GS	TF	Bare	640-1440	0.8	W
AU	GS	TF	Cr	400-1450	0.2	A
AV	GS	TF	Cr	400-1450	0.2	
AW	GS	TF	Bare	300-1275	0	F
AX	GS	TF	Bare	300-1275	0.8	F
AY	GS	TF	Bare	300-1360	0.8	F
AZ	GS	TF	Bare	300-1200	0.8	F
BA	GS	TF	Bare	300-1400	0	
BB	GS	TF	Cr	400-1300	0.2	F
BC	GS	D	Bare	not tested		A
BD	GS	D	Cr	Metallography and SEM		
BE	GS	D	Co + Cr	Metallography, AES and SEM		
BF	GS	D	Co + Cr	Metallography, AES and SEM		
BG	GS	TF	Bare	635-1450	0.2 & 0.8	A
BH	GS	TF	Cr	635-1450	0.2	A
BI	GS	TF	Bare	425-1440	0.2	A
BJ	GS	TF	Bare	600-1375	0.8	A
BK	GS	TF	Bare	325-1410	0.2	A
BL	GS	TF	Cr	650-1460	0.2	A
BM	4340	TF	Cr	unsatisfactory plate		

Table III. - Specimen Summary and Nominal Test Conditions (cont.)

Specimen Letters	Material (1)	Type (2)	Plate (3)	Temp. (°F)	Constraint (%) (4)	Cooling (5)
BN	4340	TF	Co+Cr	650-1460	0.2	A
BO	4340	TF	Co+Cr	400-1300	0.2	A
BQ	4340	TF	Bare	400-1450	0.2	A
BR	4340	TF	Co+Cr	600-1400	0.2	A
BS	4340	TF	Co+Cr	450-1450	0.2	A
BT	4340	TF	Co+Cr	600-1400	0.2	A
BU	4340	TF	not tested			
BV	4340	TF	Bare	400-1300	0.2	A
BW	4340	TF	Bare	600-1450	0.2	A
BX	4340	TF	Bare	450-1450	0.01	A
BY-CE	4340	TF	not tested			
CF	GS	TF	Co+Cr	430-1420	0.2	A
CG	GS	TF	Co+Cr	unsatisfactory plate		
CH	Ta-W	TF	Bare	500-1500	0	A
CI	Ta-W	TF	Bare	600-1500	0.2	A
CJ	Ta-W	TF	Bare	600-1500	0.8	A
CK-CO	Ta-W	TF	not tested			
CP	Ta-W	D	metallographic specimens			
CQ	4340	TF	Bare	325-1440	0.8	
CR	4340	TF	Bare	350-1400	calibration specimen	
CS	4340	TF	Bare	375-1450	0.8	
CT	GS	TF	Bare	470-1260	0.2	A

## Notes:

1. 4340 = 4340 steel; GS = gun steel; Ta-W = tantalum-10% tungsten alloy.
2. TF = thermal fatigue; D = disk specimen; CS = compression test specimens.
3. Bare = no electroplate; Cr = chromium; Co = cobalt with dispersed  $\text{Al}_2\text{O}_3$ , except for specimen BF which had no  $\text{Al}_2\text{O}_3$ .
4. Constraint is nominal applied diametral strain in addition to thermal expansion.
5. A = air cooling; W = air with injected water; F = air with injected Freon 11.

( $M_s$ ), the cycling was done in the austenitic phase. When  $T_{max}$  is above 1240°F and  $T_{min}$  is below 525°F, the specimen underwent phase transformations on each thermal fatigue cycle.

As noted in the experimental section, air cooling with no injected fluid was found to be least damaging to the specimens. Many of the earlier tests were performed with water or Freon 11 in the air stream. Most of the analysis of results which follows is confined to specimens which were tested with air cooling only.

### 3.2 Initial Specimen Characterization

In this section are discussed some results of specimen materials characterization before the materials had been subjected to thermal fatigue cycling. This includes analysis of both the substrate and coating materials.

3.2.1 Steel and Ta-10%W. Figure 6 shows the microstructure of the gun steel and of 4340 steel as found in the as machined specimens. As noted earlier, the gun steel was received in a heat treated condition. Its microstructure, as seen in Fig. 6a, is typical of tempered martensite. Fig. 6b shows the microstructure of 4340 steel after water quenching from 1500°F and tempering at 900°F. Again, this is typical tempered martensite. Fig. 7 is a transmission electron micrograph of the gun steel as received. Large numbers of small carbide particles are visible, presumably  $Fe_3C$  which has formed during the tempering of the steel.

Figure 8a shows the microstructure of the Ta-10% W material as received. The microstructure is seen in cross section and is a wavy cold worked structure due to the final reduction to size during processing. The microstructure

parallel to the rod direction is shown in Fig. 8b, with the arrows indicating the rod direction. The grain structure is appreciably elongated in this direction.

### 3.2.2 Plating Materials.

3.2.2.1 SEM and TEM Observations. Figures 9 and 10 are scanning electron micrographs of the as-plated chromium and cobalt chromium plate on disk specimens of gun steel. Fig. 9a and 9b are for Cr over Co as-plated before the post-plating bake. The specimen BF has no  $\text{Al}_2\text{O}_3$  in the cobalt. The Co/Cr interface is fairly irregular and some cracks are present in the Cr. After baking, Fig. 9c, the number of cracks in the Cr has not increased, though some of the cracks appear to have propagated a short distance into the Co, Fig. 9d.

Figures 10a and b show Cr plate over Co plate dispersion hardened with  $\text{Al}_2\text{O}_3$  and in the as-plated (unbaked) condition. The Co plate here has about three times as many cracks per unit interfacial length as the Co plate of Fig. 9. Figure 10b shows one of these cracks in detail. The Co/Cr interface is much smoother in appearance than for the Co plate specimen containing no  $\text{Al}_2\text{O}_3$ . It is not known whether this is due to the presence of the  $\text{Al}_2\text{O}_3$  or whether some other plating variable change caused the interface roughness seen. It is possible that the  $\text{Al}_2\text{O}_3$  content may affect the roughness of the Co/Cr interface and hence the extent of cracking in the Cr plate. Further depositions would be required to test this. In Fig. 10c and 10d are shown Cr plate on gun steel after baking.

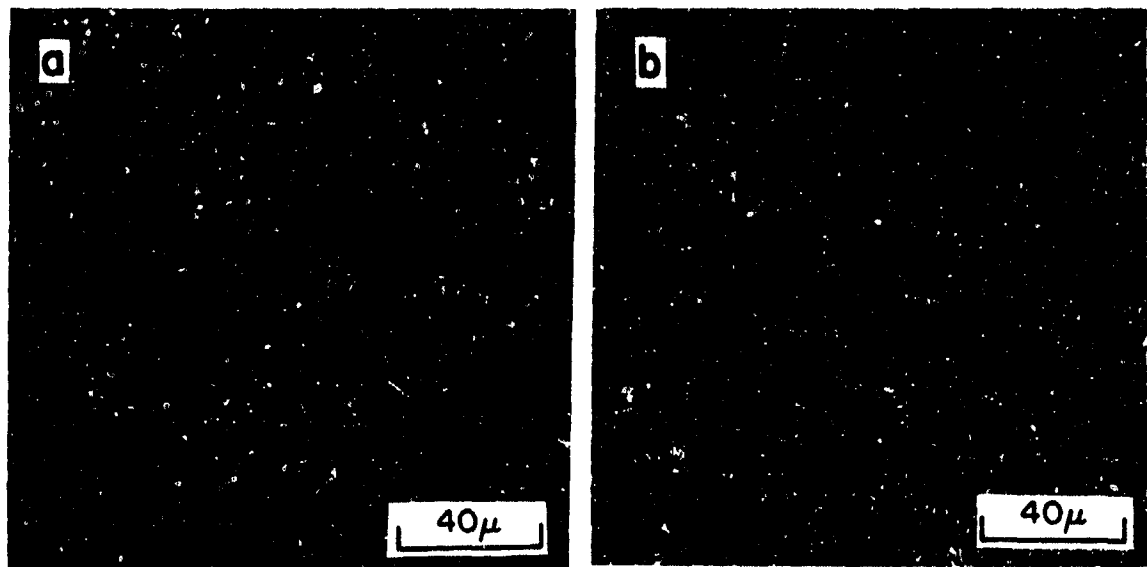


Fig. 6 Optical micrographs of etched sections of a) as received gun steel, b) heated treated 4340 steel.

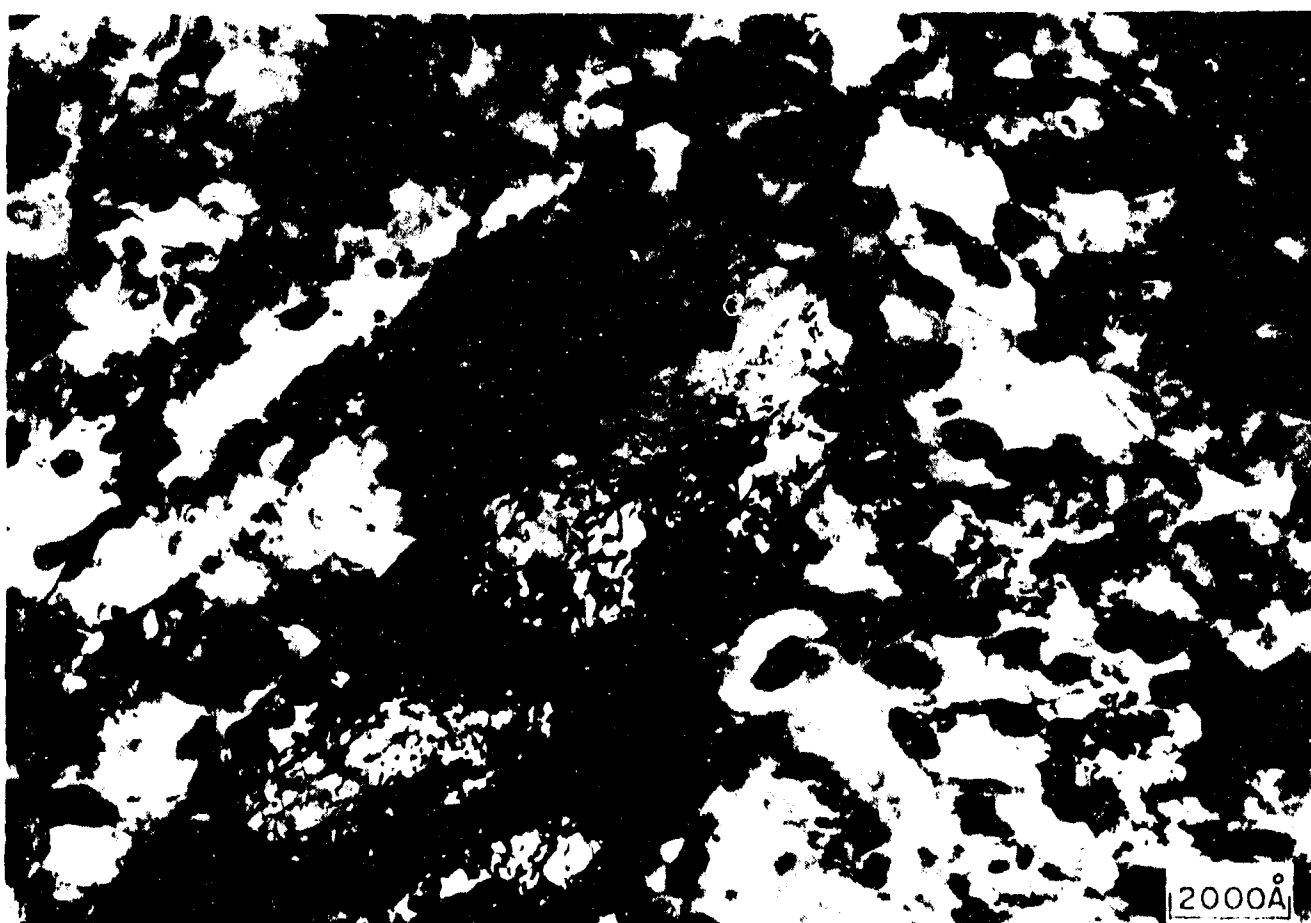


Fig. 7 Transmission electron micrograph of as received gun steel.

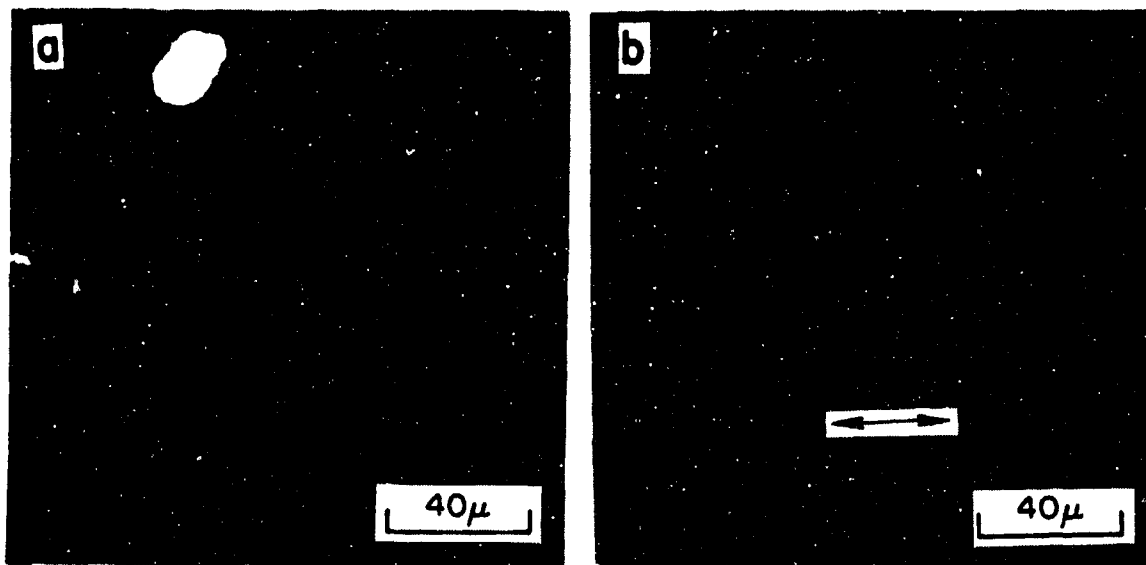


Fig. 8 Optical micrographs showing structure of as received Ta-10% W bar:  
a) section through bar; b) section along bar, arrow in direction of  
bar axis.

28-c

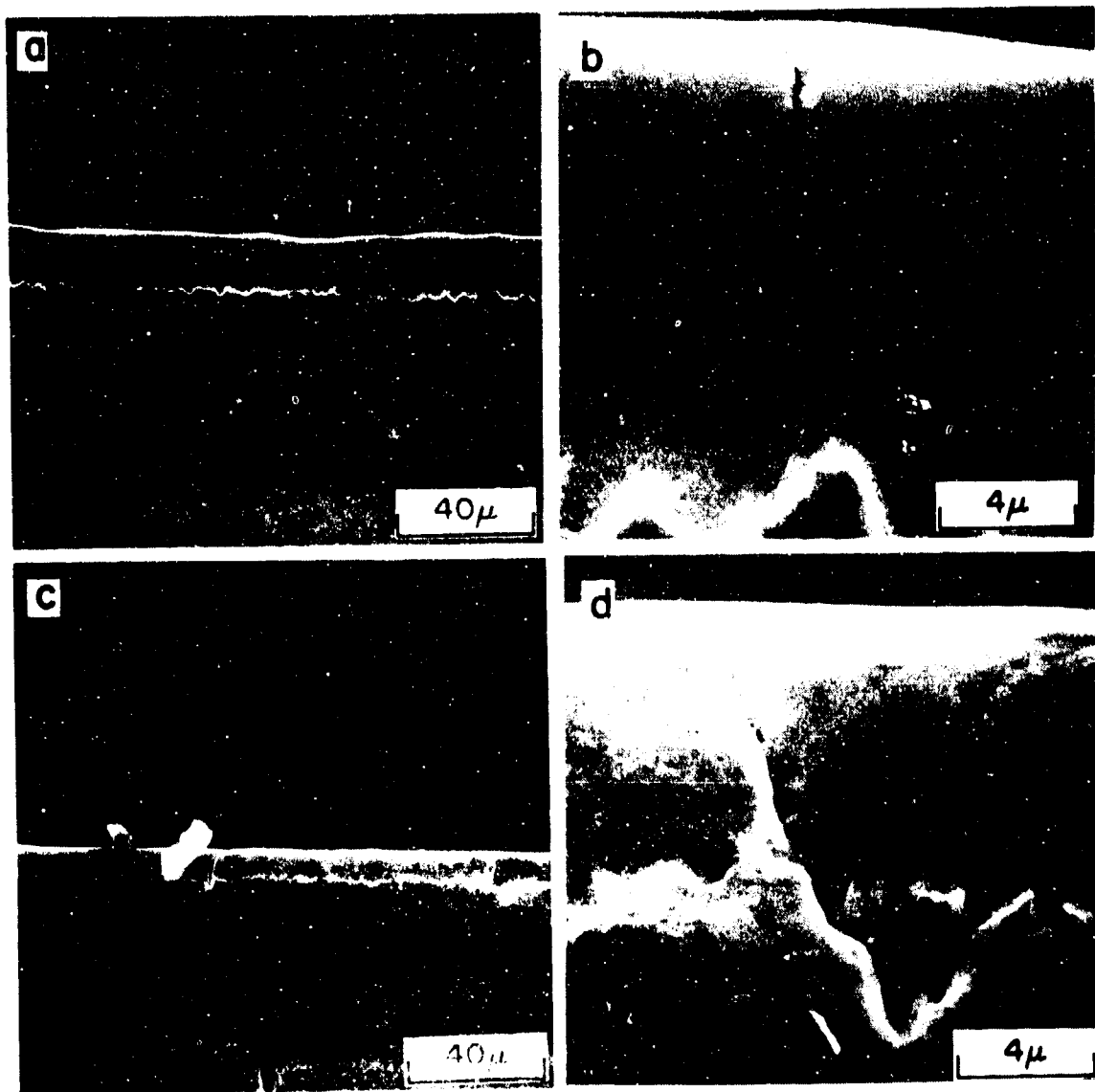


Fig. 9 Scanning electron micrographs of electropolished sections of specimen BF, a Cr/Co plated specimen with no  $\text{Al}_2\text{O}_3$  in the cobalt: a), b) as plated; c), d) after bakeout. Cr on top.

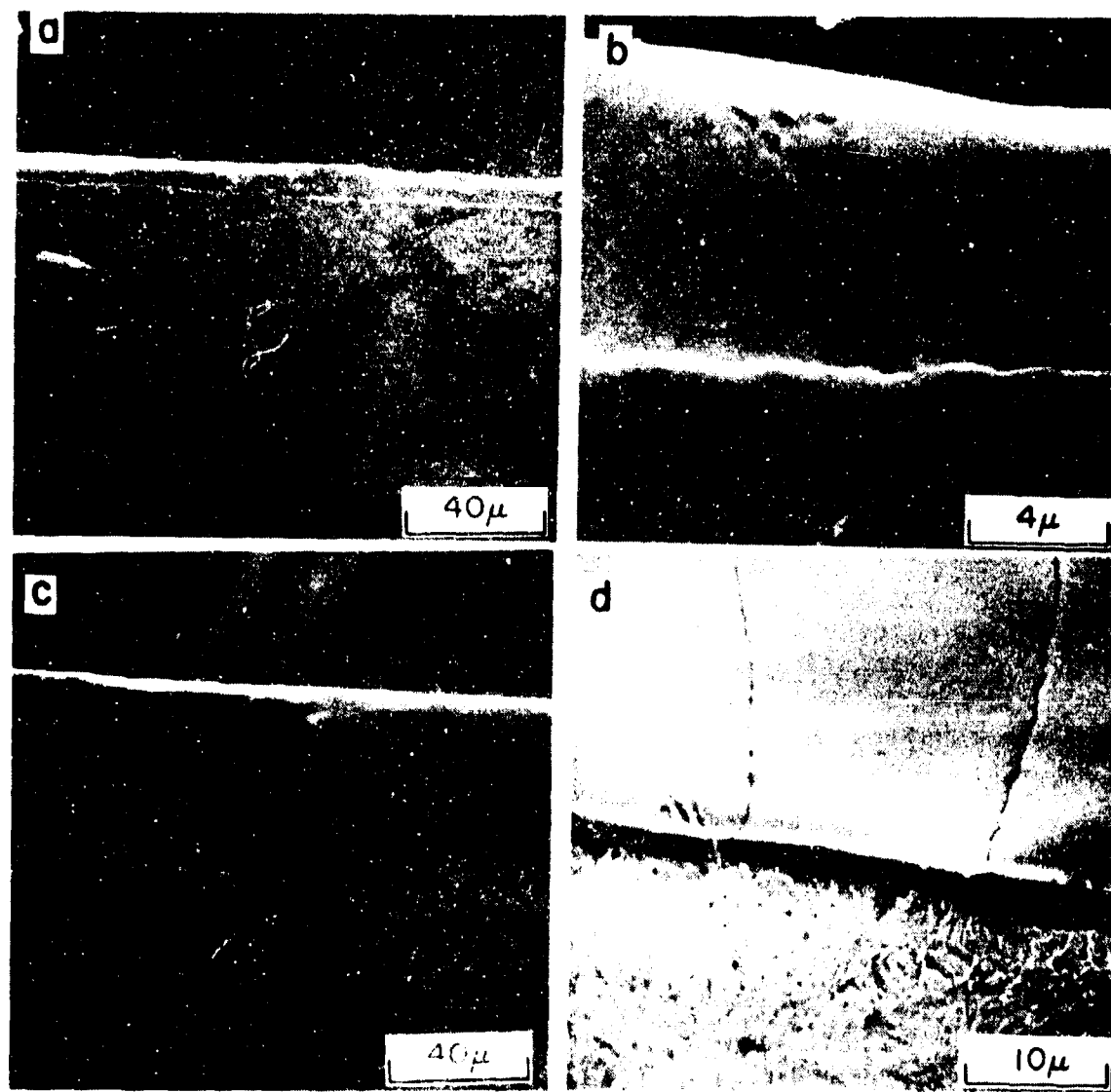


Fig. 10 Scanning electron micrographs of electropolished sections of a), b) Cr/Co plated specimen, cobalt containing  $\text{Al}_2\text{O}_3$ , specimen not baked, c), d) Cr plated steel specimen baked. Cr on top.

The frequency of cracks in this plate is lower than that for the Co in Fig. 10a and is about the same as for the plate of Fig. 9a. Figure 10d shows that the baking process has not caused cracks to propagate from the Cr plate into the steel. No cracks are observed in the plated or baked condition at the Co/steel interfaces or in the Co except for the small crack extension into the Co from the Cr plate noted in Fig. 9d.

Figures 11 and 12 are transmission electron micrographs of the plated and baked Co layer containing  $\text{Al}_2\text{O}_3$ . The  $\text{Al}_2\text{O}_3$  is found to be unexpectedly low. The dark field micrograph was taken with maximum illumination of  $\text{Al}_2\text{O}_3$  in the region indicated by the arrow (Fig. 12). The content of  $\text{Al}_2\text{O}_3$  in actual thermal fatigue specimens has been found to be higher. Note the fine grain structure of the as-plated cobalt; even at this high magnification the grains appear quite small and irregular. As seen in Fig. 9 and 10a and b the Co plate thickness is about 6 mils and the Cr thickness about 1.5 mils. These values of plate thickness are typical of all plated specimens used in the present program.

3.2.2.1. Auger Measurements. In several cases the Cr plate turned yellowish on its outer surface after baking. Some specimens, however, retained the clear white color typical of Cr plate. To identify the cause of the color change several specimens were examined by Auger electron spectroscopy (AES) both at the surface and after sputtering off successive layers. Four specimens were examined. These were pieces of specimens BE and BF, Table III. One piece of each specimen was examined as-plated and one piece of each after baking at  $750^{\circ}\text{F}$  for four hours. The elements found at the surfaces of the specimens included (in addition to chromium), sulfur, chlorine, carbon, calcium, nitrogen, oxygen, iron, sodium, magnesium, silicon and phosphorus. The sodium, magnesium, silicon and

chlorine were almost all removed by sputtering away 20Å from the surface and were probably present due to handling of the specimen after plating. Most of the calcium was also removed by sputtering of about 20Å, though traces were present to much deeper levels. Small amounts of sulfur, carbon, oxygen and nitrogen were present at all levels of sputtering in the chromium layer. The only element present that could have caused the yellow color on the surface was iron. The iron content found as a function of depth is given in Table IV, where the numbers are the height of the iron AES peak as percent of the chromium AES peak. No iron was detected on specimen BE as-plated. Specimen BF as-plated had a small amount of iron which was all within 40Å of the surface. After baking both BE and BF had iron present to depths of 80Å or more. It appears that a small amount of iron may have been present at the surface after plating and that considerably more iron was picked up during the baking process. Since the baking was done in air, the iron was oxidized and incorporated into the thin chromium oxide layer which formed on the chromium plate. There is no evidence that this iron or any specimen contamination had any adverse effect on the specimen behavior during subsequent testing.

### 3.3 High Temperature Mechanical Properties

The flow stress of gun steel was measured over the range of strain rates from  $7.2 \times 10^{-7} \text{ min}^{-1}$  to  $1.7 \times 10^{-3} \text{ min}^{-1}$  at temperatures of 1200, 1300, 1400 and 1500°F. The procedure is described in section 2.5 of the experimental portion of this report. The results of the steady state flow stress measurements are presented in Table V and are plotted in Figure 13. It is apparent that at low strain rates the flow stress is independent



Fig. 11 Transmission electron micrograph of Co layer for Co/Cr plated specimen BE.

30-12

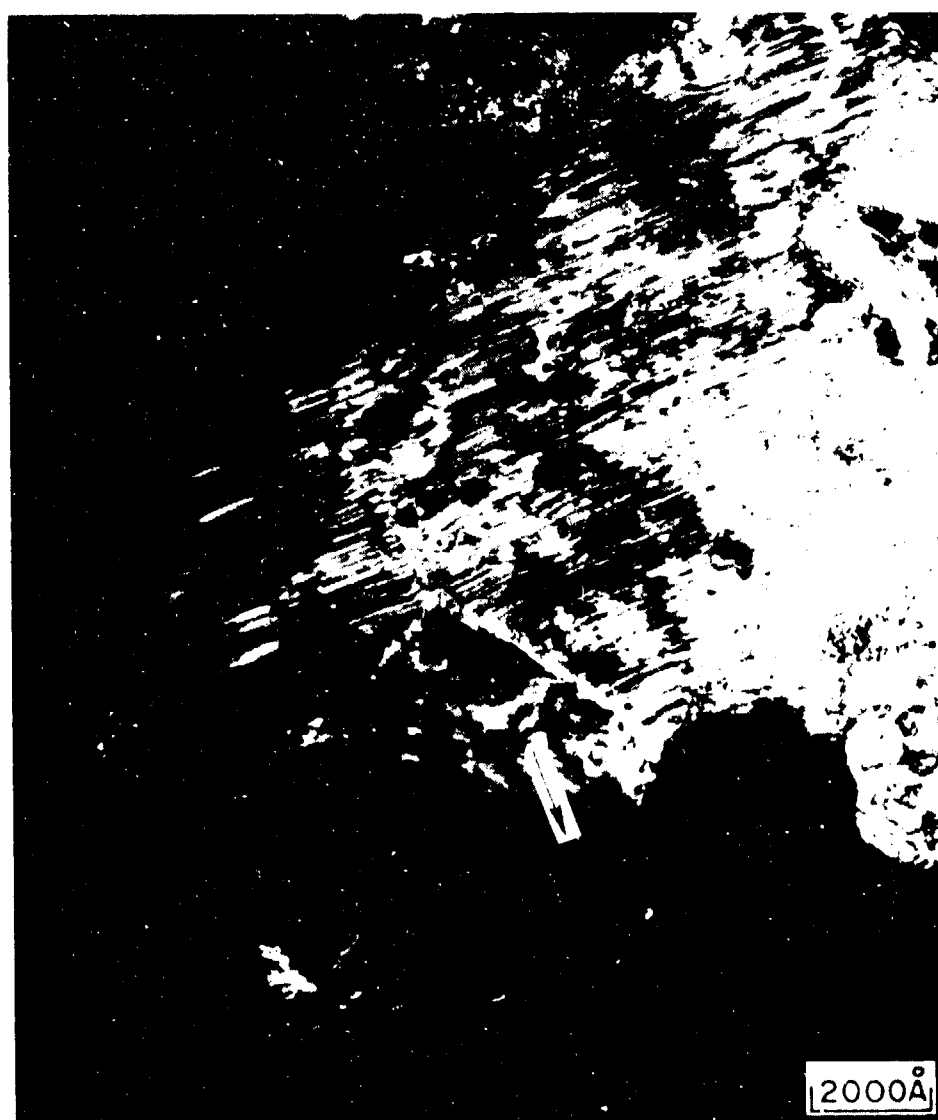


Fig. 12 Dark field transmission electron micrograph of Co layer or Co/Cr plated specimen B1. Arrow at illuminated Al<sub>2</sub>O<sub>3</sub> particles.

31-6

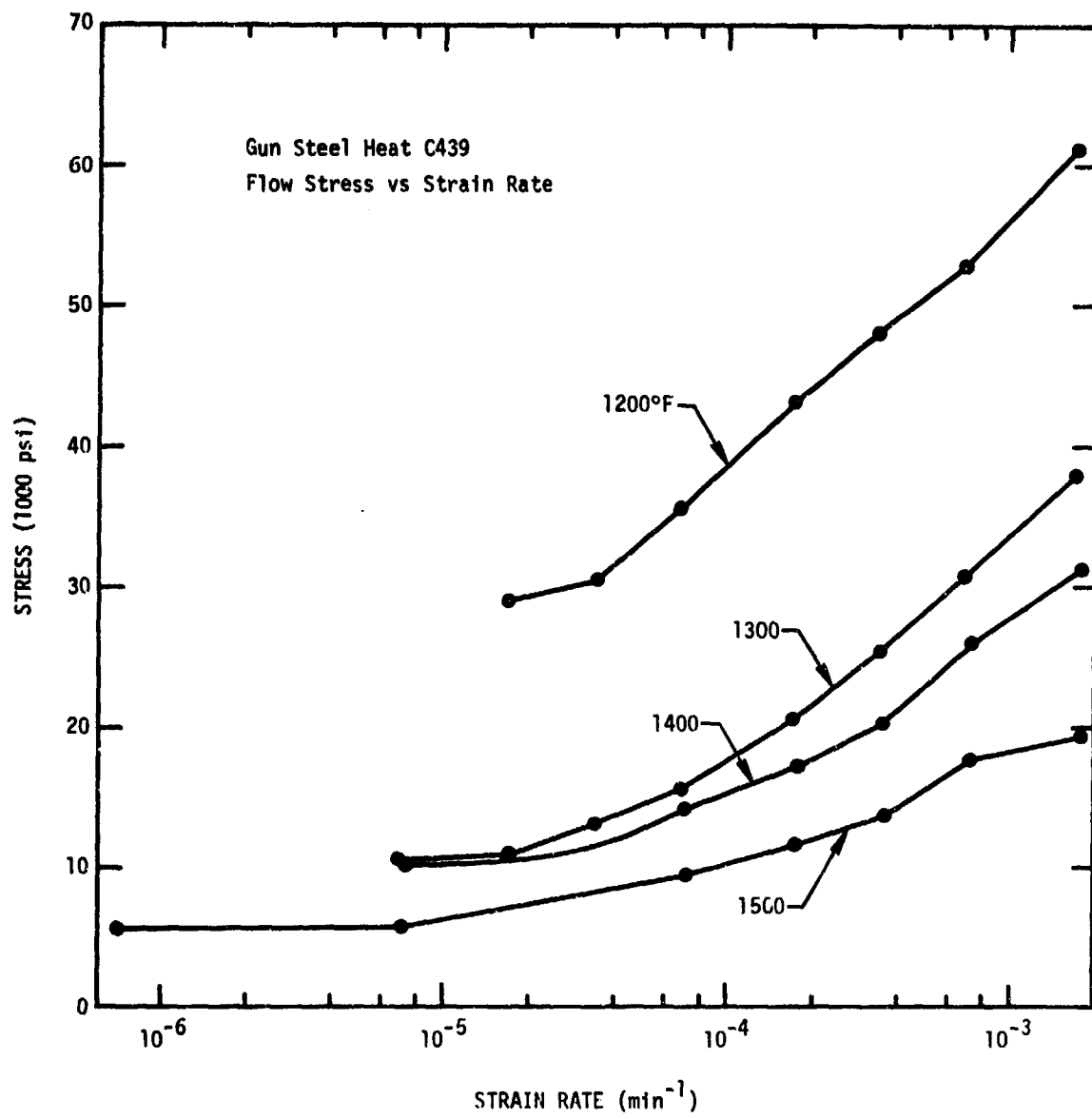


Fig. 13 Flow stress versus strain rate at various temperatures for gun steel.

30-21

Table IV.

Iron Contamination of Chromium Plate  
(Height of Iron Auger Peak as percent of Chromium Auger Peak)

Depth (Angstroms)	Specimen			
	BE as plated	BF as plated	BE baked	BF baked
0	0	2	6.5	1.3
10	0	1	2.3	0.9
20	0	0.4	2	0.8
40	0	0.1	1	0.6
80			0.5	0.6
160			0	0.4
320			0	0

Table V.  
Flow Stress of Gun Steel

Strain rate <sub>1</sub> (min <sup>-1</sup> )	Flow Stress (1000 psi)			
	1200°F	1300°F	1400°F	1500°F
$7.2 \times 10^{-7}$				5.5
$7.2 \times 10^{-6}$		10.5	10.2	5.8
$1.7 \times 10^{-5}$	29.0	11.0		
$3.4 \times 10^{-5}$	30.5	13.0		
$6.9 \times 10^{-5}$	35.6	15.7	14.3	9.5
$1.7 \times 10^{-4}$	43.2	20.6	17.1	11.6
$3.4 \times 10^{-4}$	48.1	25.3	20.4	13.8
$6.9 \times 10^{-4}$	53.0	30.8	26.1	17.7
$1.7 \times 10^{-3}$	61.1	37.9	31.4	19.1

of strain rate, whereas it becomes quite strain rate dependent at higher strain rates. The room temperature strength of this material, as reported by the producer from results of standard tensile tests is as follows: yield strength, 164,000 psi, ultimate strength, 180,000 psi.

As a point of reference for comparison to the thermal fatigue tests described in the next section, the stresses developed during thermal fatigue of steel fall in the range of 6000 to 12,000 psi at 1400°F. From Figure 4 it can be seen that the stresses at 1200°F are around 37,000 psi. These values are quite comparable to the measured flow stress for the lower strain rates at the applicable temperatures shown in Fig. 13.

### 3.4 Thermal Fatigue Tests.

The methods used for performing the thermal fatigue tests are described in detail in the experimental section. As can be seen from Table III, a large number of thermal fatigue specimens were fabricated and tested under a range of conditions. As an aid in identifying the various conditions of test used for each specimen, Table VI summarizes the test conditions utilized. At the top of the table is the temperature range used for thermal fatigue testing. Specimens in the column labeled Below  $A_1$  were tested with  $T_{max}$  less than  $A_1$  and  $T_{min}$  less than  $M_s$ . Above  $M_s$  means that  $T_{max}$  was greater than  $A_1$  and  $T_{min}$  greater than  $M_s$ . Through  $A_1$  and  $M_s$  means that  $T_{max}$  was greater than  $A_1$  and  $T_{min}$  has less than  $M_s$ . On the left of the table are listed the various materials tested. The cobalt plated specimens all had  $Al_2O_3$  dispersed in the Co plate.

With three temperature ranges and six materials, there are 18 boxes in

Table VI.  
Identification of Test Conditions for Specimens

		Temperature Range		
		Below $A_1$	Above $M_s$	Through $A_1$ and $M_s$
Bare	Gun Steel	CT - valid AH, AI, - no load AB, AW, AX, AZ - Freon	AT, BG, BJ - valid AS - water	BI, BK - valid AJ, AK AR, BA - no load AY
	4340 Steel	BV - valid	BW - valid	BQ, BX - valid CQ, CR, CS - water
Chromium	Gun Steel	BB - valid AP, AQ - Freon	BH, BL - valid	AU, AV - valid
	4340 Steel	AA - no load		
Plated	Gun Steel	AM, AN - Freon		CF - valid
	4340 Steel	BO - valid	BN, BR - valid BF - bad plate	BS - valid
Cobalt plus Chromium Plated	Gun Steel			
	4340 Steel			

Table VI, one for each combination of material and temperature range. In each box are listed the specimens tested using their letter description from Table III. In each box are listed first the specimens that were tested under conditions that should give a valid result. These specimens are designated "valid" and were tested using air cooling with constraint during the test. Also listed in each box are the specimens tested under conditions such that the result is not a valid constrained thermal fatigue test. The principal reason they are not considered valid is listed after the specimen letters. The specimens tested with water or Freon 11 injection were suspected to have failed due to attack by the fluid. Many of the specimens tested under no load were also cooled with water or Freon 11, so they are invalid for more than one reason.

With a few exceptions, only the specimens in Table VI designated "valid" are discussed below. The exceptions are as follows: Specimen AA, Cr plated 4340, was tested under no load, so the mechanical results have no meaning. However, the Cr plate did show some interesting cracking patterns and the microscopic examination results are discussed later. Specimen AN, Co + Cr plated gun steel, was cycled for ten cycles and the test stopped before fracture. Thus, though cooled by Freon 11, the electroplate was never exposed to Freon 11 and the microscopic examinations on this specimen are valid. Specimen BT would have been a valid test. However the Cr plate on this specimen did not completely cover a portion of one end. This distorted the heating pattern because of uneven induction, ruining the specimen.

From Table VI it is apparent that valid tests were obtained for both bare gun steel and bare 4340 steel. Except for specimen AA, no Cr plated

4340 specimens were tested because a valid test was obtained for each temperature range with Cr plated gun steel. Because of scheduling and time problems, it was not possible to obtain sufficient Co/Cr plated gun steel specimens for test in each range. Therefore a complete series of Co/Cr plated 4340 steel specimens was tested.

The results of the thermal fatigue tests are presented in the five subsections which follow. First, the test parameterics for the valid test specimens from Table VI are presented. In the succeeding three sections the microscopic observations are presented for bare steel, Cr plated steel, and Co/Cr plated steel. In the final section the results for Ta-10W are presented.

3.4.1 Thermal Fatigue Parameters. The actual thermal fatigue test parameters for the valid tests of specimens listed in Table VI are given in Table VII. The specimens are listed in that order in which they appear in the boxes of Table VI. There are five sections in Table VII, corresponding to each of the material combinations tested (no tests for Cr plated 4340). For each specimen the specimen designation, the temperature range, the percent constraint in addition to thermal strain, the maximum tensile load, and the maximum compressive load are listed. The last three parameters are summarized for three stages of the test, early, midway and late in the test. Finally a comment on the mode of failure is made.

There are several points to note in the results presented in Table VII. First, the maximum tensile and compressive loads remain about constant until near the end of the specimen life, when they fall off more and more rapidly until the final specimen failure. The constraint remains fairly constant

TABLE VII  
TEST PARAMETERS FOR STEEL THERMAL FATIGUE TESTS

Specimen	Temp. Range	Cycle No.	Constraint (%)	Load (lbs)	
				Tensile	Compressive
<b><u>BARE GUN STEEL:</u></b>					
CT	390	2	0.19	2300	480
	1230	50	0.18	2220	550
		90	0.15	600	100
		94	Specimen cracked		
AT	640	2	0.68	1320	650
	1415	11	0.71	1350	810
		22	0.79	1380	820
			No separation		
BG	615	2	0.24	690	175
	1435	27	0.24	90	470
		53	0.24	10	300
			100% tensile load drop		
BJ	600	1	0.86	1900	1140
	1375	7	0.81	1850	1100
		13	0.79	1620	950
			Specimen separation		
BI	375	2	0.08	1300	200
	1435	16	0.08	1350	250
		18	0.19	1370	430
		86	0.19	1470	480
		133	0.15	490	70
		117	Specimen separation		

TABLE VII (cont'd)

Specimen	Temp. Range	Cycle No.	Constraint (%)	Load (lbs)	
				Tensile	Compressive
BK	360	2	0.10	1720	690
	1405	17	0.10	1560	690
		34	0.10	1450	700
Test stopped. No separation					
<u>BARE 4340 STEEL:</u>					
BV	470	2	0.15	970	350
	1315	100	0.16	900	270
		218	0.13	360	130
		218	Specimen separation		
BW	610	2	0.22	920	220
	1420	140	0.22	580	190
		318	0.19	500	390
		390	Test stopped. Specimen broken at room temperature.		
BQ	325	2	0.80	1200	200
	1425	10	0.88	1100	200
		19	0.84	1300	550
			Specimen separation		
BX	475	40	0.36	720	440
	1390	420	0.36	690	780
		800	0.37	300	80
		800	Test stopped. Specimen necked down		
<u>CHROMIUM PLATED GUN STEEL:</u>					
BB	465	2	0.20	2560	890
	1270	20	0.23	2400	680
		70	0.22	2100	610
		124	0.22	1820	520
		124	Specimen fractured.		

TABLE VII (cont'd)

Specimen	Temp. Range	Cycle No.	Constraint (%)	Load (lbs)	
				Tensile	Compressive
BH	635	2	0.17	900	370
	1440	6	0.16	850	300
		10	0.16	800	350
			Test stopped.	No separation.	
BL	640	2	0.18	1100	450
	1460	130	0.21	840	340
		258	0.24	650	340
			Test stopped.	No separation.	
AU	350	2	0.16	1800	1100
	1440	13	0.16	1900	1150
		25	0.16	2200	1140
			Specimen separation.		
AV	435	1	0.19	1350	400
	1465	5	0.16	1250	370
		10	0.12	1300	280
			Test stopped.	No separation	
<u>COBALT-CHROMIUM PLATED GUN STEEL:</u>					
AM	320	2	0.68	1700	850
	1250	13	0.68	1900	700
		25	0.67	2050	875
			Specimen separation		
AN	160	1	0.78	2870	1360
	1215	5	0.67	2800	1100
		10	0.70	2730	1200
			Test stopped.	No separation	

TABLE VII (cont'd)

Specimen	Temp. Range	Cycle No.	Constraint (%)	Tensile	Load (lbs) Compressive
CF	340	5	0.26	1800	270
	1415	40	0.19	1490	270
		65	0.19	1680	470
		66		Plating flaked and test stopped.	
<u>COBALT-CHROMIUM PLATED 4340 STEEL:</u>					
BO	440	2	0.32	1500	640
	1300	180	0.18	1130	390
		360	0.23	470	170
		361		Specimen separation	
BN	625	1	0.24	940	200
	1420	5	0.14	690	540
		10	0.12	220	500
				Test stopped.	80% load drop
BR	650	2	0.21	1650	450
	1435	40	0.22	1230	440
		79	0.28	950	400
				Test stopped.	No separation
BS	375	2	0.04	1000	700
	1450	116	0.14	720	190
		231	0.10	200	220
				Test stopped.	80% load drop

throughout the life. The variations in constraint in many cases are associated with small fluctuations in  $T_{max}$  and  $T_{min}$  as cycling proceeded.

The constraint calculation is based on the original diameter of 0.25 inch. Near the end of the specimen life the specimen cross-section typically severely distorts. The diameter usually remains approximately equal to the original diameter through the line of strain measurement, but bulges and distorts at right angles to this line. Under these conditions the actual constraint being applied to the specimen is not well defined.

A second important point is that the total number of cycles to failure for a given material is quite sensitive to the applied constraint. As the constraint is reduced from 0.8% to 0.2% the specimen life increases quite markedly. Not enough experiments have been performed to thoroughly explore this constraint dependence but it is clear that the dependence is strong.

It also appears from the tests on bare steel that for the same constraint conditions gun steel has a shorter thermal fatigue life than 4340 steel. This may be due to different high temperature flow stress for the two materials. Also it is possible that 4340 may soften more rapidly than gun steel at higher temperature, ie. that the resistance to flow of the 4340 is lower than for the gun steel. Part of the apparent difference in results between gun steel and 4340 may be only superficial, however, because there may be systematic differences in the applied strain for the two materials. Because of the strong constraint dependence of thermal fatigue life, small differences in constraint can cause large differences in life.

A final point to note with regard to Table VII is the effect of the temperature range on the total life. For the gun steel, cycling above  $A_1$  and below  $M_s$  on each cycle appears to appreciably reduce total life as compared to cycling entirely below  $A_1$  or cycling entirely above  $M_s$  with  $T_{max}$  above  $A_1$ . The probable reason for this is that going through the phase transformations on each cycle requires the presence of a considerable strain component to remain on the desired smooth diameter-temperature curve. This puts appreciable work into the specimens on each cycle, thereby promoting crack propagation and other degradation mechanisms. This result is not as clear cut for the 4340 steel; in fact, there is some indication that cycling all above  $M_s$  is more severe in terms of reduced life than cycling through  $A_1$  and  $M_s$ . It also appears that the effect of the phase transformations is fairly large and could well stand further study.

3.4.2 Bare Steel Microscopic Results. This section describes the typical observations of the changes in microstructure and the failure mechanisms for thermally cycled bare steel. Figure 14 shows SEM observations of the surface of specimen BK after cycling both above  $A_1$  and below  $M_s$ . The roughened surface structure is due to the sand blasting given the specimen before attaching the thermocouples. This structure persisted throughout the test but did not appear to contribute to the specimen failure.

Figure 15 shows micrographic results for specimen BV, 4340 steel cycled below  $A_1$ . Figure 15a is an optical micrograph showing a change in structure of the tempered martensite. The martensite has further tempered during cycling. A decarburized layer has formed on the inner specimen surface due to the exposure to air at high temperature. The inner surface typically

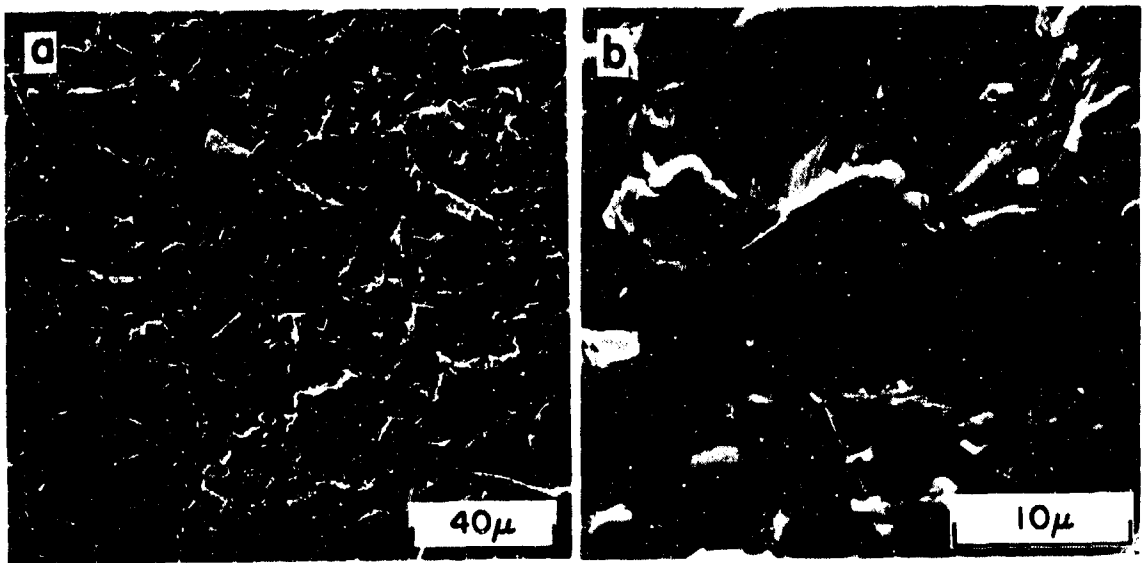


Fig. 14 Scanning electron micrographs of sandblasted structure on the surface of specimen BK.

42-a

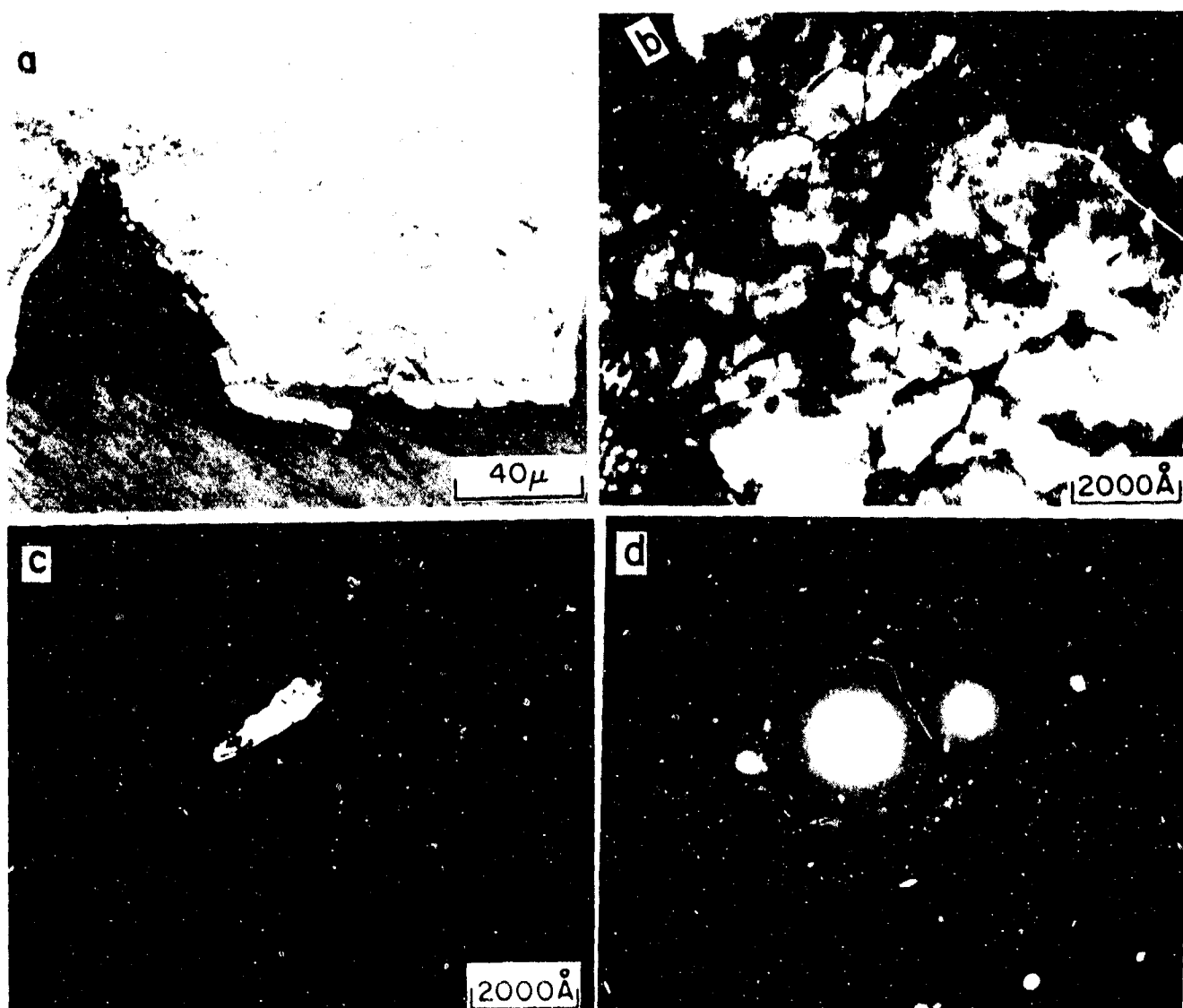


Fig. 15 Microstructure of specimen BV. a) Optical micrograph of inner surface; b) transmission micrograph of bulk structure; c) dark field view of carbide particle; d) diffraction pattern of area in b).

42-6

showed large cracks on cycling below  $A_1$ . The decarburized layer extends into the crack tip, indicating that the decarburization and cracking occur together, rather than one greatly preceding the other. Specimens cycled below  $A_1$  appear to have all failed from the inside out. Figures 15b and c are transmission electron micrographs of the same material. In Figure 15b the bright field view shows the steel structure after the further tempering and working of the thermal cycling. A dark field view of a carbide particle is shown in Fig. 15c; the carbide particles have considerably enlarged as compared to the fatigued material, Fig. 7. Figure 15d is a electron diffraction pattern which still shows strong carbide as well as martensite matrix reflections.

Specimen BJ is gun steel, cycled above  $M_s$  and above  $A_1$  so the structure in the heated zone was austenite during the cycling. On cooling back to room temperature, the austenite transformed to martensite, whose structure is shown in Fig. 16a and b. Figure 16c is a transmission micrograph of this structure, showing that many large carbide particles have grown. They show up in the electron diffraction pattern, Fig. 16d. This specimen failed after only thirteen cycles, so the particles had grown quite large after only a short time at temperature. Fig. 16a is a cross-section including the outer surface of BJ, showing no decarburized zone. The inner surface, Fig. 16b has a thin decarburized zone, but no deep cracks as observed on specimens cycled below  $A_1$ .

Figure 17 gives optical micrographs for the outer surface (17a) and inner surface (17b) of specimen BW, 4340 steel cycled above  $M_s$  and above  $A_1$ . This again shows the martensitic structure of 4340. The inner surface, Fig. 17b, has a thick layer of decarburized material since this specimen was

thermally fatigued for 280 cycles. This specimen shows no appreciable cracking from the inside surface.

To illustrate direct observation of specimen failure from outside-in, the fracture of specimen BJ is shown in scanning electron micrographs in Fig. 18. The fracture originated at the external surface of the specimen and propagated inward forming large stepped shear areas in the specimen center.

Specimens tested above  $A_1$  and below  $M_s$  are shown in Figures 19-22. Data for gun steel specimen BK are shown in Fig. 19. The optical micrograph, Fig. 19a, shows the martensite structure formed on cooling. This is similar to the structure of specimens thermally fatigued all above  $M_s$ , Fig. 16. The transmission micrograph, Fig. 19b, shows carbide particles, which also show up on the diffraction pattern, Fig. 19c.

In Figure 20 are shown optical micrographs of specimen AY. This specimen was tested with Freon, so it is not a valid test. The test was stopped, however, before fracture, so the Freon did not affect the structure of the specimen center shown in Fig. 20. Figure 20b is the microstructure of the center of the heated section; it is untempered martensite formed on cooling. Figure 20a shows the microstructure just outside the heated zone, where the temperature did not exceed  $A_1$  during test. This structure is similar to that of the specimen cycled below  $A_1$ , Fig. 15a, i.e. tempered martensite.

Figure 21 shows optical micrographs of specimen BX, 4340 steel cycled through  $A_1$  and  $M_s$ . This also shows the essentially untempered martensitic structure formed on cooling. The outer surface is shown in Fig. 21a and is smooth. The inner surface, Fig. 21b, exhibits some cracking similar to but not as severe as that in specimens tested below  $A_1$ . This specimen also

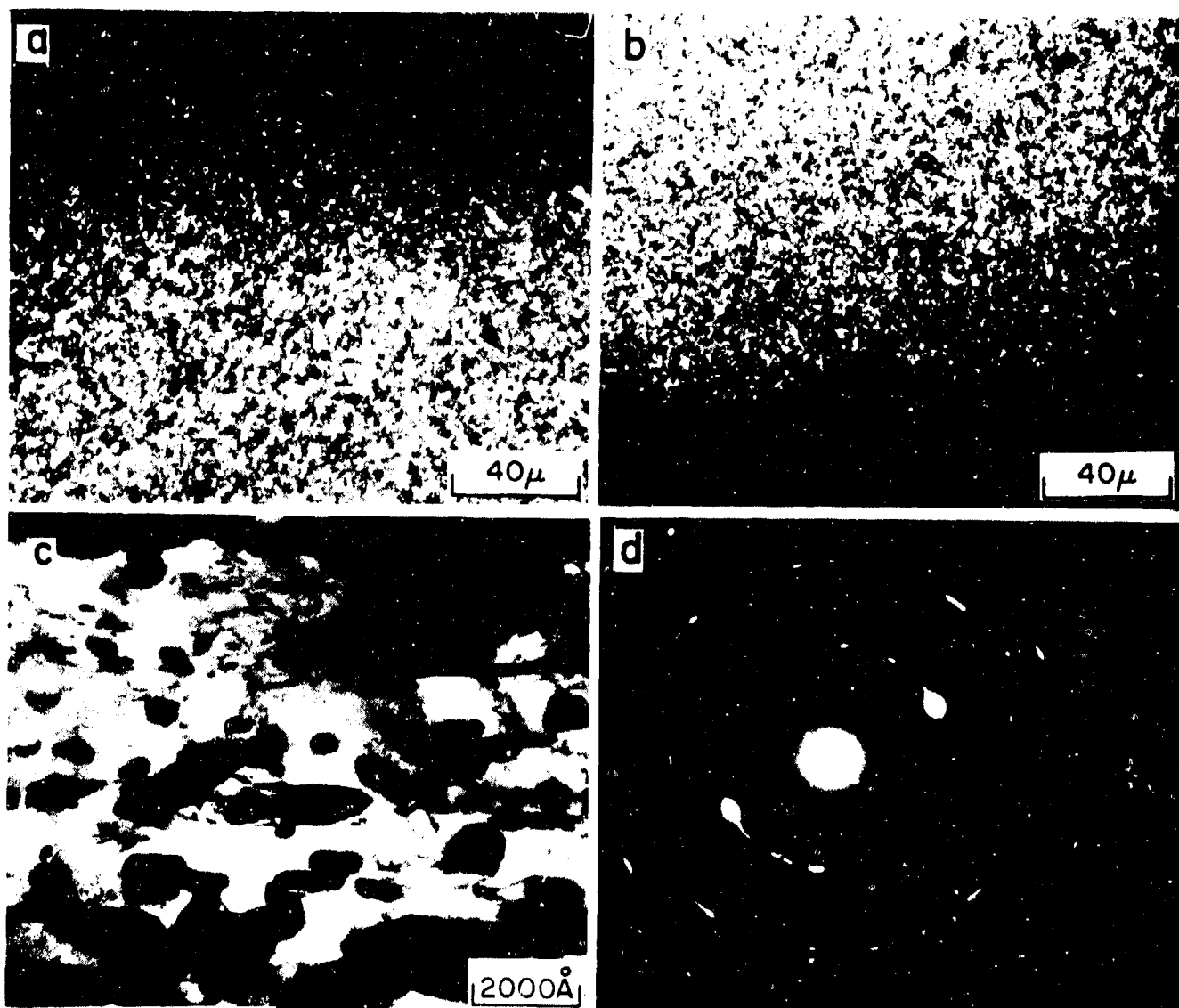


Fig. 16 Microstructure of specimen BJ. Optical micrographs of a) outer surface; b) inner surface; c) transmission micrograph of bulk area; d) diffraction pattern of area c).

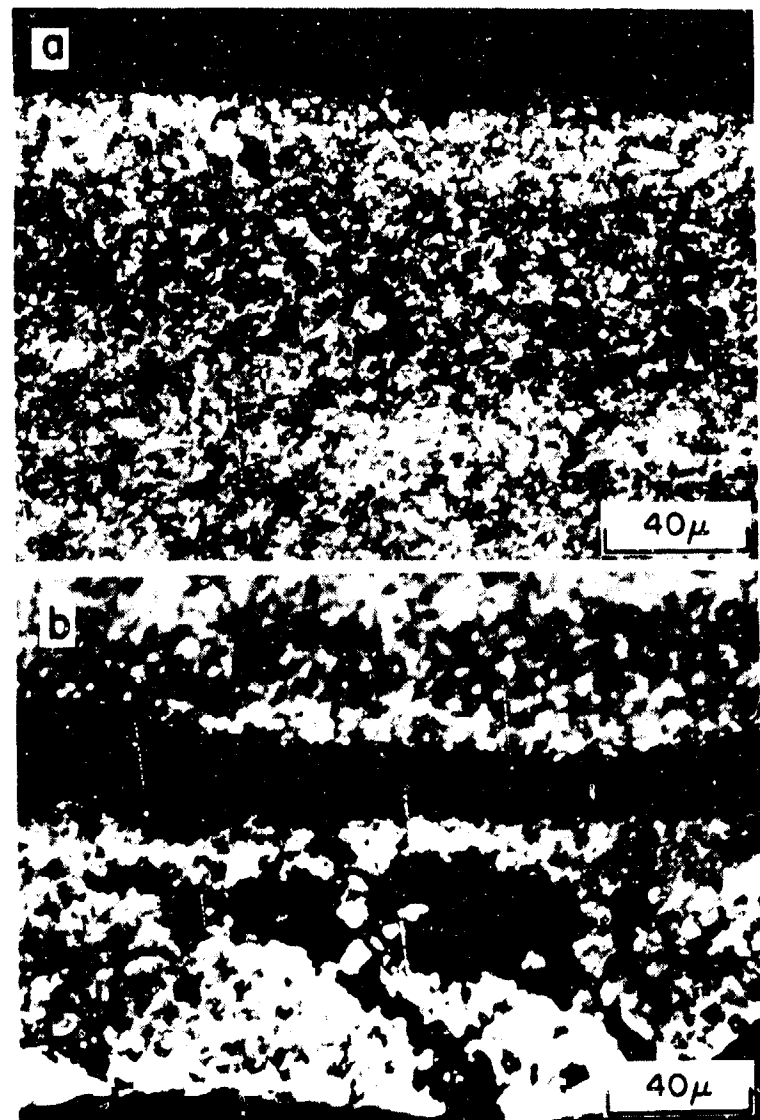


Fig. 17 Optical micrographs of specimen BW. a) Outer surface; b) inner surface.

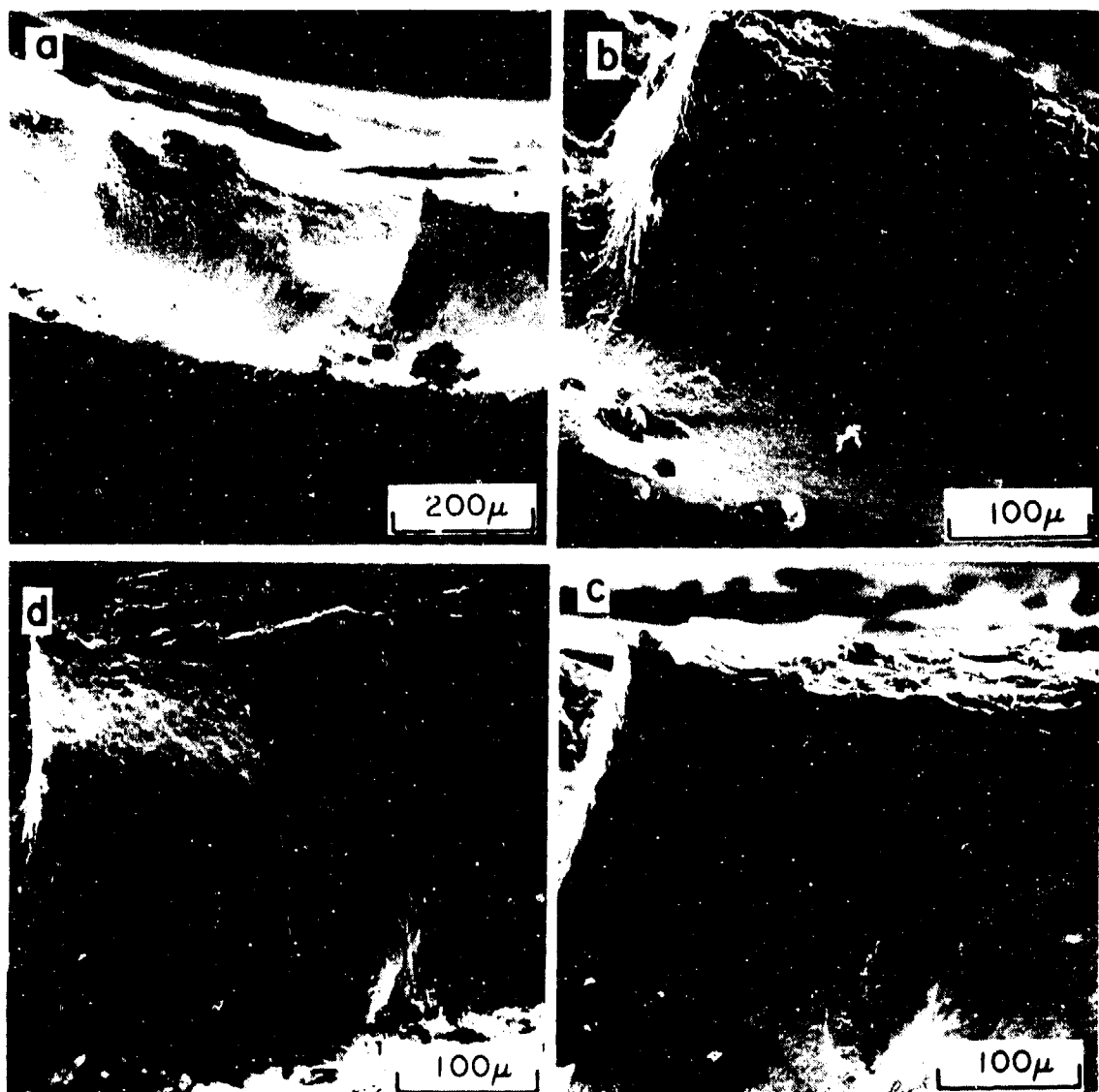


Fig. 18 Scanning electron micrographs of the fracture surface of specimen BJ.

44-c

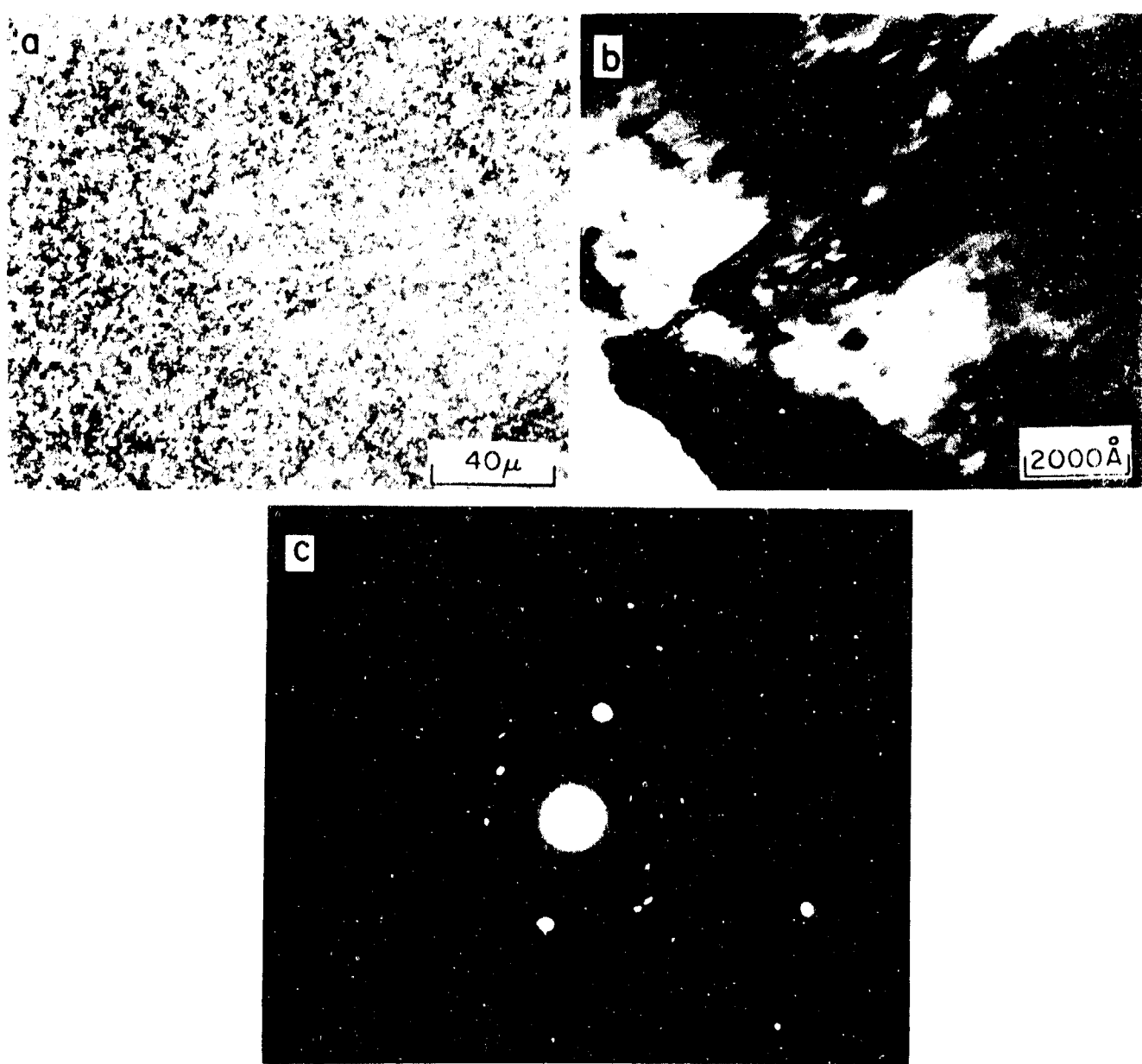


Fig. 19 Microstructure of Specimen BK. a) Optical micrograph of bulk  
b) transmission micrograph of bulk; c) diffraction pattern of  
area b).

44-d

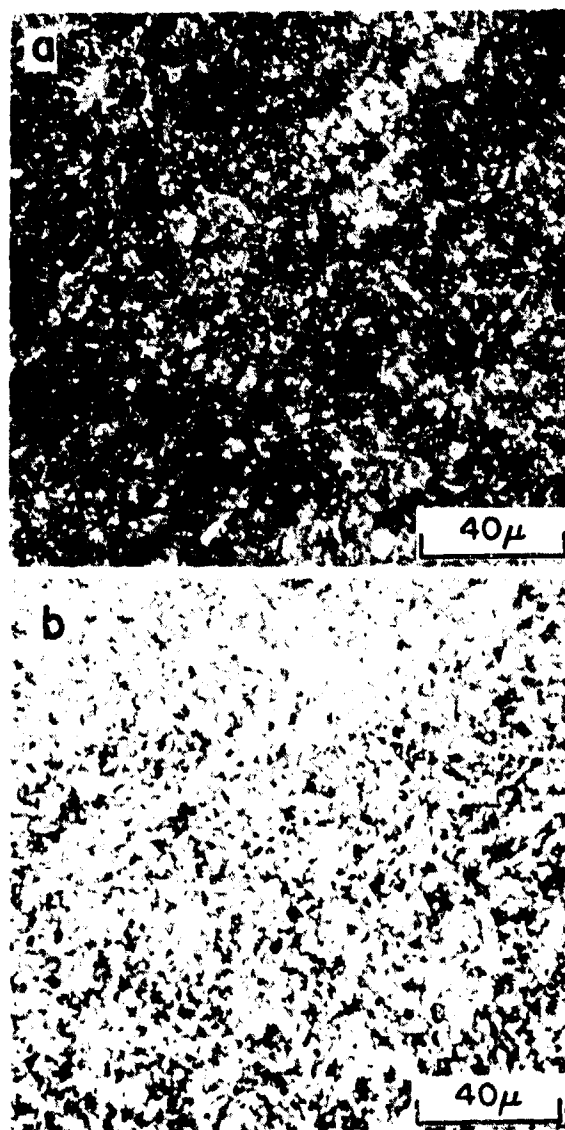


Fig. 20 Optical micrographs of specimen AY: a) away from hottest zone; b) center of hottest zone.

44-2.

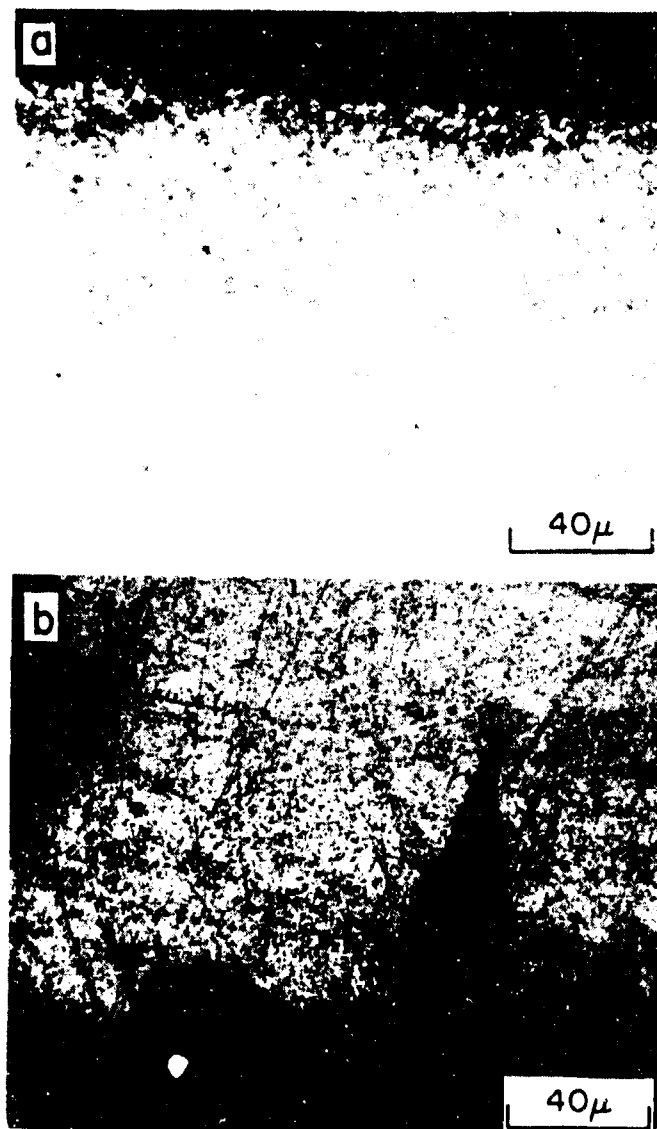


Fig. 21 Optical micrographs of specimen BX: a) outer surface; b) inner surface.

44-f

shows a decarburized layer on the inner surface.

Figure 22 presents scanning electron micrographs of specimen BK, gun steel tested though  $A_1$  and  $M_s$ . These views are of the inner surface of the specimen and show oxide particles and cracks. The cracks are similar to those of Fig. 21. The cracked oxide particle layer is fairly thin and is often found to partially flake off as seen for specimen BW in Fig. 17b.

In summary, a decarburized layer is found to form on the inner surfaces of the thermally fatigued steel specimens which grows with increasing exposure time. Specimens cycled below  $A_1$  show extensive cracking on the inner surface, and specimens cycled above  $A_1$  and below  $M_s$  show inner surface cracking to a lesser degree. Steels thermally fatigued above  $A_1$  and above  $M_s$  do not exhibit this internal surface cracking, and typically crack from the outside in or fail by gradual necking of the cross section. The expected process of coarsening of carbide particles in the two steels is noted for thermal fatigue through  $A_1$  - above  $M_s$  and through  $A_1$  - below  $M_s$ .

3.4.3. Chromium Plated Steel Microscopic Results. The Cr plated specimens that were thermal fatigue tested are identified in Table VI. The pertinent test data have been given in Table VII. Eight specimens constituted the test set analyzed; of these, specimen AP was tested for the temperature range below  $A_1$ . Freon gas was used as the cooling agent during the cool down portion of the thermal cycle. This specimen failed after 22 cycles and energy dispersive x-ray analysis shows that the fracture surfaces were heavily incrusted with metallic chlorides. The data for this specimen therefore has limited value, and are not discussed further.

The remainder of this section deals only with the results obtained from seven thermal fatigue specimens designated BR, AO, BH, BL, AU, AV and AA. Of the seven specimens, five (BB, BL, BH, AU, and AV) were cooled with air

during the cool down portion of the thermal cycle. These, then, are as free from the effects of chemical attack from the cooling agent as can practically be achieved at the Science Center with reasonable cool down times. Specimen AQ, though cooled with Freon, was not fatigued to failure and consequently the Cr plate and plate/steel interface region is free from contamination.

The thermal fatigue results have been divided into two categories. First is the mechanical test data which were summarized in Table VII. The remaining results are the extensive materials degradation observations obtained for each specimen. These two categories of results are coupled in a complex way. Our interest is in evaluating Cr plating failure, and the number of cycles at failure has meaning in this respect only if it is somehow associated with a degradation of the Cr plate or the Cr/steel interface. So, for instance, specimen BB apparently failed by crack propagation initiating from the inside of the hollow test specimen. Thus, although degradation had occurred in the plate and plate interface near the outside of BB, this contributed only in a minor way to the failure at 124 cycles. This, in turn, compounds the job of comparison of degradation mechanismson an equal footing from specimen to specimen.

As a consequence, one can not rely on the numerical failure values alone. Extensive post fatigue microscopic materials characterization was required to provide a data base for comparison of plating failure under the selected test conditions and to define potential plating failure mechanisms. Several important failure mechanisms have been identified for the Cr plate/gun steel system and will be discussed in turn.

3.4.3.1. Chemistry Related Interfacial Structural Change. Evidence has been found to support the view that a significant modification of the chemistry

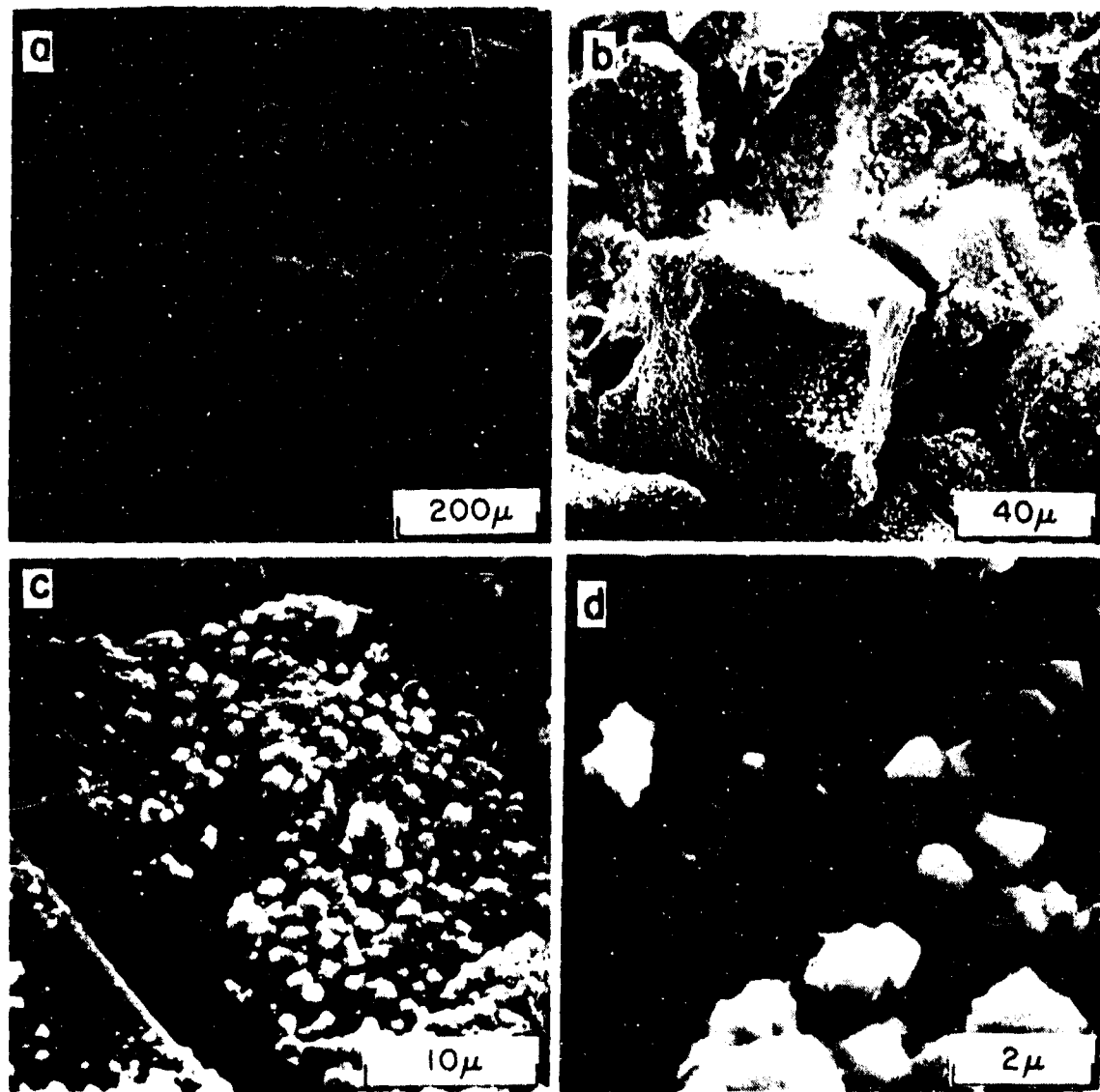


Fig. 22 Scanning electron micrographs of inner surface of specimen BK showing cracks and surface oxide particles.

and associated structure of both the gun steel and the Cr plate occurs due to carbon diffusion across the steel/Cr interface during thermal fatigue. The consequence is the formation of chromium carbide in the Cr near the interface with a concomitant reduction in carbon content in the gun steel near the interface. This process is expected to result in the embrittlement of both the gun steel and the Cr at the interface and consequently to play a major role in the process of flaking and debonding of the Cr plate from the steel. This mechanism has not been found to be active in specimens BB, AQ, and AA cycled only below  $A_1$ , but is, inferentially, present in the remaining test specimens, and is apparently more extensive for the two cycled both through  $A_1$  and  $M_s$ .

The possibility that an alteration of the near interface gun steel indeed does occur was first noted on electro-polished sections of test specimens observed with scanning electron microscopy. A narrow band in the steel at the interface was found to preferentially etch in the polishing solution utilized. Figure 23 shows a comparison of preferential etch zone size for specimens BH and AV. In all micrographs, the Cr layer is on top. Both specimens were sectioned and then electropolished as described earlier. The bulk of the steel is only lightly etched by the etching used. Typical of the polished bulk gun steel structure is that at the arrow in micrograph 23c. Near the Cr interface, the steel is heavily etched in a zone corresponding roughly to the lighter area below the Cr in 23a and 23c. Arrows in 23a and 23c indicate the approximate lowest point of penetration of this zone. The apparent depth of these zones is of reasonably uniform thickness across the specimens. The depth of the altered zone indicated by etching is roughly 0.4 mils for BH cycled 10 cycles through  $A_1$  but above  $M_s$ , and is roughly 4.5 mils for specimen AV cycled 10 cycles both through  $A_1$  and  $M_s$ . In actuality, a

sharp zone demarcation does not exist but instead, the fraction of steel heavily etched decreases with increasing distance from the interface. Particularly for the specimens cycled both through  $A_1$  and  $M_s$ , the apparent zone depth is a function of both etch time and etch conditions, which could contribute as much as 50% error to the zone depth estimate. Irregardless, the zone is significantly deeper for specimen AV than for BH.

In contrast, Fig. 24 shows the electropolished interface for specimen AQ cycled with 0.8% plastic strain for 10 cycles for a temperature always below  $A_1$ . No preferential etching of the steel is seen and the lightly etched steel structure is similar to that for the bulk steel for specimens BH and AV. The light/dark areas particularly noticeable in 24a have nothing to do with the etch, but instead are the result of variations in corrosion product coating thickness on the steel. Likewise, the apparent light band in the Cr just above the steel is an artifact of the viewing angle used in making the micrographs.

As noted above, the heavy etching zone is also seen in specimens BL and AU that were cycled to failure, through  $A_1$  - above  $M_s$  and through  $A_1$  - through  $M_s$ , respectively. Specimen AU lasted only 25 cycles and within the error attributable to etching conditions the zone depth is the same as for AV. Specimen BL lasted 282 cycles and significant changes in the heavy etching zone are noted. The average depth increased as shown in Fig. 25a and b, but the extent of the pitting within the zone decreased. It is uncertain if this is intrinsic to the test or the result of a slight variation in etching conditions. Additionally, sizeable regions of expanded etching are noted in association with points of penetration of cracks from the Cr into the gun steel. This is particularly the case where significant branch cracking in the steel is present. Figure 25c and d illustrate this observation. Typical interface heavy etch zone depth is 0.7 mils for specimen BL, except in regions

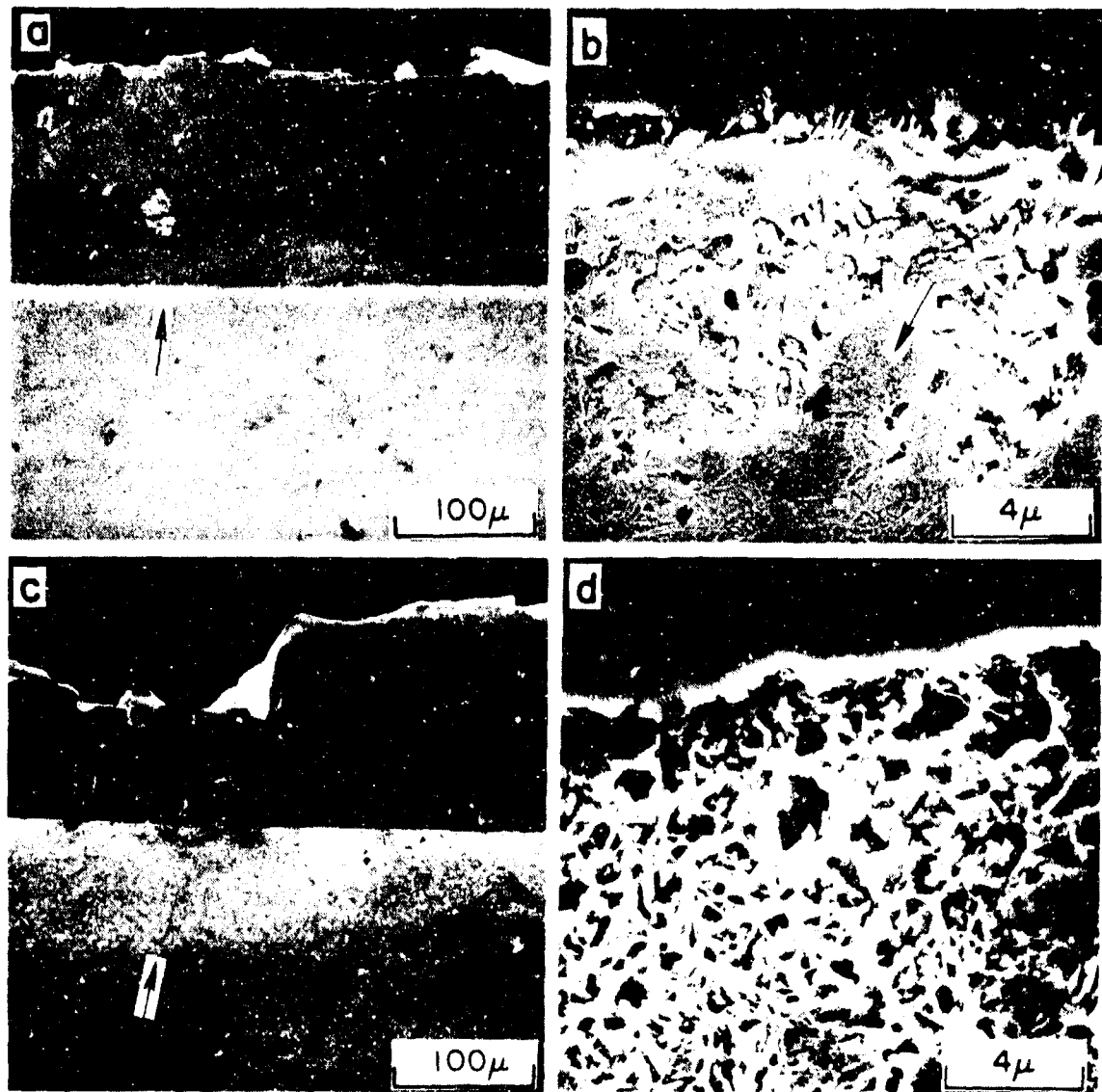


Fig. 23 Scanning electron micrographs of altered zone in the steel at chromium/gun steel interface seen in electropolished sections:  
a) For specimen BH, arrow at deepest penetration distance of zone of heavy etch; b) high magnification of region in (a), arrow at etch structure typical of bulk material; c) for specimen AU, arrow at deepest penetration distance of zone of heavy etch; d) high magnification of region in (c) showing heavily etched altered zone. Chromium at top.

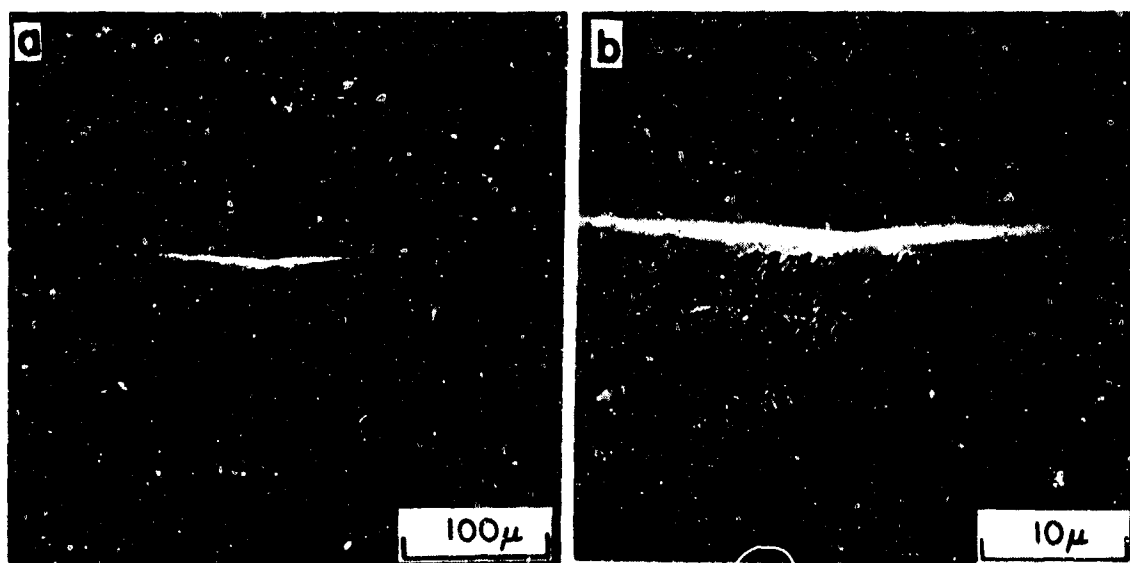


Fig. 24 Scanning electron micrographs of chromium/gun steel interface seen in electropolished sections of specimen AQ, cycled only below  $A_1$ . No altered zone is observable in the steel at the interface. Chromium at top.

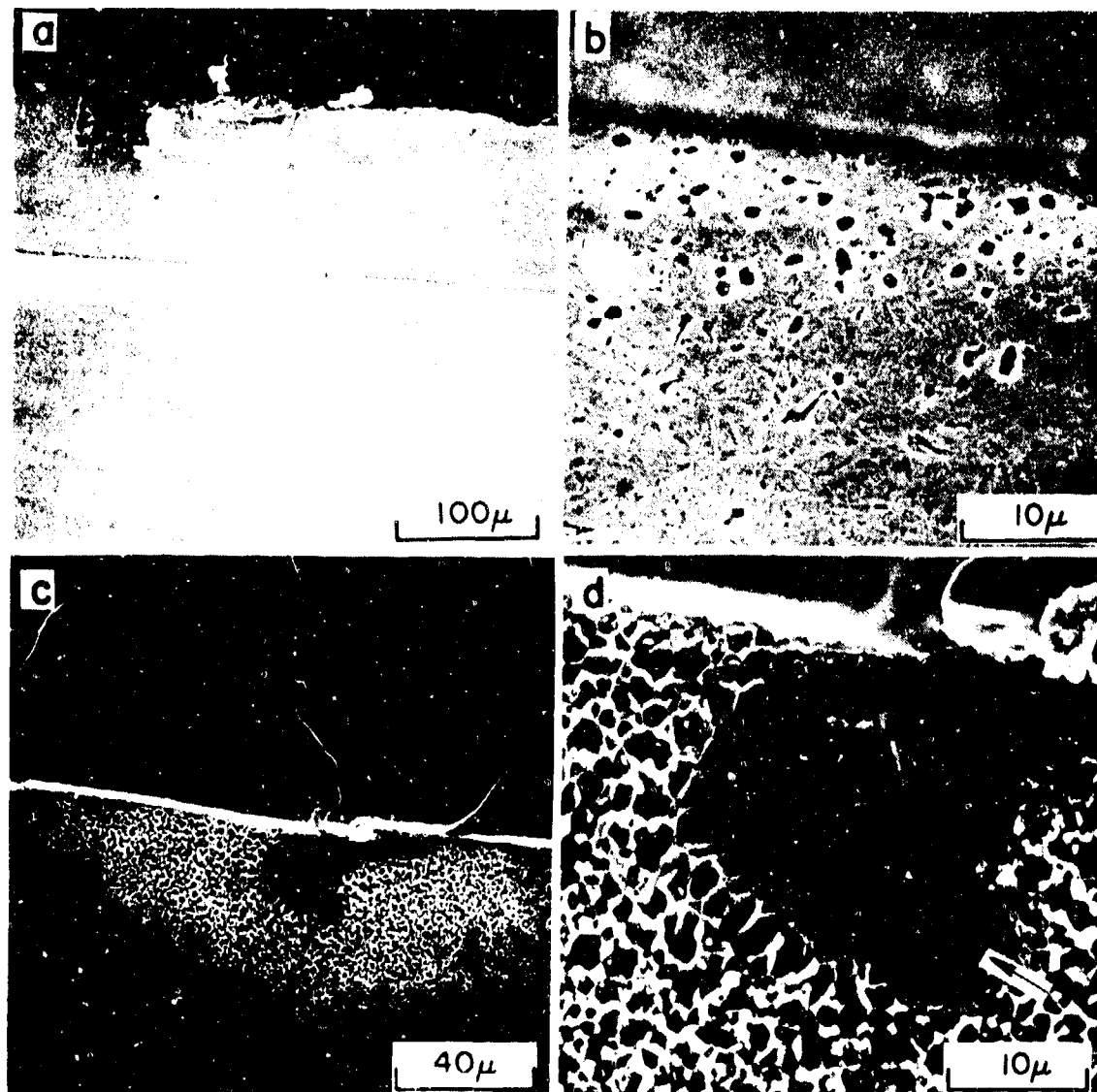


Fig. 25 Scanning electron micrographs of chromium/gun steel interface seen in electropolished sections: a) & b) For specimen BL showing slight increase in depth of altered zone over that for specimen BH cycled for 10 cycles over the same temperature range; c) & d) showing expansion of the altered zone at point of passage of crack in the chromium into the gun steel. Arrow in (d) at microcracked region having increased chromium content.

such as in 25c and 25d, where the zone thickness associated with the crack in Fig. 25c is 2.5 mils. Energy dispersive x-ray analysis using the SEM shows that the central zone in 25d, indicated by the arrow, is especially rich in Cr (i.e., more so than for the gun steel itself). No other chemistry shifts were detectable in the interface region using this unit, but the system is particularly insensitive to analysis for low atomic number elements.

It was initially speculated that the altered zone was the result of differential thermal expansion effects due to the phase changes in the steel encountered during thermal cycling. This is, at least, consistent with the lack of apparent damage for the three specimens cycled entirely below  $A_1$ , and with the apparent increased damage for specimens AU and AV. While differential thermal expansion is probably a contributing factor, analysis of the Cr/steel interface of specimen BL using transmission electron microscopy (TEM), has shown an additional mechanism to be active. A chemical alteration of the Cr near the Cr/steel interface has been detected which is attributed to the formation of  $Cr_7C_3$ , one of the several carbides Cr can form. Figure 26 shows a transmission micrograph taken in the Cr layer near the interface and Fig. 27 a corresponding dark field micrograph. An electron diffraction pattern of the Fig. 26 region is shown in Fig. 28a. For purposes of comparison, the diffraction pattern in Fig. 28b is one from the Cr layer taken near the Cr/Co interface of the Co-Cr plated specimen identified as BR (this is discussed in the following section). The pattern in 28b is essentially that of body centered cubic Cr as expected for electro-deposited Cr. The only anomaly is the presence of a few diffuse rings which are attributed to the formation of corrosion products during the electro-thinning process used for specimen preparation. Figure 28a is taken with roughly the same camera constant and when the diffuse rings are neglected the remaining pattern gives a reasonable

fit to  $\text{Cr}_7\text{C}_3$ . The few minor discrepancies can be attributed to substitution of other metals for Cr in the  $\text{Cr}_7\text{C}_3$  lattice. Comparison with patterns for other Cr and Fe carbides yields no other match. Referring again to Figs. 26 and 27, the entire region is essentially polycrystalline  $\text{Cr}_7\text{C}_3$  with the bright laths particularly noticeable in the dark field micrograph being zones of larger  $\text{Cr}_7\text{C}_3$  crystallites. The location of the pictured area, with respect to the interface, is not precisely known due to difficulties encountered in the specimen preparation process. The Cr near the interface is heavily micro-cracked, requiring the electro-thinning of extremely small fragments. It can be estimated, however, that the particular region was at least within 0.25 mils of the interface and probably much closer.

It was also possible to obtain a near interface analysis of the gun steel for specimen BL. Figure 29 shows a comparison between the gun steel of specimen BL near the Cr/steel interface 29a with that for a similarly thermally fatigued unplated gun steel specimen, BG (29b). Figure 30a and b gives sample corresponding diffraction patterns. In 30b, in addition to the matrix spots, a large unit cell sub-lattice is detectable. For the plated steel only scattered reflections can be illuminated. The principal reason is seen in Fig. 29. In the thermally cycled bare gun steel, precipitates of various metallic carbides are sufficiently small to be transparent and thus are detectable with electron diffraction. In contrast, for the near interface steel of BL, the particulate matter has conglomerated into larger, nontransparent particles which yield poor electron diffraction results. To summarize the above observations, both the Cr and the steel have been altered, as a consequence of chemical and mechanical activity at the interface. There has been a diffusion of carbon from the steel into the Cr, resulting in the formation of  $\text{Cr}_7\text{C}_3$  at the interface and a concomitant reduction in carbon content in



Fig. 26 Transmission electron micrograph of chromium layer near to chromium/gun steel interface of specimen BL. The lath structure is apparently a single crystal of Cr<sub>3</sub>C<sub>2</sub>.



Fig. 27 Dark field transmission electron micrograph of region shown in Fig. 26 taken in matrix reflection of Cr-C.

70 - b

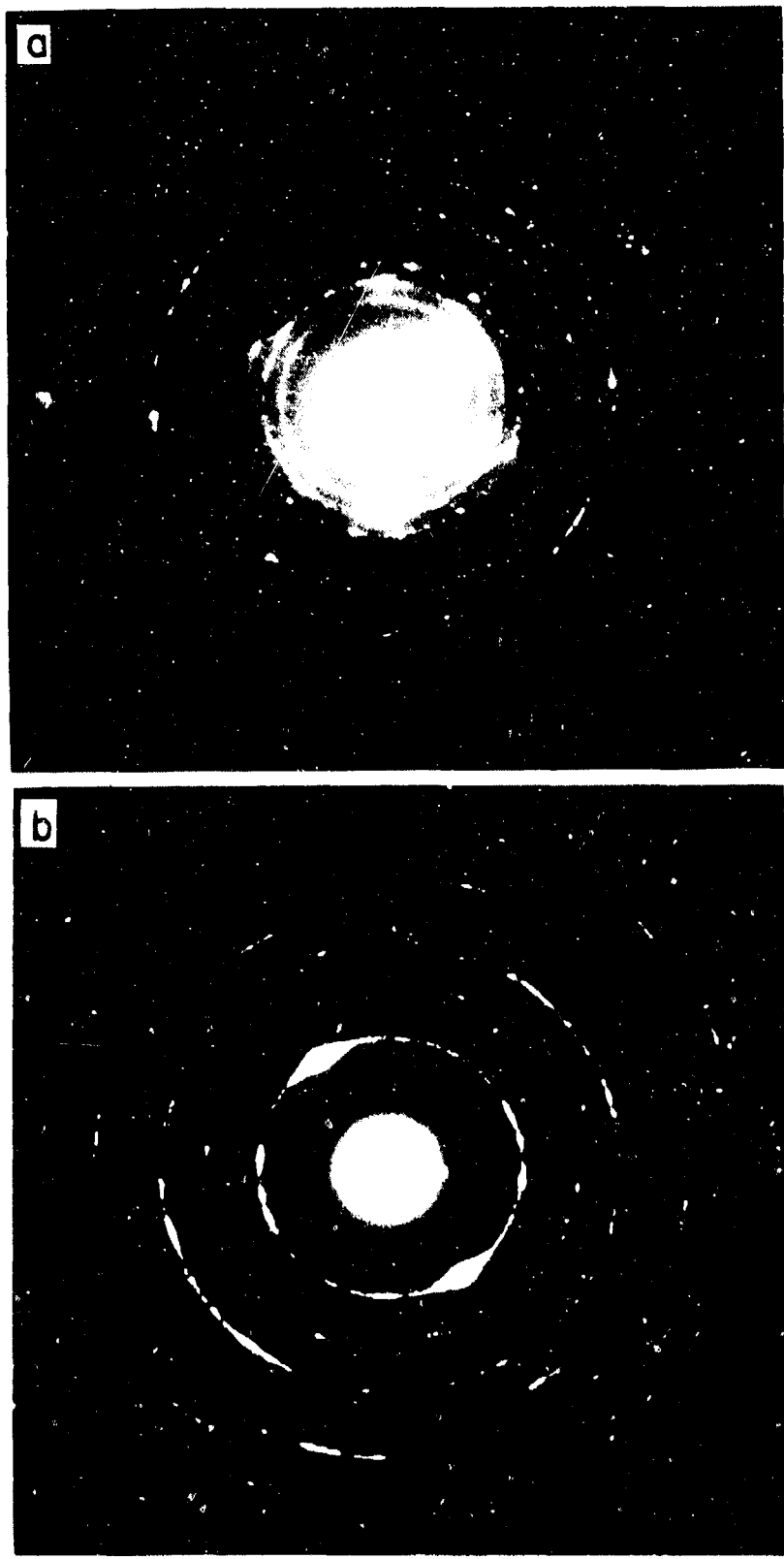


Fig. 28 a) Electron diffraction pattern of region shown in Fig. 26. In addition to the polycrystalline rings the matrix reflections of the crystal illuminated in Fig. 27 are visible. b) Comparison electron diffraction pattern taken in the Cr layer near the Cr/Co interface of specimen BK.

5 C 8'

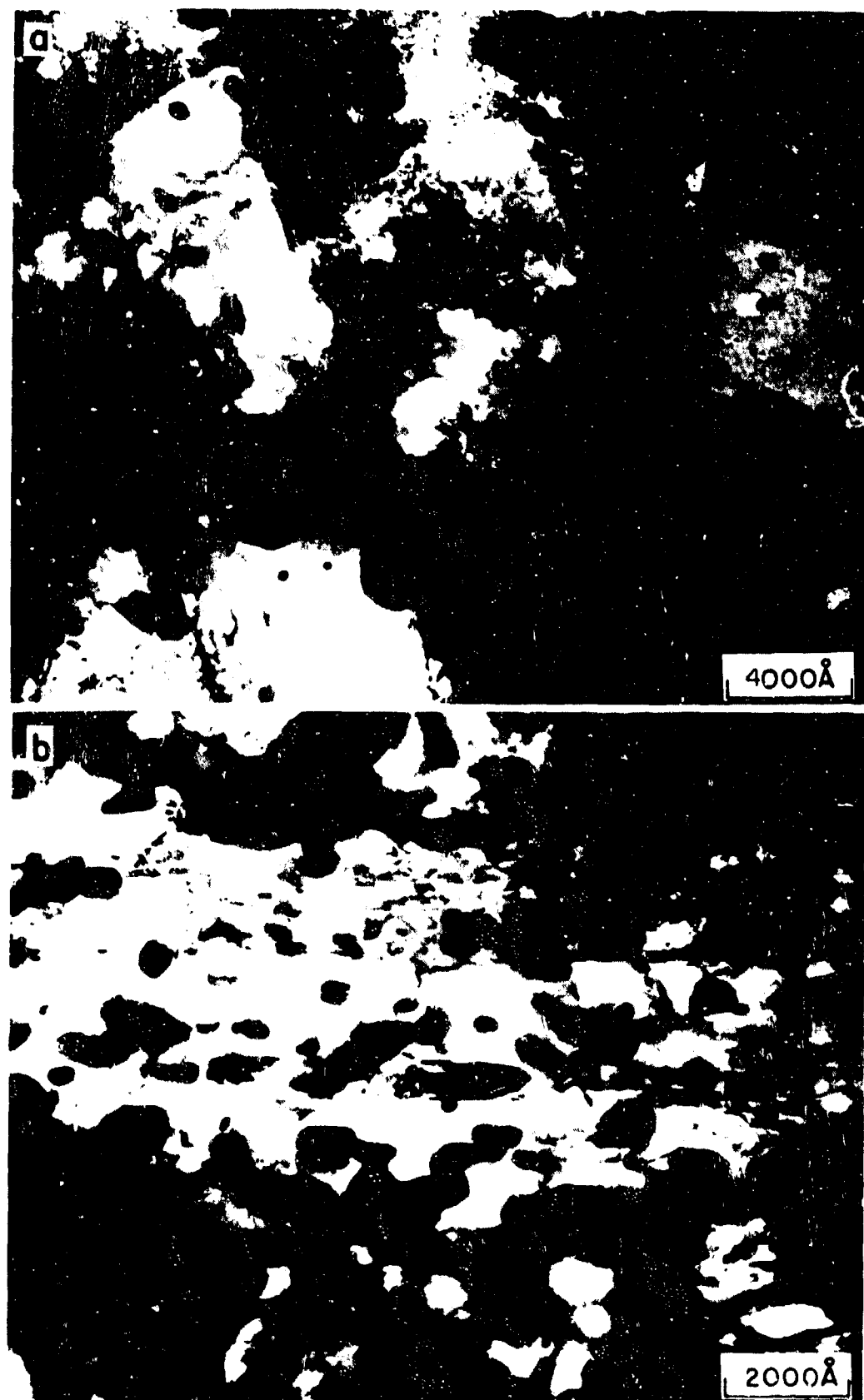


Fig. 29 Transmission electron micrographs of gun steel comparing the steel near the steel/Cr interface of specimen BL (a) to that for thermally fatigue unplated gun steel specimen, BG. (b) Precipitate density in (a) is significantly decreased.

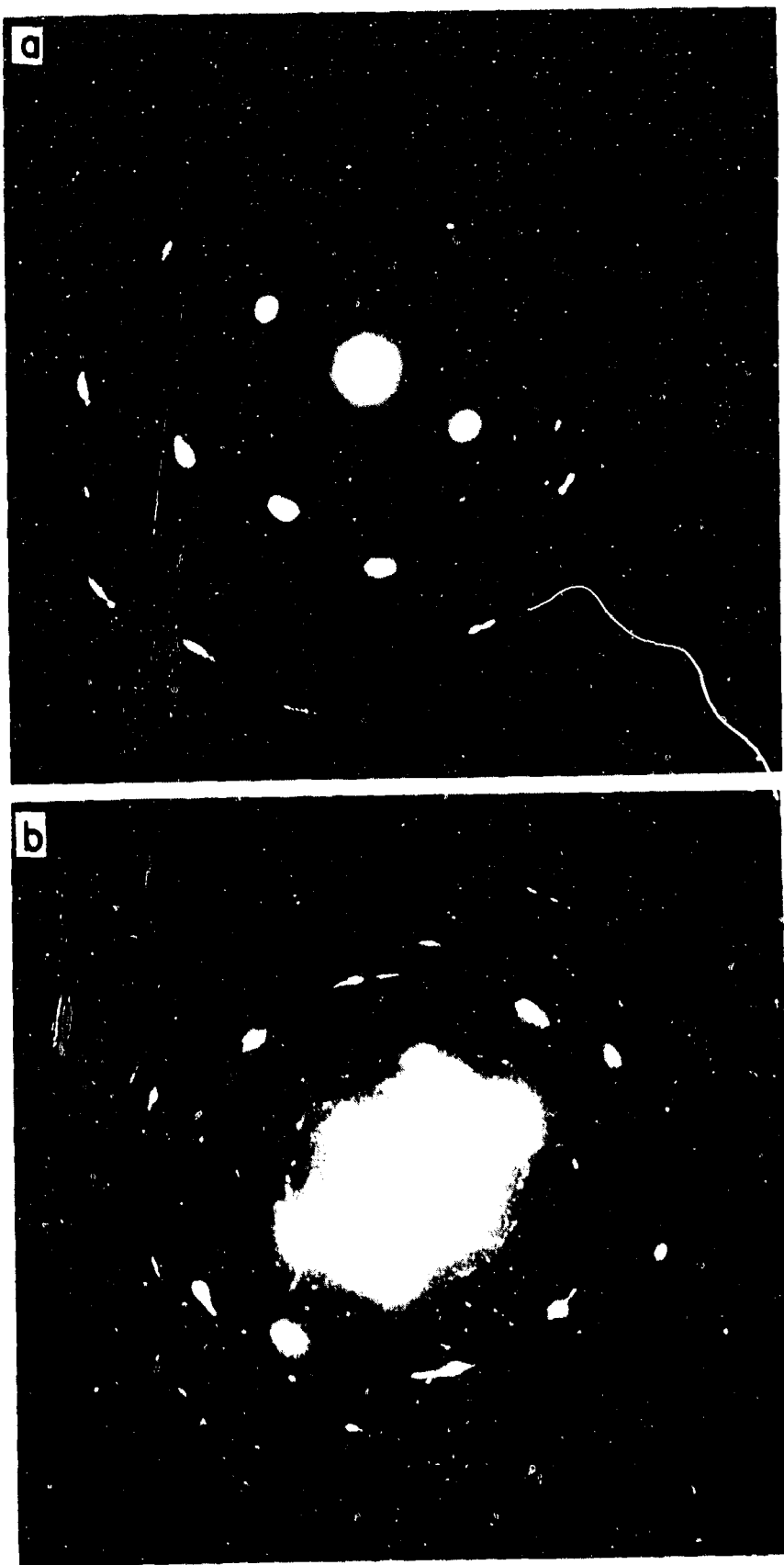


Fig. 30 Electron diffraction patterns corresponding to the micrograph regions in Fig. 29: a) specimen BL; b) specimen BG.

the interface steel. There has also been a diffusion of additional Cr into the steel and an apparent result is the conglomeration of the more finely dispersed precipitates typically seen in the bulk into larger conglomerates of carbides. This process has only been identified with specimens cycled so that the steel has undergone phase transformation, either through  $A_1$  or both through  $A_1$  and  $M_s$ , and seems to be more serious for the latter. There is no present evidence that this phenomenon is active for Cr plated gun steel cycled in thermal fatigue at temperatures always below  $A_1$ .

The only degradation that can be directly associated with this process for our imposed test constraints is microcracking of the steel at the Cr/steel interface. One sub-interface area preferentially identified as microcracked is shown in Fig. 31. Cracking in this zone is almost completely obscured by the concomitant etching, as in this etched section view, but is a bit more apparent on the steel fracture surface. Figure 32 shows a section of fracture surface of specimen AU. In these four views the Cr is at the top or top-left and particularly in 31a and 31b is seen to have a laminated structure and to be heavily cracked. The bands just below the Cr plate indicated by the arrows in 31c and 31d are found to be extra rich in Cr using energy dispersive x-ray analysis. In particular, the sub-Cr region in 31b appears to be heavily micro-cracked.

In contrast, Fig. 33 shows a section of the fracture surface of specimen BB, thermally fatigued below  $A_1$ . No zones comparable with those seen in Fig. 32 have been identified for this specimen. In particular, no zones in the steel just below the Cr plate have been found which are Cr rich. Again, some bonding structure is seen in the Cr plate.

3.4.3.2. Cracking and Deformation at the Cr/Steel Interface. As previously mentioned, cracks are found in the Cr plate which occur during the electrodeposition process. Even after one thermal cycle the stress fields associated with the tip of these cracks can produce significant deformation in the steel at the Cr/steel interface. This deformation and associated cracking has been seen to take different forms, depending on the temperature cycling and strain range selected. The number of tests conducted is insufficient to demonstrate whether the variations in deformation and cracking observed are indeed intrinsic to the test conditions, or rather due to some apparently minor variation in loading or specimen preparation. Nonetheless, because of the significant differences in near interface constraint for the three thermal cycling ranges examined in this effort, the possibility remains that these differences are real, and so they are reviewed here.

The observations are summarized in Table VIII and illustrated by the following eleven figures. The observations in Table VIII pertain to representative cracking through the Cr/steel interface which could potentially relate to debonding at the interface. In particular, differences are seen in the details of the deformation mode at the interface and the frequency with which significant crack propagation into the steel occurs. Exact comparison for failed specimens AU, BL and BB is not possible because of the differences in number of cycles to failure. In the case of specimen BB, the specimen failed by cracking from the inside. While specimen AU did fail because of cracking through the plate, the 25 cycles to failure is more a measure of the steel properties under those conditions than of Cr plate properties. The data for AU, BL and BB, however, illustrate the complexity of the interface cracking and deformation processes.

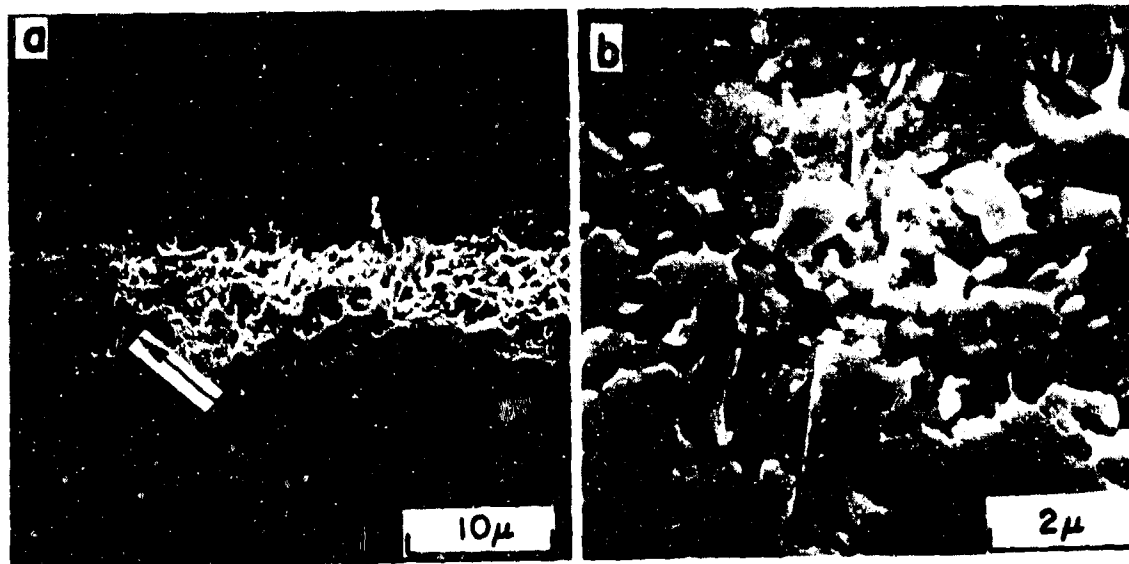


Fig. 31 Scanning electron micrographs of electropolished section of specimen BG showing apparent microcracking in altered zone not associated with Cr cracking. Arrow in (a) at region of high magnification in (b). Chromium at top.

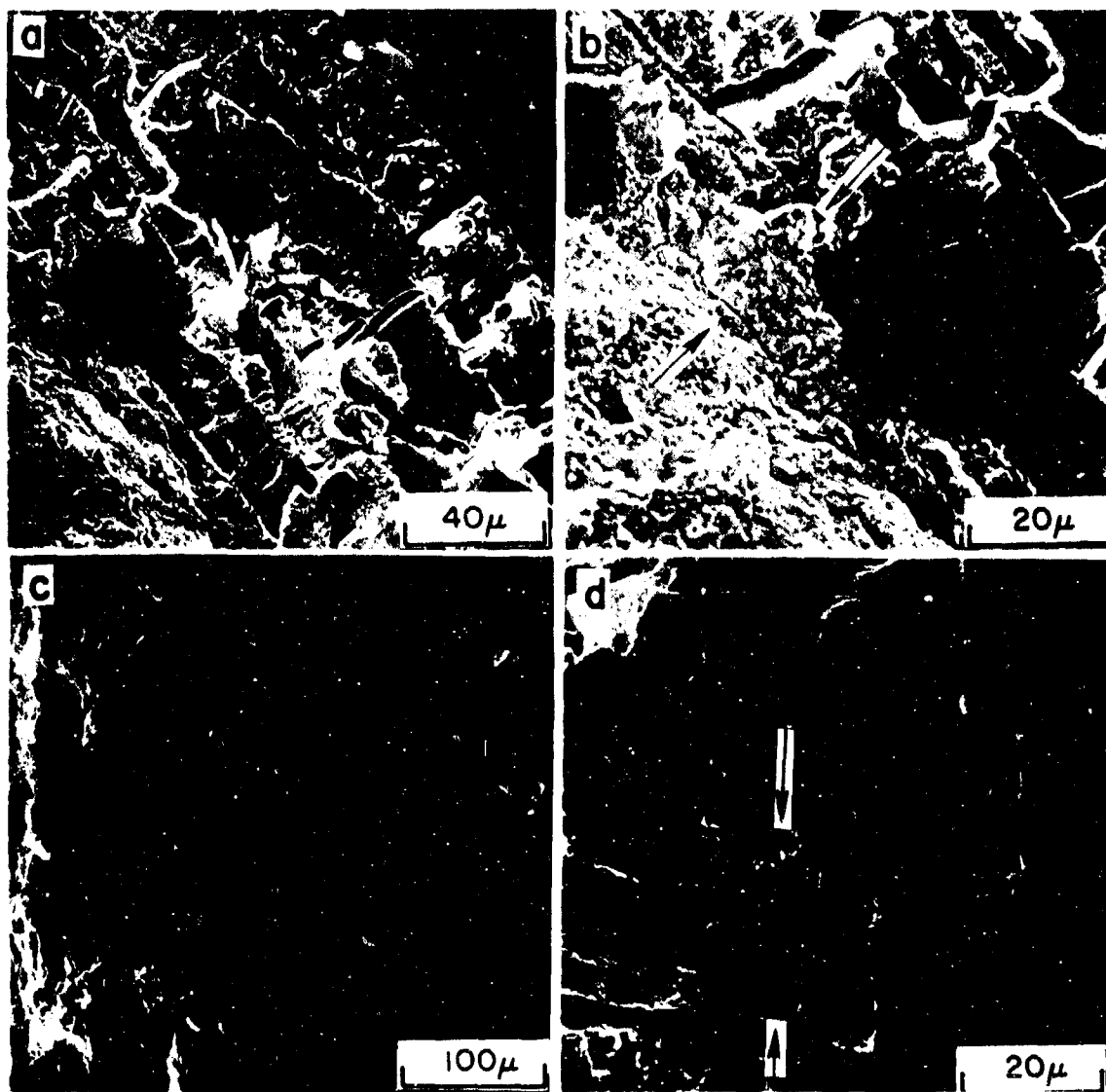


Fig. 32 Scanning electron micrographs of sections of fracture surface of specimen AU showing microcracked region in steel at Cr/steel interface: a) & b) region one, arrows in (b) define zone; c) & d) region two, arrows in (d) define zone.

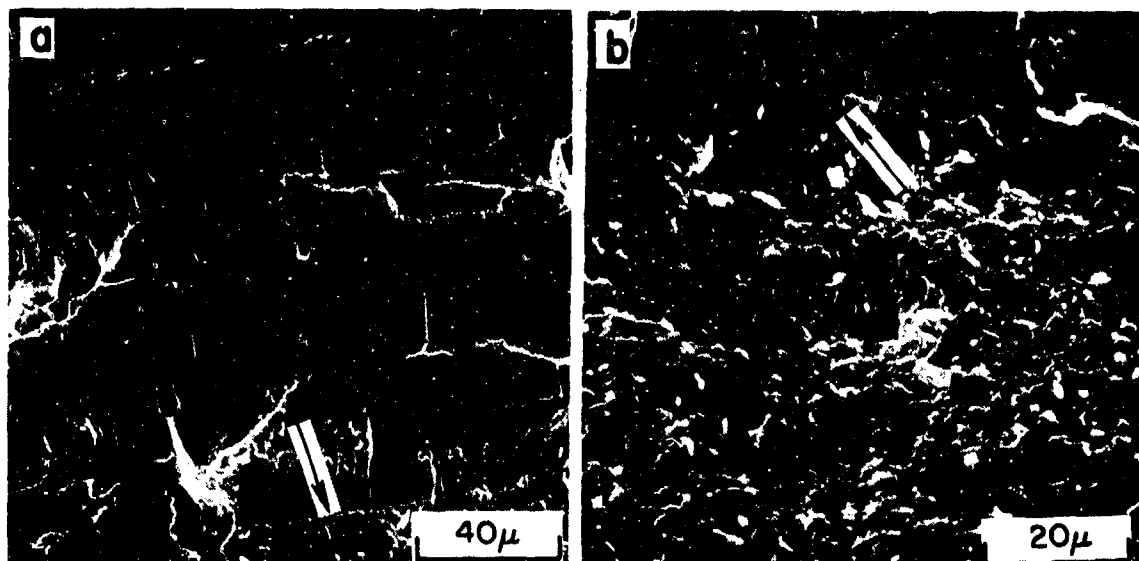


Fig. 33 Scanning electron micrographs of section of fracture surface of specimen BB. Arrows at Cr/steel interface. Cr on top.

TABLE VIII  
SUMMARY OF NEAR CR/STEEL INTERFACE CRACKING AND DEFORMATION

Test Condition	Thru $A_1$ Thru $M_S$ .2% Plastic $\epsilon$	Thru $A_1$ Above $M_S$ .2% Plastic $\epsilon$	Below $A_1$ .2% Plastic $\epsilon$	Below $A_1$ .8% Plastic $\epsilon$	Below $A_1$ 0% Plastic $\epsilon$
Specimen After 10 cycles	AV	BH	AQ		
	Crack blunting in steel & high steel interface deformation	Crack blunting in steel & little steel interface deformation	Cracking into steel & mod- erate to low steel interface deformation		
Specimen After n cycles	AU	BL	BB	AA	
	25 (failed) Cracking into steel.	282 (failed) Crack blunting high defor- mation at interface.	124 (failed) Crack blunting moderate undermining in steel	226 (terminated) Crack blunting in steel. Little defor- mation.	

Of particular importance, with regard to plating debonding, is interface undermining. Figure 34 of specimen AV shows a possible precursor of an undermining process. The plastic zones associated with two separated cracks are seen to have joined in only 10 cycles to form an extended plastic zone undermining the Cr plate. After 25 cycles, for the same test conditions (specimen AU), crack propagation past the interface (Fig. 35) had initiated resulting in almost immediate specimen failure.

The deformation history is quite different for the two specimens tested through  $A_1$  but above  $M_s$ . After 10 cycles the cracks in specimen one blunted at the Cr/steel interface and show little associated deformation (Fig. 36). For specimen BL, which failed at 282 cycles, the majority of the cracks remain blunted at the Cr/interface, although some through cracking was observed which accounts for specimen failure. As seen in Fig. 37, extensive deformation and folding is associated with the cracks at the interface and pinches of steel have been entrapped in the Cr in several instances.

Ten cycles at 0.8% plastic strain, below  $A_1$ , produced significant cracking into the steel as seen for specimen AQ (Fig. 38). At a lower strain (0.2%) specimen BB failed after 124 cycles. No crack penetration into the bulk of steel is seen for this specimen which failed because of crack propagation from the inside of the specimen. There is a significant amount of undercutting associated with the blunting of the Cr cracks in the steel for specimen BB (Fig. 39). The free expansion run made below  $A_1$  was terminated after 226 cycles. For this specimen (AA) cracks in the Cr remained blunted at the Cr/steel interface and no significant associated deformation is observed, (Fig. 40). This specimen has an un-heat-treated 4340 steel substrate.

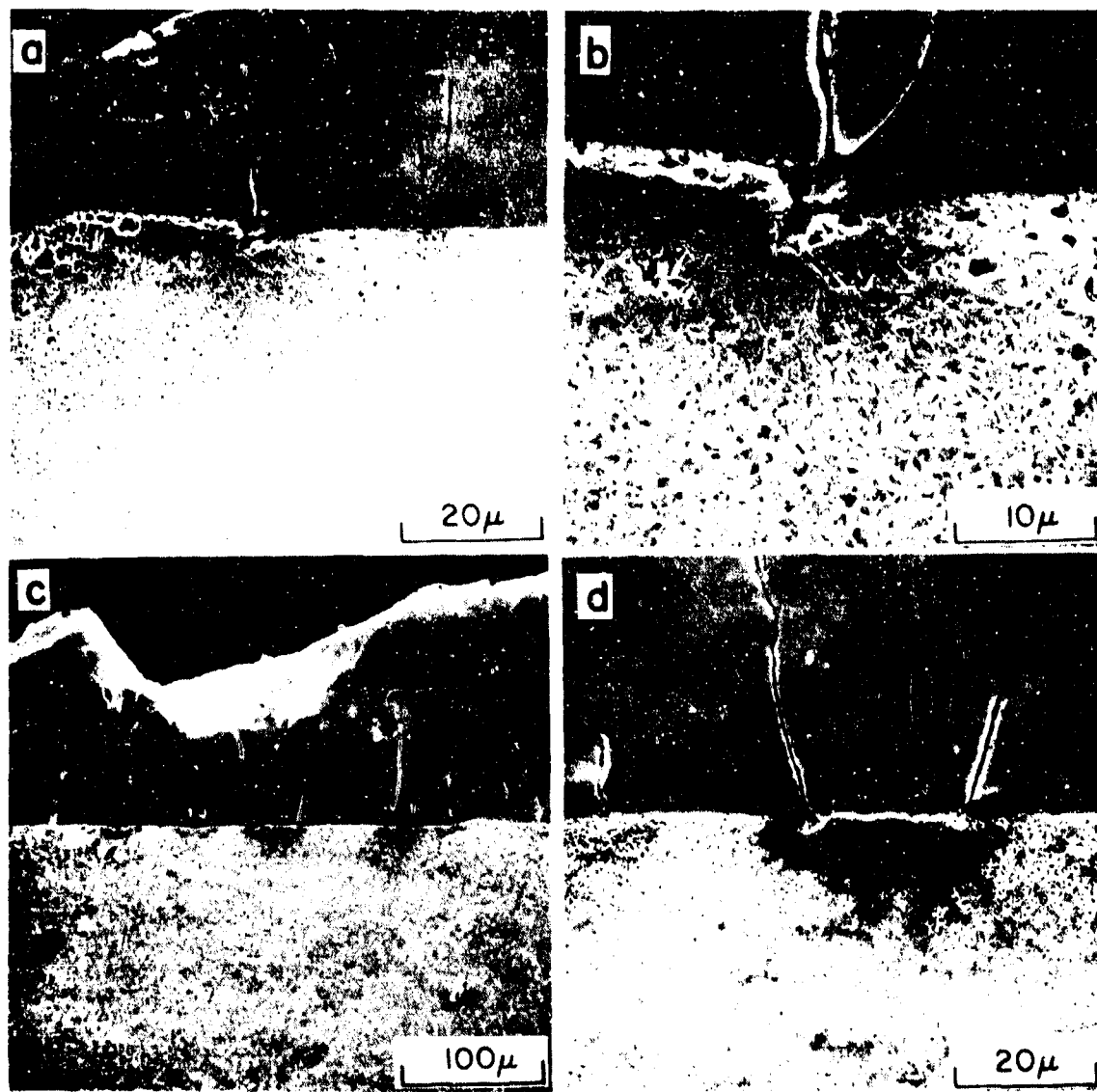


Fig. 34 Scanning electron micrographs of electropolished section of specimen AV. Connection between sub Cr plastic deformation zones can be seen associated with cracks in the Cr plate, Cr on top.

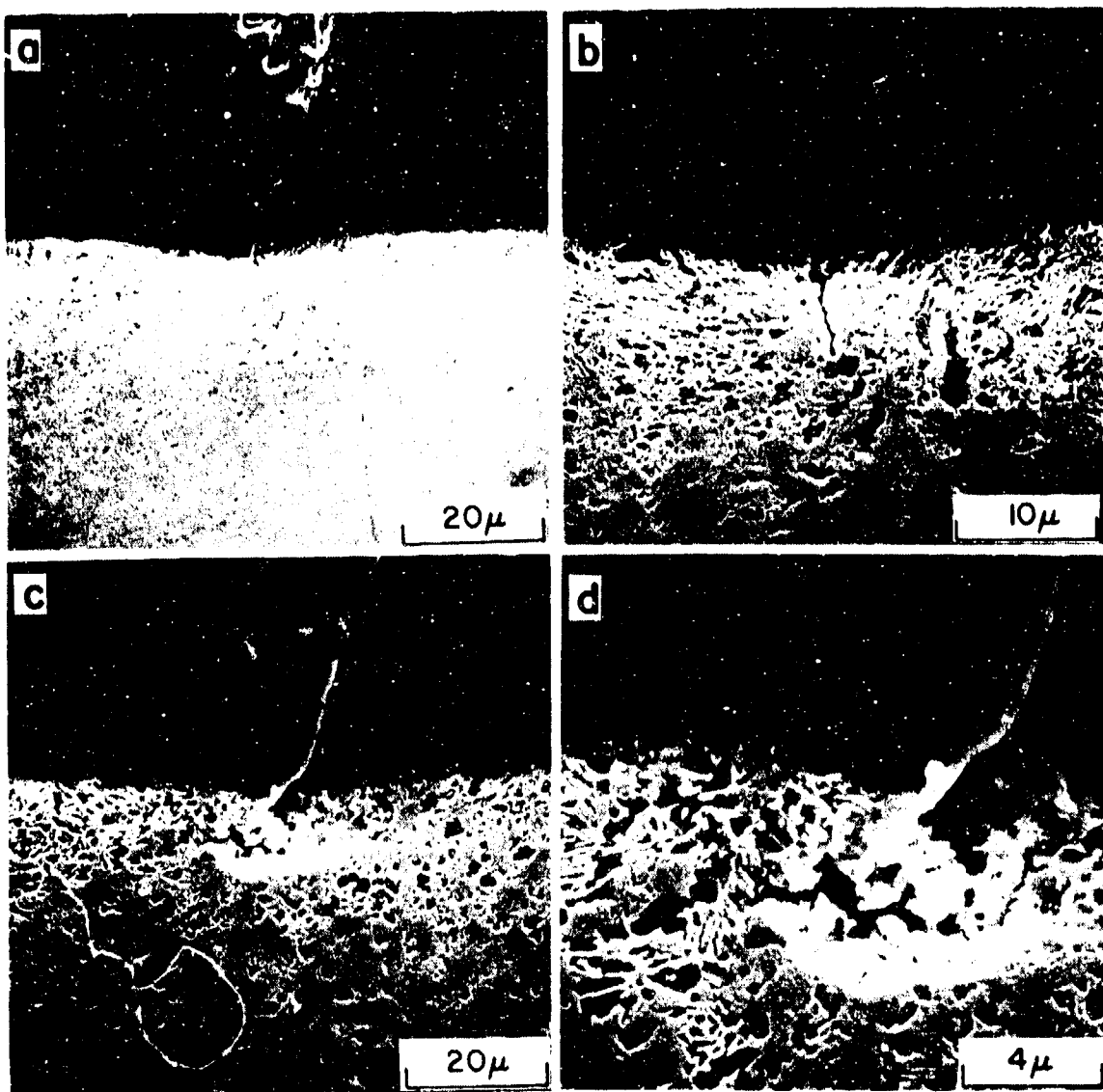


Fig. 35 Scanning electron micrographs of electropolished section of specimen AU showing crack propagation into the steel after 25 test cycles. Cr on top.

54 b



Fig. 36 Scanning electron micrograph of electropolished section of specimen BH showing crack blunting at Cr/steel interface. Cr on top.

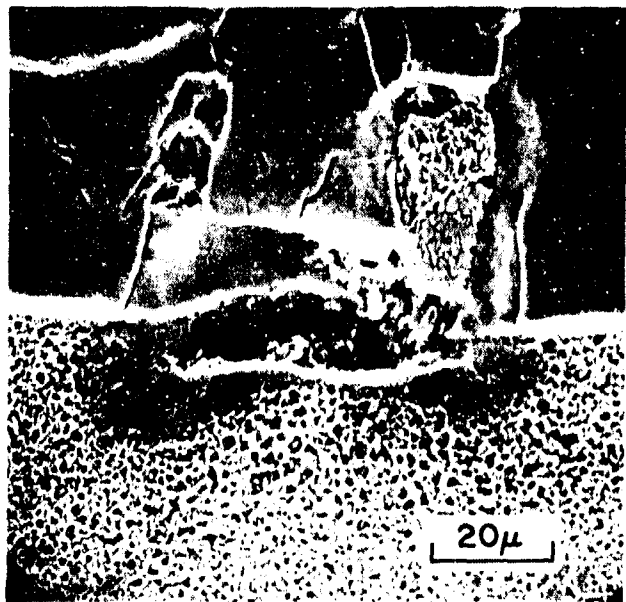
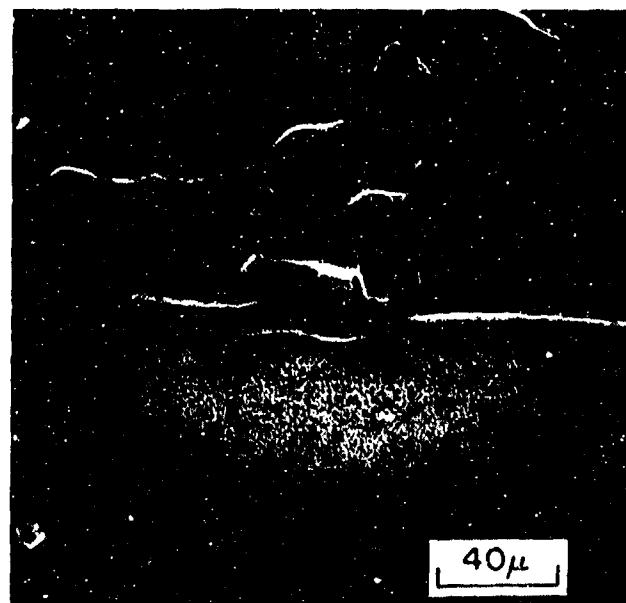


Fig. 37 Scanning electron micrographs of electropolished section of specimen BL. In addition to the heavy deformation in the steel a pinch of steel can be seen in the Cr plate. Cr on top.

54-d

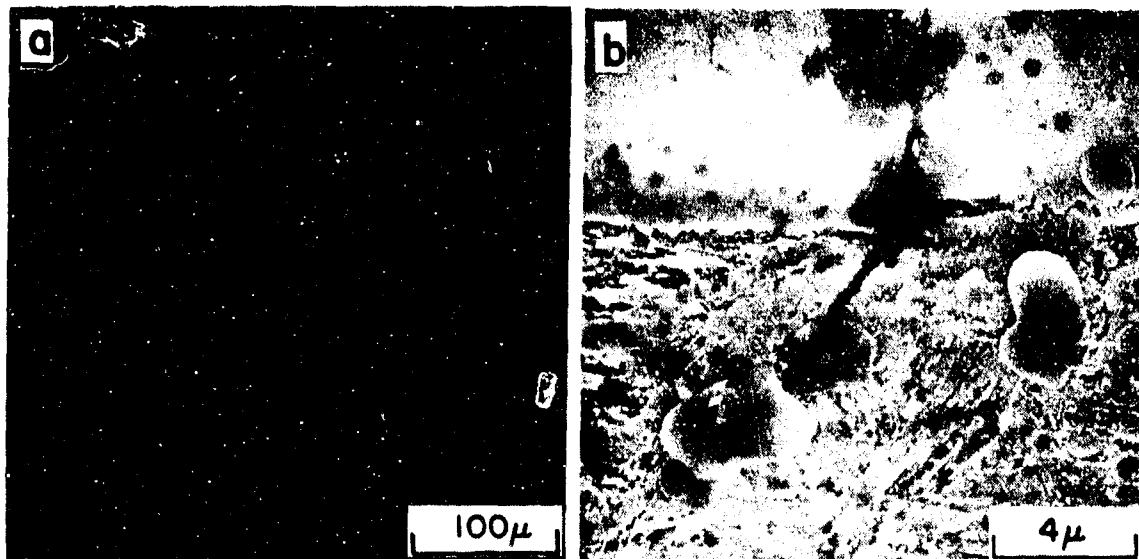


Fig. 38 Scanning electron micrographs of electropolished section of specimen AQ. Crack propagation through the Cr/steel interface is seen for this test condition and little associated deformation is noted. Cr on top.

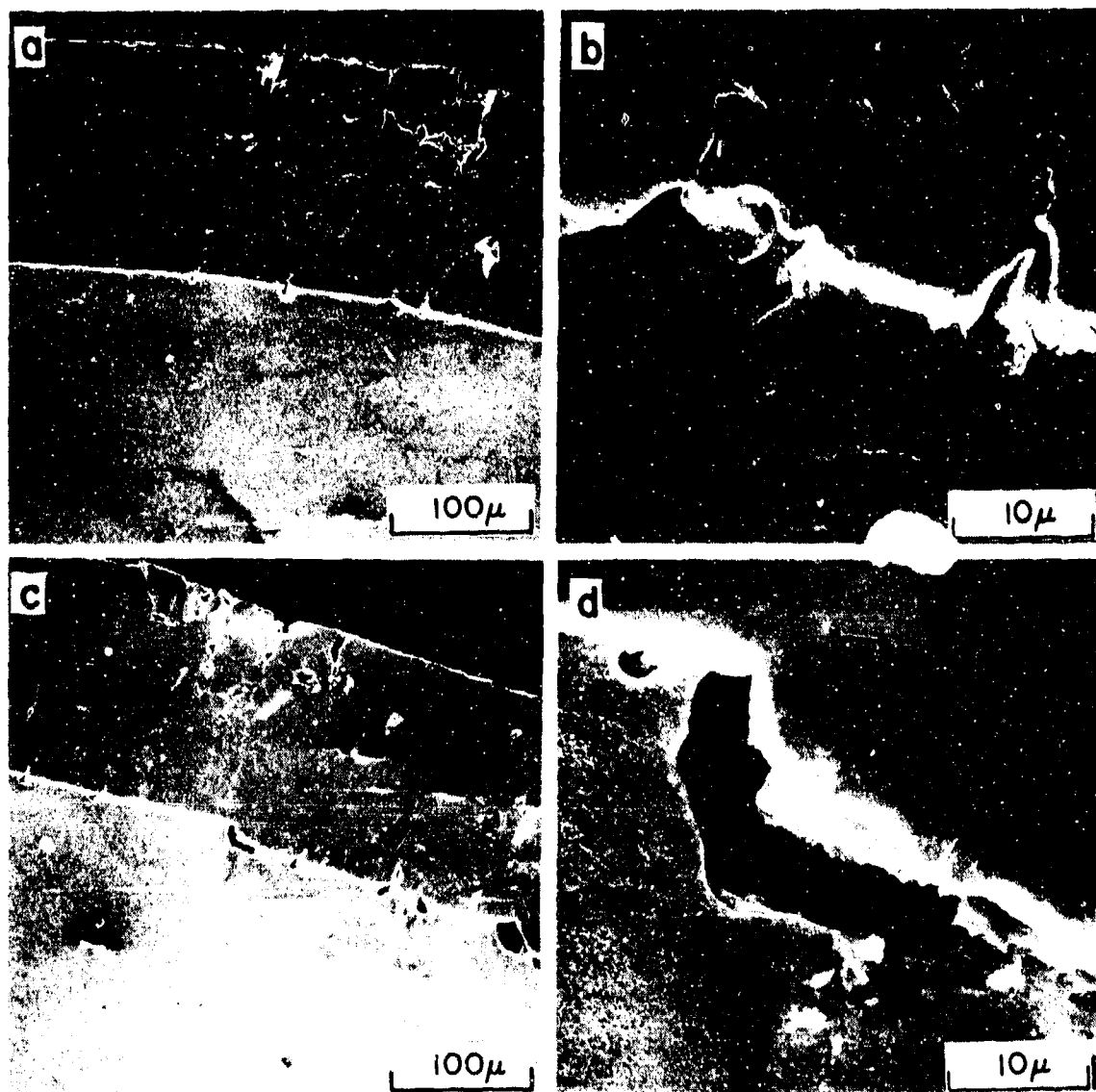


Fig. 39 Scanning electron micrographs of electropolished section of specimen BB. No crack propagation through the interface is observed. Significant undermining is associated with crack blunting. Cr on top.

.54-f

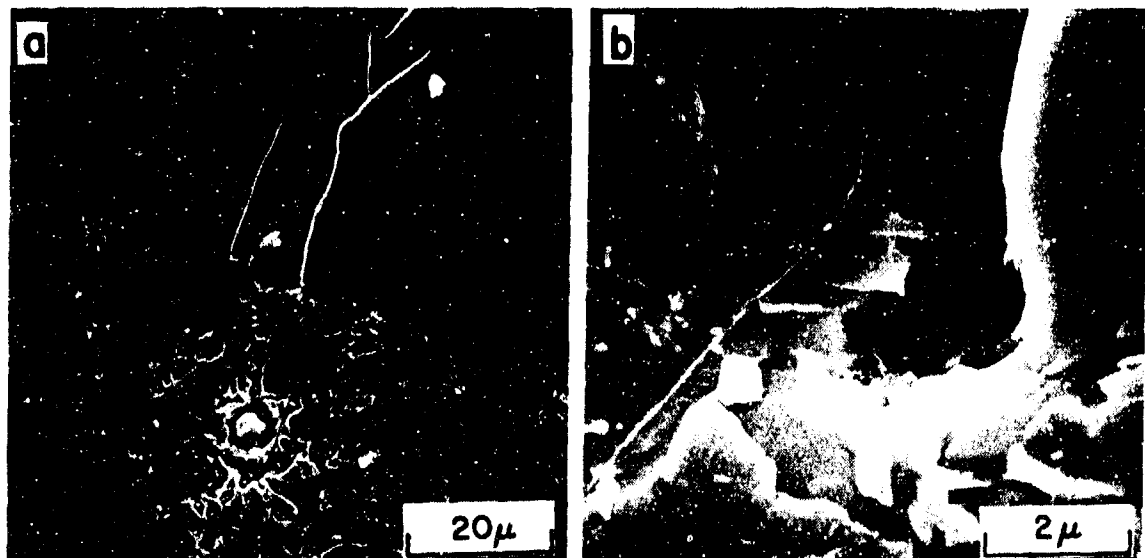


Fig. 40 Scanning electron micrographs of electropolished section of specimen AA. No crack propagation is observed through the interface and also no associated deformation is detectable. Cr on top.

54g

The observed residual surface crack openings seen for specimens AU, BH and AQ are consistent with the interfacial deformation seen for these specimens. Scanning microscope montages of the surface of the Cr plate for specimens AU, BH and AQ are seen in Figs. 41, 42, and 43, respectively. The same larger residual crack openings seen for AU and AQ would suggest the presence of more significant near-interface activity for these specimens than for specimen BH.

To summarize, all test conditions employed, with the exception of free thermal expansion, lead to some form of Cr/steel interface degradation that is expected to play a role in eventual interface debonding. Apparent differences in the effect of the strain and applied thermal cycle have been seen on the details of the deformation. A modified measurement approach would be required, however, to evaluate the relative importance of these degradation modes. In lieu of such measurements, one can speculate that, all else being equal, those conditions which lead to rapid crack propagation into the steel rather than to crack blunting at the Cr/steel interface would cause the least interfacial undermining. These then would be, for our test set, through  $A_1$  - through  $M_s$  at 0.2% strain and below  $A_1$  at .8% strain. The dependence of the chemical alteration at the interface on thermal fatigue state as well as the fracture resistance requirements of the gun tube itself would, of course, have to be included in the overall systems evaluation.

#### 3.4.3.3. General Cr Cracking, Deformation and Specimen Fracture.

Cracking of the inner (inside) surface of the test specimens is the rule. Figure 44 shows an example of this phenomenon. For specimens run through  $A_1$  - above  $M_s$  and through  $A_1$  - through  $M_s$ , the surface simply scales off (as apparent in Fig. 44b and 44c for specimen AU). For the specimens run

below  $A_1$ , however, inside specimen cracking apparently is the prime cause of final specimen failure. For all specimens appreciable large residual crack openings are always seen in the Cr plate near the point of failure. This is apparent both in Fig. 44a and in Fig. 45a, both for specimen AU. In addition to circumferential cracking, significant opening of cracks parallel to the load axis are seen and manifest themselves on the failure surface.

The intrinsic layered structure of the deposited Cr is particularly evident in Fig. 45b. The detailed process of degradation of the Cr plate itself as evidenced by fracture structure and electropolished sections has been found to be a function of the constraint conditions and is noticed particularly in comparison with the Cr in the Cr/Co plated combination. This comparison will be elaborated upon later, but for sake of continuity the typical cracking and fracture structure seen on Cr plated gun steel is described here.

Specimen AA, thermally cycled in free expansion, can be used as a point of comparison (Fig. 46). The cracking pattern seen is essentially intrinsic to the Cr as-plated (i.e., the thermal cycling alone has resulted in little apparent additional damage to the plate). In contrast, Fig. 47 shows an electropolished section of Cr plate on specimen AU and what appears to be zones of deformation associated with the as-plated cracks after thermal fatigue. It is surmised that the boundaries of this deformation may correspond to the lines of blocky fracture of the Cr plate as seen in Fig. 48a and 48b. Neighboring regions of comparatively smooth fracture of the Cr, such as in 48c and 48d, may be associated with the initial cracks in the Cr that propagate into the steel, with the blocky fracture occurring as the stress in the remainder of the contiguous Cr rises. Both specimens BB and AU show similar Cr crack phenomena.

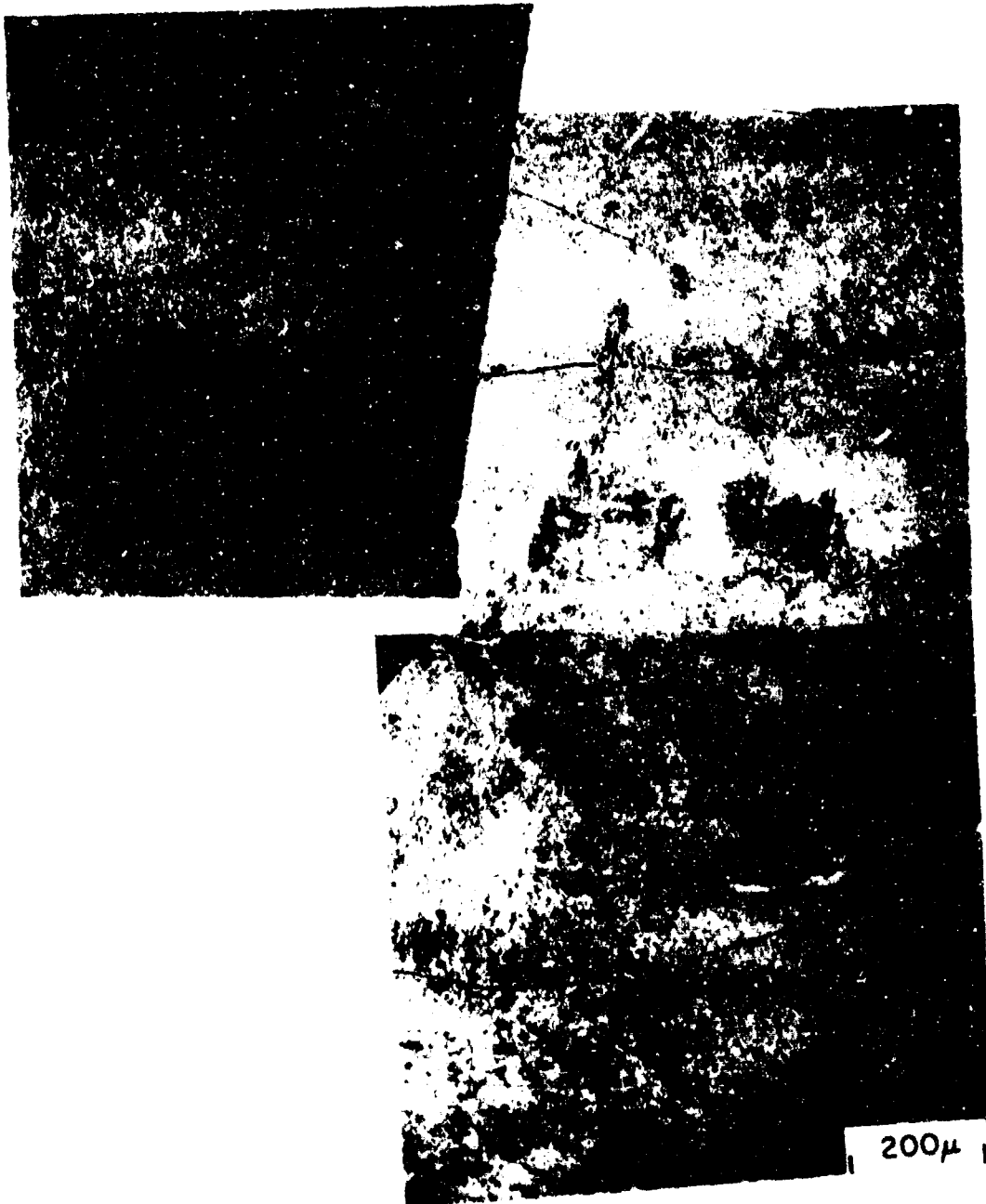


Fig. 41 Montage of scanning electron micrographs of surface of Cr plate for specimen AV. Load axis is vertical.

56-a



Fig. 42 Montage of scanning electron micrographs of surface of Cr plate for specimen BH. Load axis is vertical.

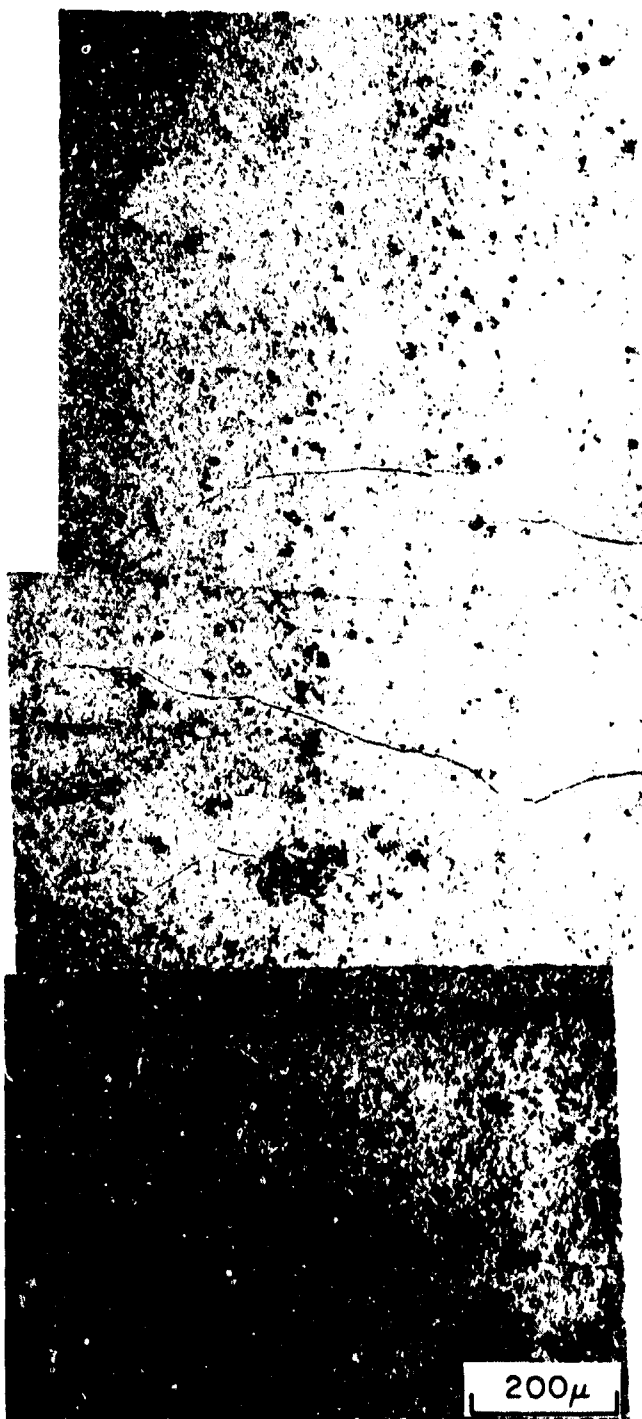


Fig. 43 Montage of scanning electron micrographs of surface of Ur plate for specimen A Load axis is vertical.

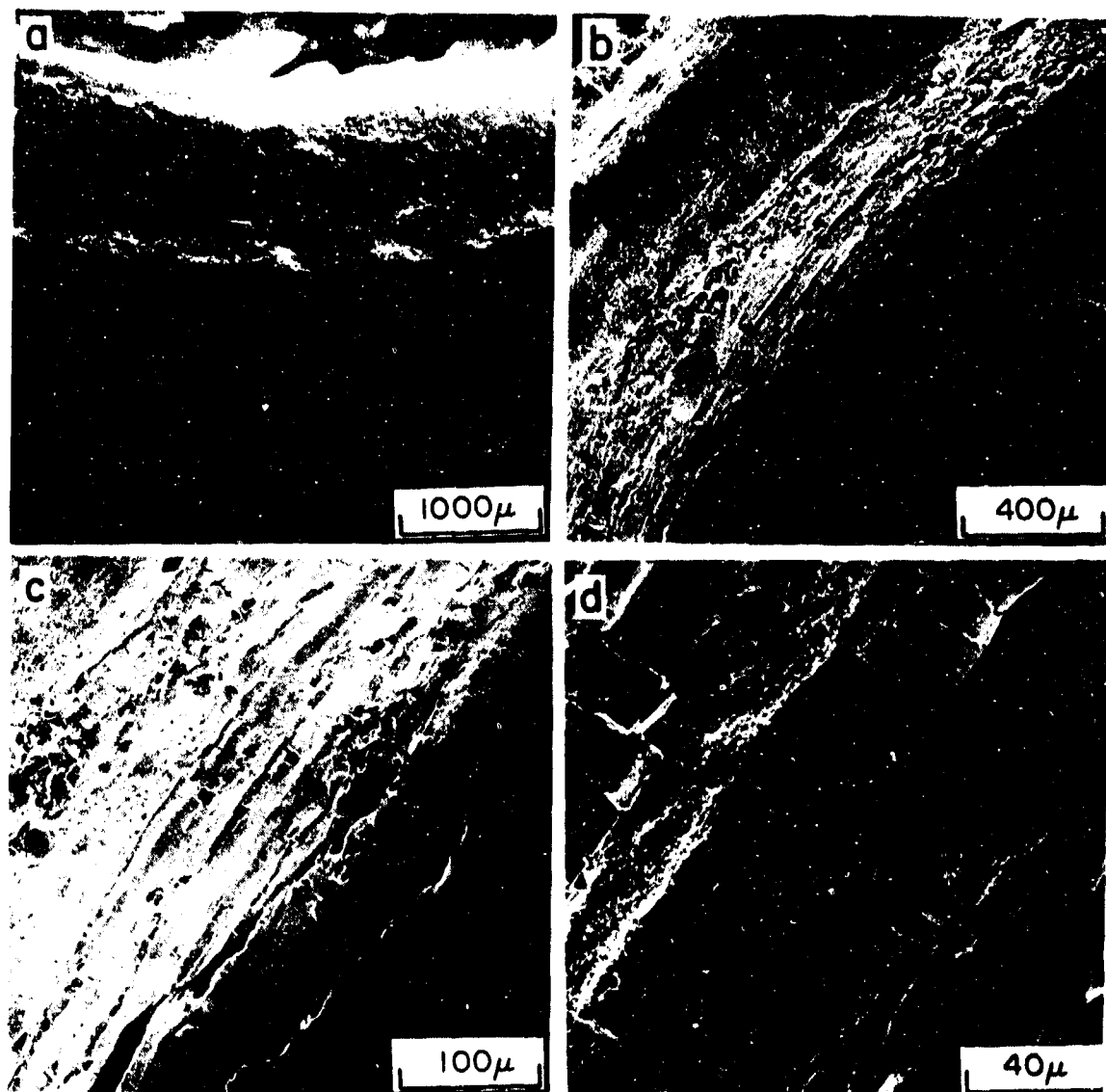


Fig. 44 Scanning electron micrographs of the fracture surface of specimen AU. Cracking of the inside surface is seen in b, c and d.

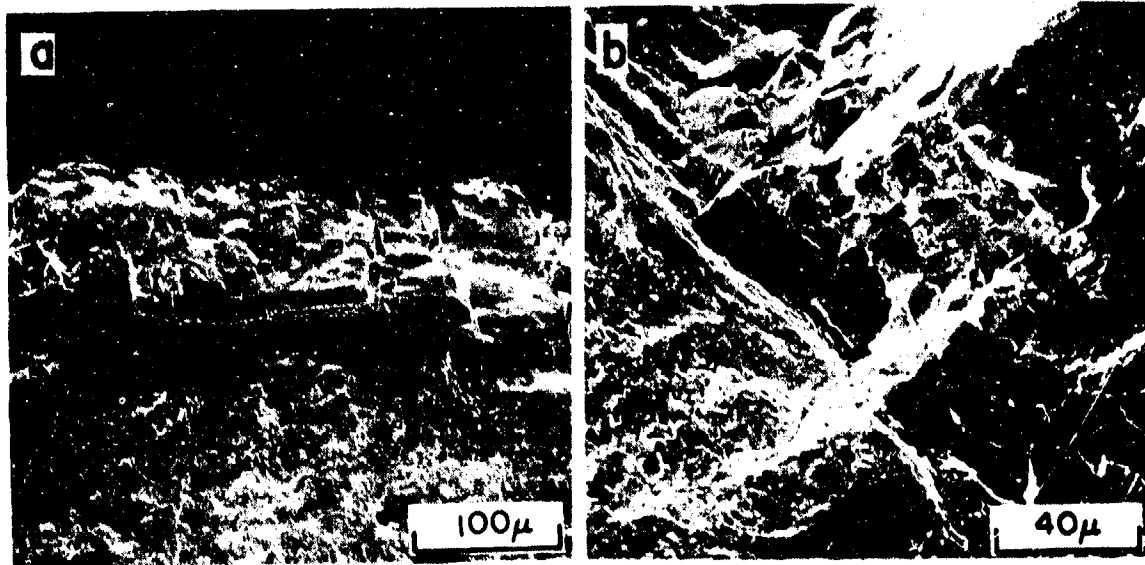


Fig. 45 Scanning electron micrograph of a segment of the fracture surface of specimen AU showing axial cracking in the Cr plate.

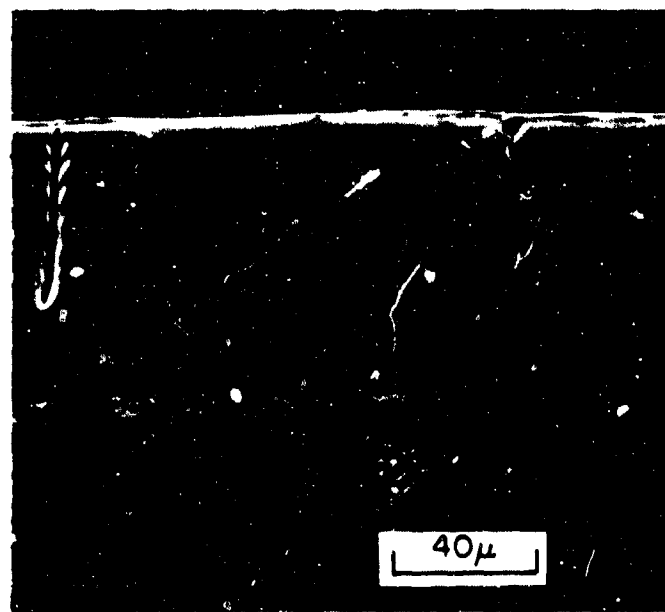
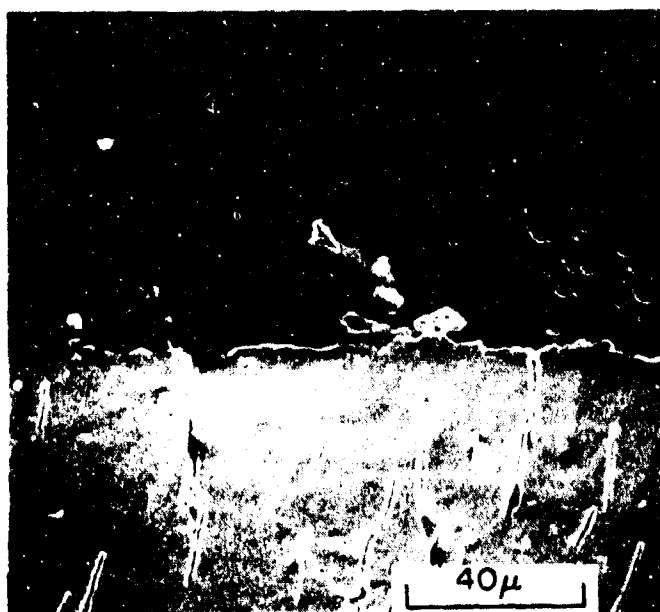
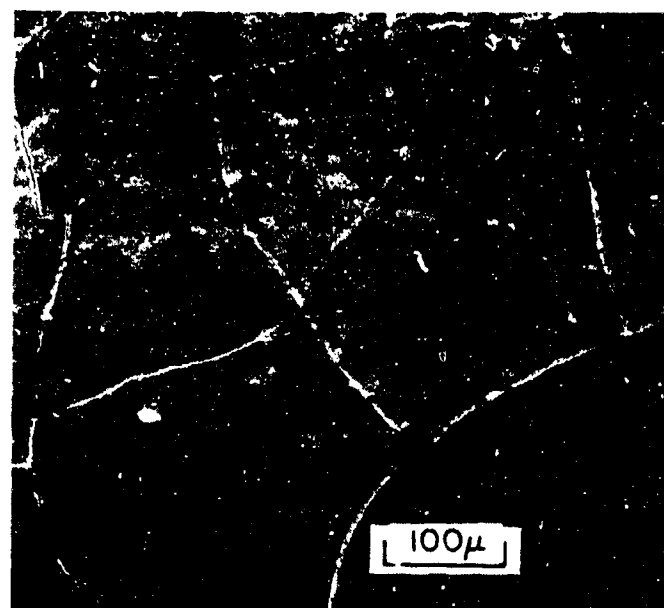


Fig. 46 Scanning electron micrographs of the surface fracture and electro-polished section of specimen AA. Crack pattern is essentially intrinsic to the electrodeposited Cr before thermal cycling.

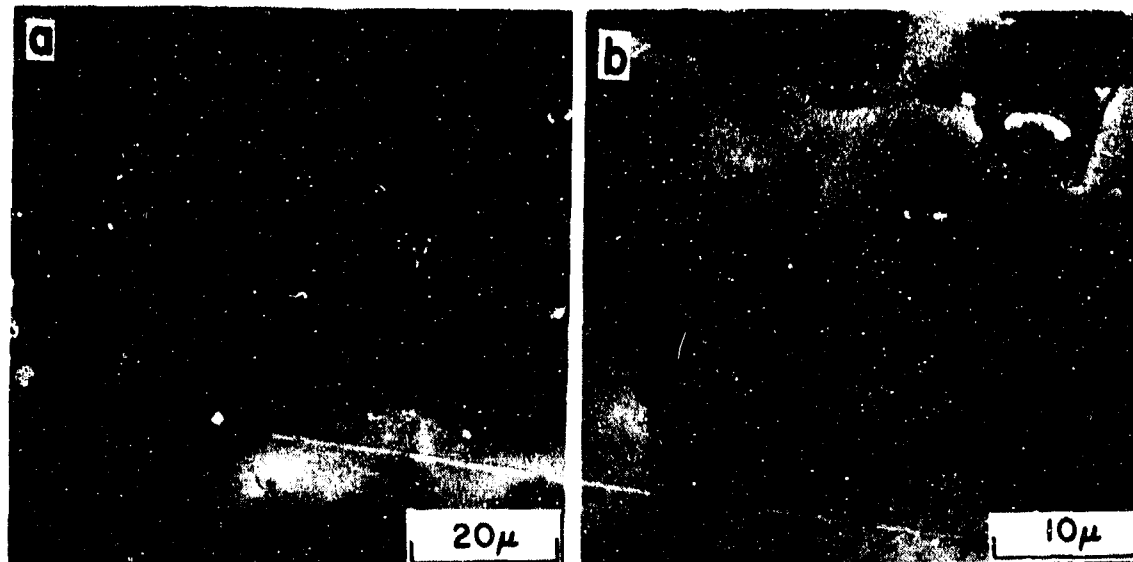


Fig. 47 Scanning electron micrographs of electropolished sections of Cr layer of specimen AU. Apparent zones of deformation are seen associated with the cracks in the Cr.

56-9

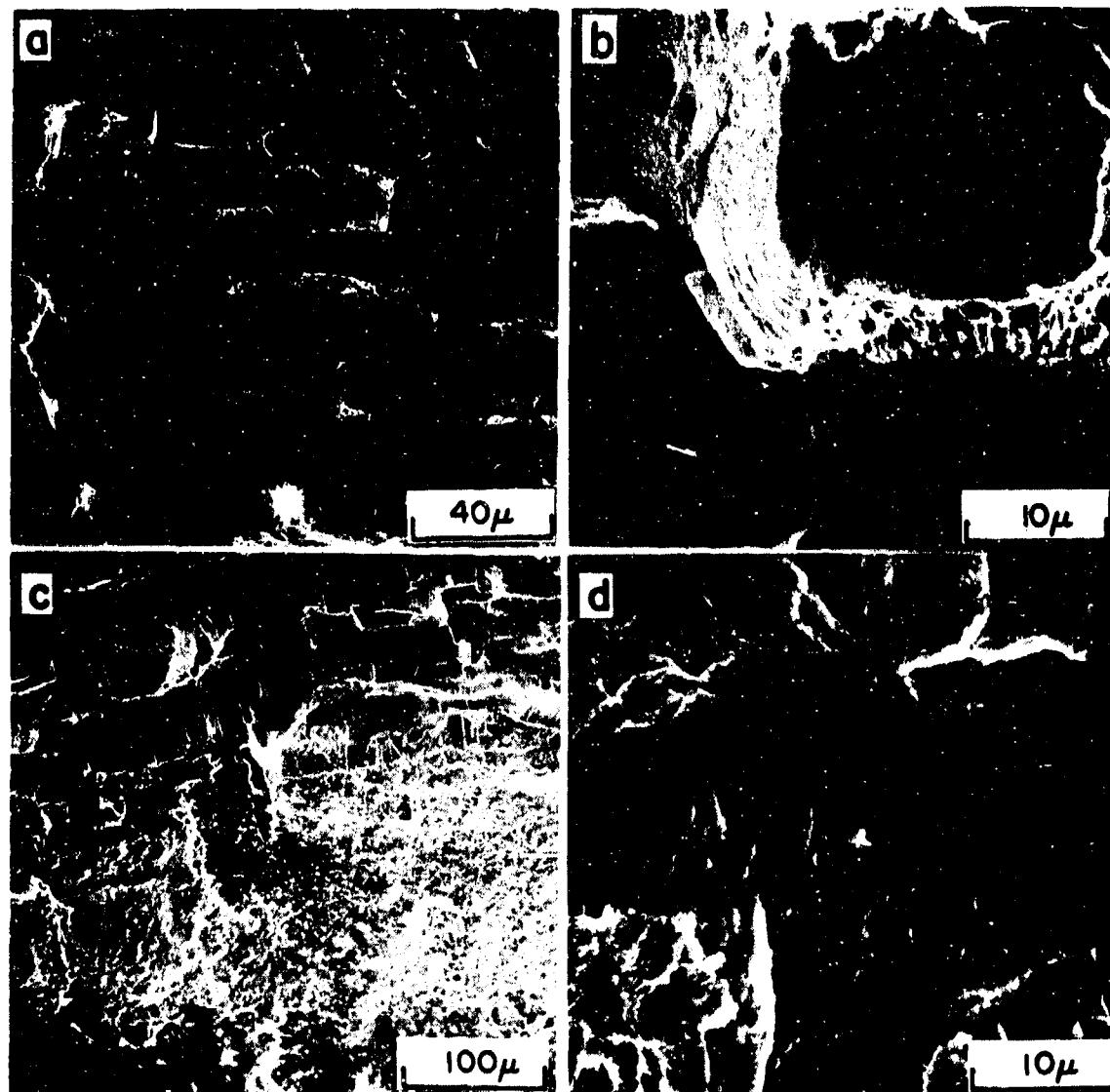


Fig. 48 Scanning electron micrographs of section of fracture surface of specimen BB. a & b show blocky appearing fracture surface possibly associated with deformation zones in the Cr. The smooth cracking in c & d may be associated with an initial through crack in the Cr.

In summary, a distinct deformation and cracking structure is seen for the Cr plate on steel when the combination is subjected to simultaneous thermal and fatigue cycling. The observed cracking structure is attributed to deformation in the Cr and the presumption is that the result of the deformation is to weaken the plate. This will be contrasted to the observations of Cr plate on Cr/Co/steel combinations in the next section.

3.4.4. Composite Cr/Co Plate on Steel Microscopic Results. The composite plate structure tested has been previously described, but to briefly review, the plating system tested consisted of a coating of dispersion hardened Co plated on each steel test specimen with a layer of Cr on top of the Co. The Co layer was typically 6-7 mils thick with the Cr layer being about 1.5 mils thick. Aluminum oxide was used as the dispersion hardening agent and the effect of two dispersion conditions were examined: ultrasonically dispersed  $\text{Al}_2\text{O}_3$ , yielding a fine dispersion; non-ultrasonically dispersed  $\text{Al}_2\text{O}_3$ , yielding localized agglomeration of the  $\text{Al}_2\text{O}_3$ . Figure 49 illustrates the general composite structure, here for specimen BR at a zone of major tearing in the steel. In all of the following figures in this section the Cr layer will be positioned uppermost (although it may not necessarily be in view).

The final test set for the evaluation of the Cr/Co plating system consists of eight specimens as listed in Table VI. The pertinent test parameters for these specimens are listed in Table VII. Specimens BO, BR, and BS are 4340 steel and the Co- $\text{Al}_2\text{O}_3$  combination were plated ultrasonically. These were tested for the three basic test temperature ranges previously described. Specimen AN is a gun steel specimen Co- $\text{Al}_2\text{O}_3$  plated without ultrasonic agitation and fatigued at temperatures below  $A_1$ . Specimen AM was tested to fracture with Freon in the gas cooling stream, so it was heavily contaminated with chlorides. It was not analyzed further. Specimens CF and

BT did not have completely satisfactory electroplates and thus gave anomalous results on testing. The plating flaked off the gage section of specimen CF at 66 cycles, causing the strain measurement to differ wildly from the preset curve. This caused a large fluctuation in load and the gage section was badly distorted. The cause of the bad plating is suspected to be difficulty associated with obtaining the proper suspension of  $Al_2O_3$  in the Co plating bath due to a change in  $Al_2O_3$  powder type. Specimen BT had an uneven Cr plate varying in thickness from one end to the other. This changed the electromagnetic susceptibility of the specimen, causing it to heat unevenly. Neither CF nor BT have been analyzed further. Specimen BN gave a valid test which was stopped after 20 cycles to allow comparison to specimen BR which was tested to failure. In the press of time at the end of the contract period, it was not possible to perform micrographic analysis of specimen BN.

As for the Cr/steel evaluation, the tested specimens were subjected to extensive post thermal fatigue characterization. The same remarks made in that section, with regard to the applicability of the number of cycles to specimen failure, apply to the Cr/Co plate evaluation series. The principal objective of the characterization is to identify potential degradation mechanisms for this three component system, and as much as possible to relate the observations to the test variables and to variances in test specimens. As for the Cr/steel plate, several potential degradation mechanisms have been identified that can be expected to play a major role in the erosion response of Cr/Co.

3.4.4.1. Effect of Thermal Cycling Range. Specimen BS, thermally fatigued through both the  $A_1$  and  $M_s$  temperatures, displayed a markedly different response in terms of deformation at the Cr/Co interface as compared

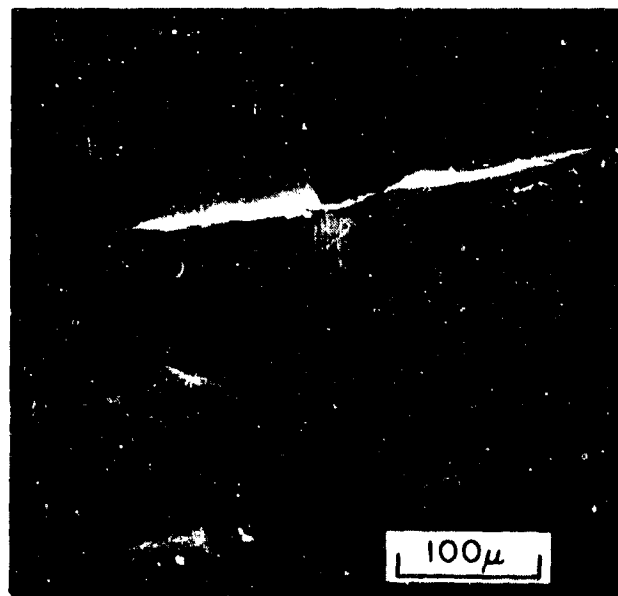
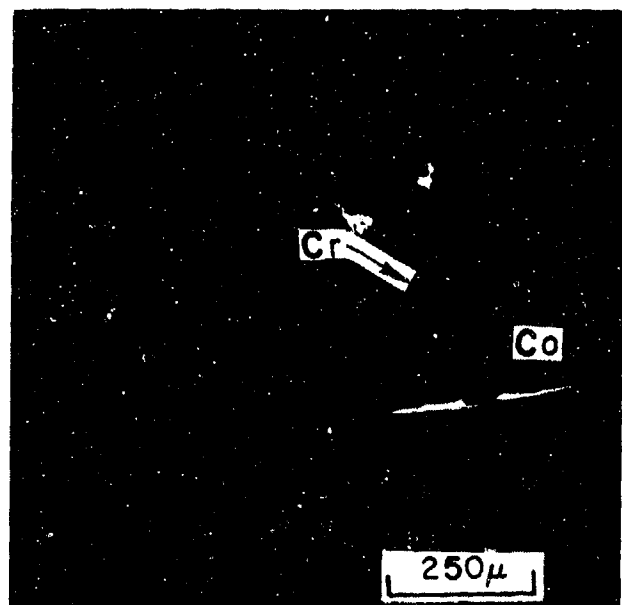


Fig. 49 Scanning electron micrographs of electropolished sections of specimen BR.

to the remaining specimens. As seen in Fig. 50, no propagation of cracks from the Cr into the Co layer took place for this specimen. Instead, the points of Cr crack/Co interface became folded into the Co, effecting what can only be described as a crack blunting. The specimen failed principally due to extreme necking. The process by which the observed in-folding took place, or the local deformation mechanics of the event, are not immediately obvious. One can speculate, but with such limited data it is perhaps better to put this observation down as a point for further study. Clearly, such blunting of the cracks in the Co is desirable if it does not, in turn, lead to Cr/Co interface degradation; in this instance, it appears not to have done so. But, a further evaluation is required to ensure that the result for this test is not the consequence of some unusual test constraint arising from the composite dimensions and applied strain cycle, which might not reasonably represent a deformation form comparable to that experienced in a gun firing cycle. For the remaining three specimens, crack propagation into the Co did occur. The following subsections deal with various aspects of this behavior. Essentially no difference is seen between the results for these specimens except that which can be attributed to variations in  $\text{Al}_2\text{O}_3$  content or distribution.

3.4.4.2. General Crack Propagation into the Co and Deformation at the Cr/Co Interface. Significant variations in the specifics of crack propagation into the Co and the associated deformation at the Cr/Co interface are seen which correlate closely with the distribution and apparent density of  $\text{Al}_2\text{O}_3$ , particulate in the plated Co. In addition to the deliberate variation in  $\text{Al}_2\text{O}_3$  distribution in the Co introduced by selection of ultrasonic plating for specimens BO and BR and of non-ultrasonic plating for specimen AN, some fairly random fluctuations in apparent  $\text{Al}_2\text{O}_3$  density, as detected by scanning electron microscopy, occurred in specimen

BO and BR. This was apparently due to some non-conformity in plating conditions, possibly due to the complicated specimen geometry interacting with standing waves in the ultrasonic deposition apparatus.

The consequence of this was to provide a variety of test conditions on the same specimen, with, in some cases, a low  $\text{Al}_2\text{O}_3$  content region occurring at the Cr/Co and Co/steel interfaces and, in other cases, a high  $\text{Al}_2\text{O}_3$  content region. The most significant interfacial damage in the Co at the Cr/Co interfaces occurs either when the  $\text{Al}_2\text{O}_3$  is not ultrasonically dispersed, or when the  $\text{Al}_2\text{O}_3$  content is low. Figure 51, for specimen AN, is a case in point. A decided zone of plastic deformation is apparent in this electropolished section in the Co at the Cr/Co interface. The large particles in the matrix are actually agglomerations of small  $\text{Al}_2\text{O}_3$  particles, as can be seen at the higher magnifications. Significant void formation is seen in association with these  $\text{Al}_2\text{O}_3$  rich regions, and voids can be seen running ahead of the crack in Fig. 51d. The subject of void formation will be treated further later. Figure 52 gives a second example of sub-Cr deformation in the Co for specimen AN, and likewise, Fig. 53 shows a somewhat subdued, but quite apparent, zone of sub-Cr deformation in an  $\text{Al}_2\text{O}_3$  lean Co/Cr interface region for specimen BO.

In contrast, for the case of a high  $\text{Al}_2\text{O}_3$  interface zone, Fig. 54a and 54b show no significant deformation in the Co but, instead, that the crack had first blunted in the Cr before breaking into the Co zone. Micrographs 54c and 54d illustrate an intermediate case.

Banding in 54a is particularly apparent and is simply due to gradation in the amount of  $\text{Al}_2\text{O}_3$  in the Co layer. As cracks transit these layers they are seen to have undergone significant changes in direction. Figure 55 gives two examples. This process may, in turn, generate a significant

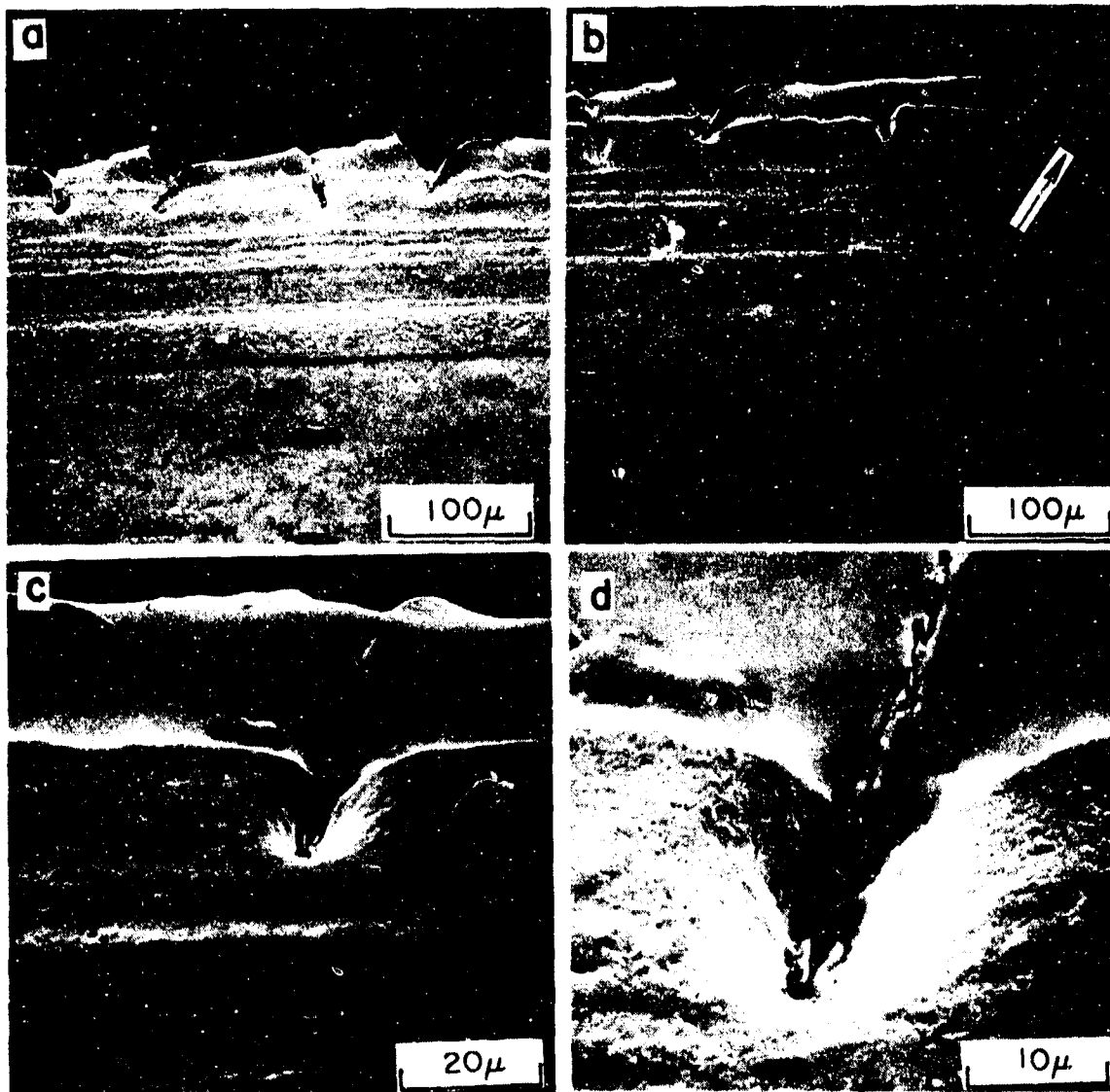


Fig. 50 Scanning electron micrographs of electropolished sections of specimen BS. Cracks in Cr have been folded into the Co, effectively blunting them. Cr layer on top.

60-44

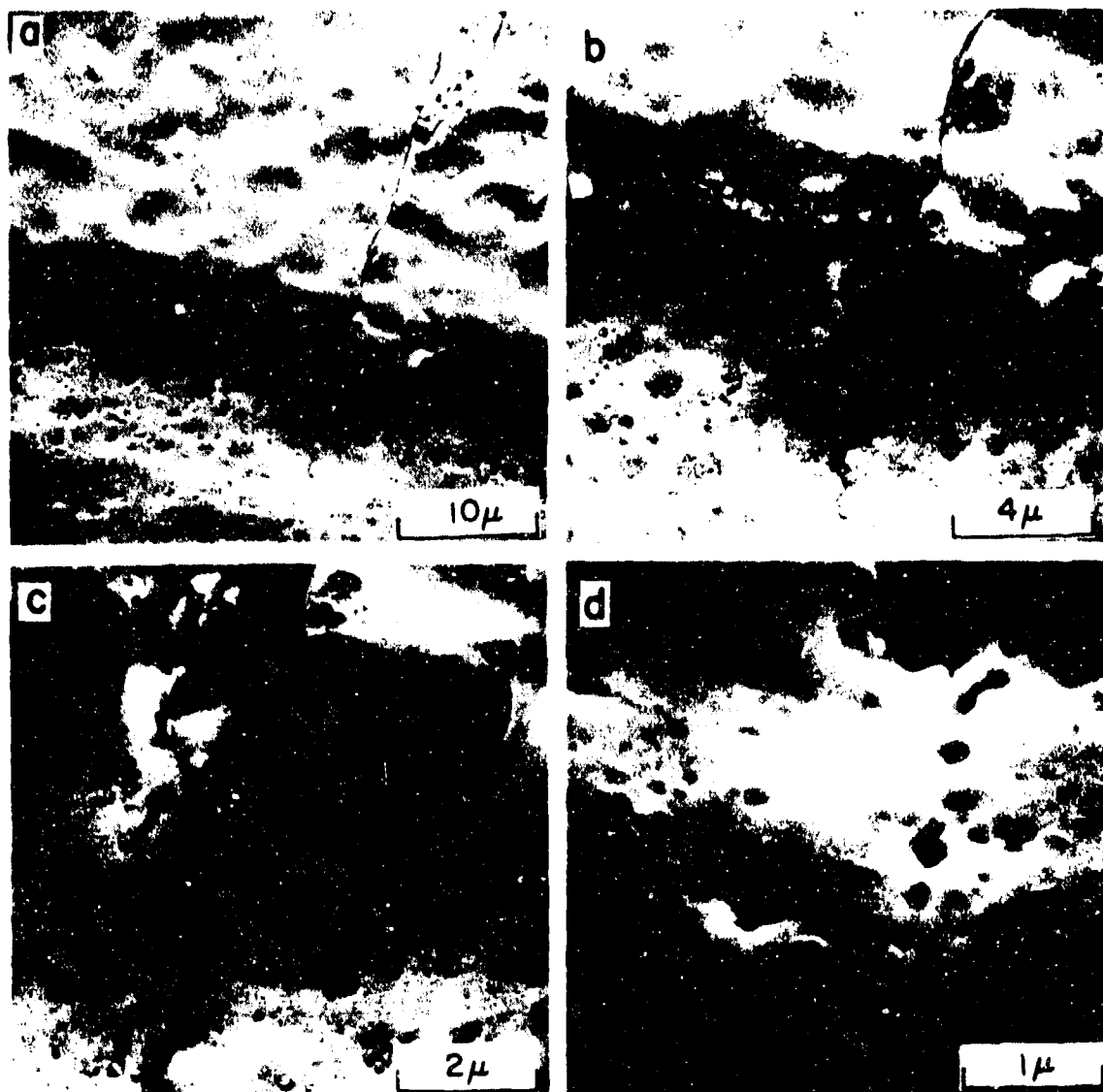


Fig. 51 Scanning electron micrographs of electropolished sections of specimen AN. An extended zone of deformation is seen in the Co at the Cr/Co interface in association with cracking through the interface. Voids have formed both ahead of the crack and in localized aggregates of  $\text{Al}_2\text{O}_3$  particles. Cr uppermost.

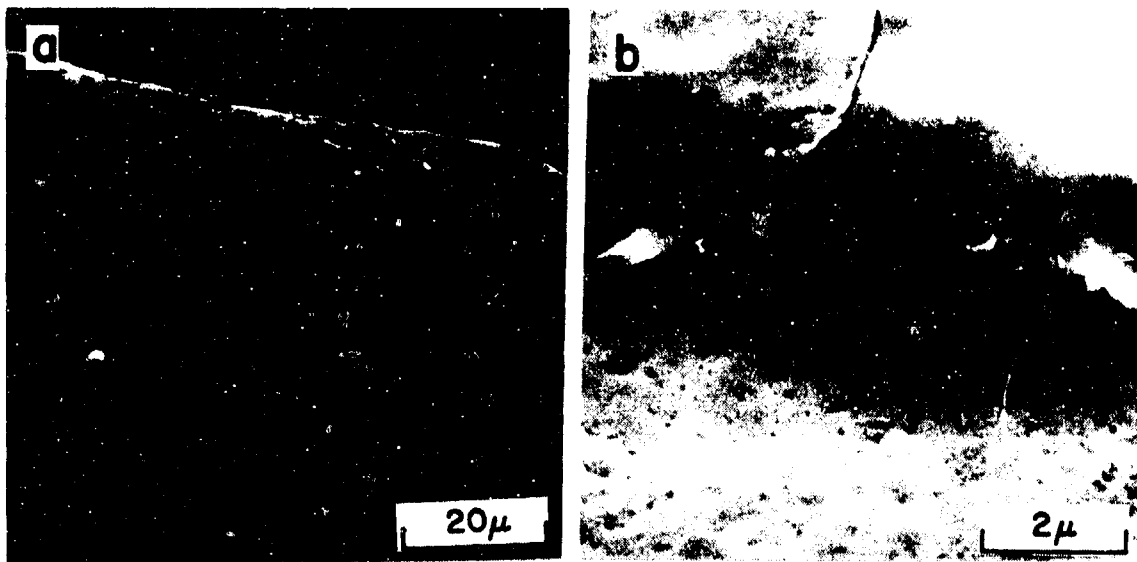


Fig. 52 Scanning electron micrographs of electropolished sections of specimen AN showing deformation in Co at Cr/Co interface and apparent interface debonding. Cr layer at top.

60-c

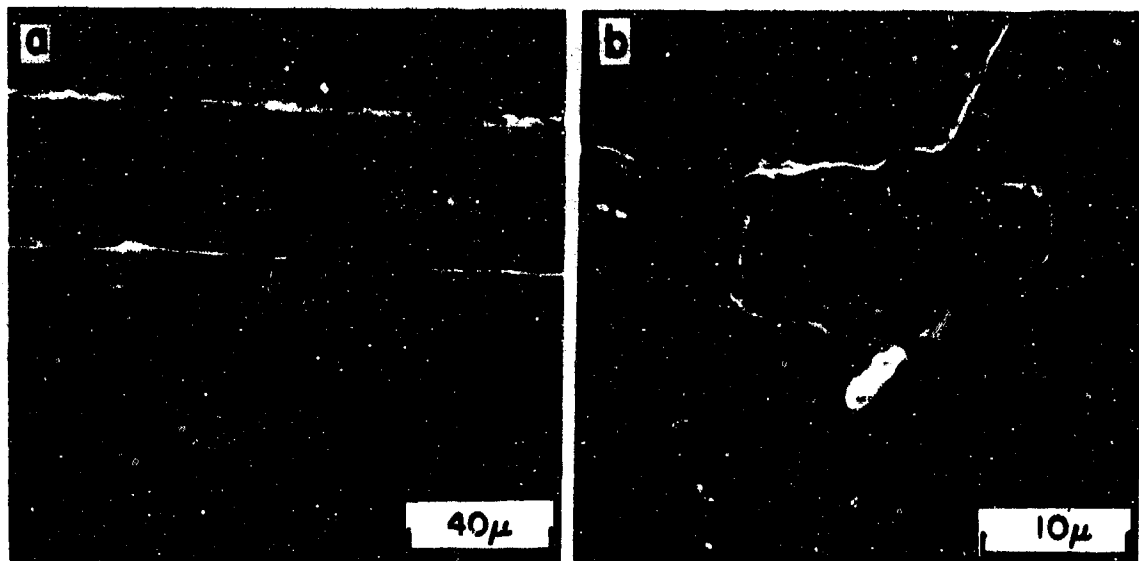


Fig. 53 Scanning electron micrographs of electropolished sections of specimen B0 for a region with low  $\text{Al}_2\text{O}_3$  content in the Co at the Cr/Co interface. Deformation is seen in the Co/Cr layer at top.

60-d

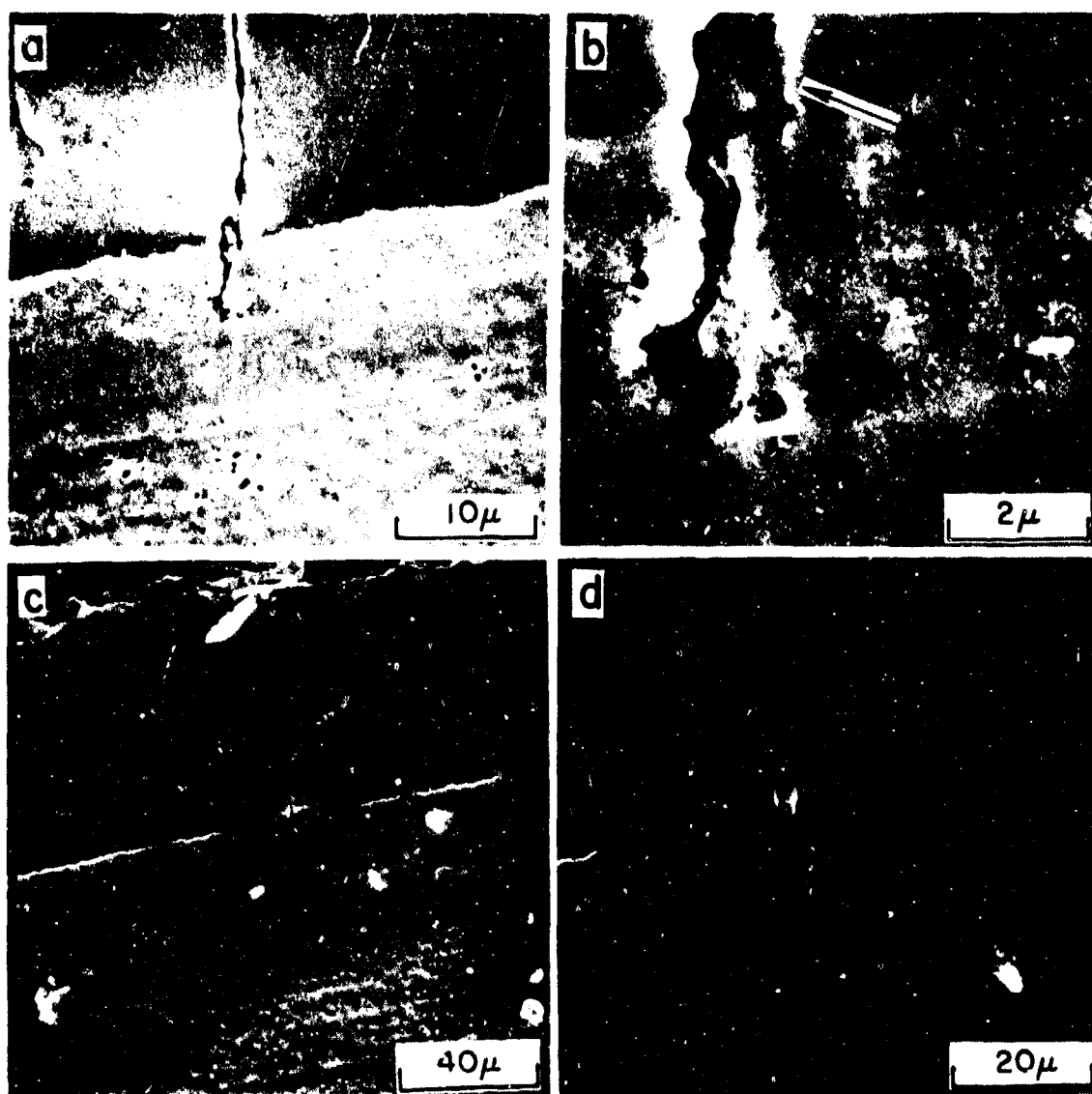


Fig. 54 Scanning electron micrographs of electropolished section of specimen BR: a) and b) at a point of high  $\text{Al}_2\text{O}_3$  concentration in the Co at the Cr/Co interface. No deformation is seen in the Co. Arrow in (b) at probable site of initial crack blunting in the Cr; c) and d) intermediate  $\text{Al}_2\text{O}_3$  concentration showing reduced deformation. Cr layer on top.

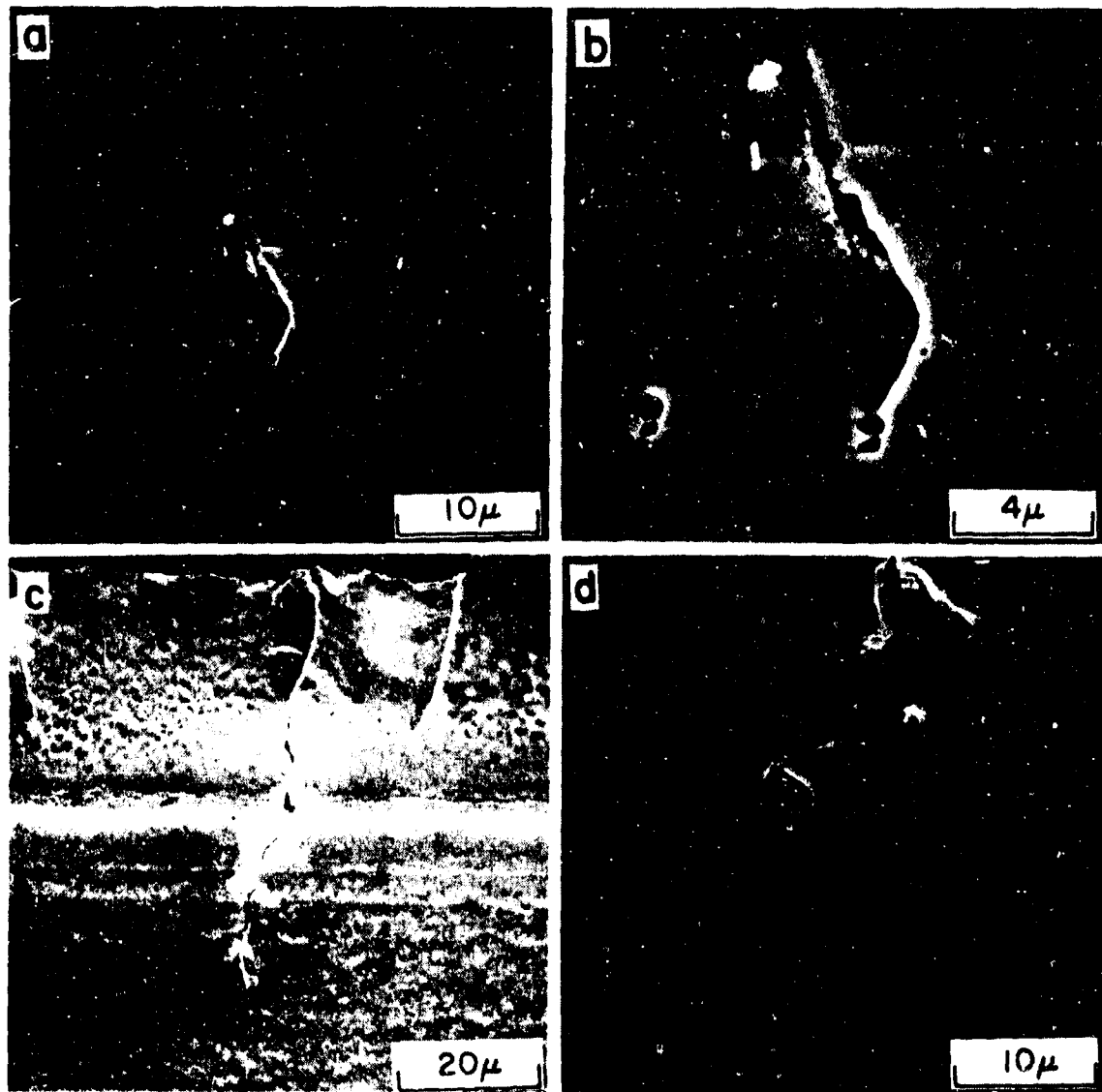


Fig. 55 Scanning electron micrographs of electropolished section of specimen BR illustrating a relationship between changes in  $\text{Al}_2\text{O}_3$  density, seen by banding and changes in crack propagation direction. Cr layer at top.

60-f

resistance to crack propagation through the Co layer, as compared to crack propagation through a more uniform layer. However, such non-uniformity probably is a significant factor in Co delamination (discussed next), and so, on overall balance it is probably better eliminated.

To briefly summarize the above observations, the most severe Cr/Co interface damage results either if the  $\text{Al}_2\text{O}_3$  content in the Co at the interface is low, or if it is not uniformly distributed. When the  $\text{Al}_2\text{O}_3$  content is high, the crack simply passes straight into the Co with perhaps a minimum of preblunting in the Cr layer. If the Co layer is laced with bands of different  $\text{Al}_2\text{O}_3$  content, the crack propagation direction is altered by these gradients.

3.4.4.3. Cobalt Delamination. A major potential degradation mechanism observed for the Cr/Co composite is delamination of the Co layer. Figure 56, an electropolished section of specimen BR, shows what is apparently an incipient plane of delamination in the Co in association with a vertical crack system that has penetrated into the Co layer. In this particular case, the delamination appears to be coupled with a region of sharp gradation in  $\text{Al}_2\text{O}_3$  content. Figure 57, a section of the fracture surface of specimen BS, illustrates a case in which delamination has gone to completion in one region. In 57a, the arrow indicates a delamination crack in the Co fracture surface. At roughly  $180^\circ$  around on the other side of the specimen (Fig. 57b, c, and d), actual delamination has occurred. In 57b the arrow indicates the lower face of the delamination layer. A closeup, in 57d, of the fracture surface of the upper lamination seems to show the presence of a band of somewhat different Co structure through which, or below which, the delamination crack passed. Insufficient test data are at hand to completely characterize the delamination process and the controlling cobalt structural parameters.

#### 3.4.4.4. Void Formation in the Co Layer and Coupling to Crack

Propagation. Voids can form in the as-deposited Co layer, probably due to poor  $Al_2O_3$  to Co bonding. It is reasonable to ask, then, when one sees voids leading a crack tip in a thermally fatigued specimen, which came first? Are cracks following as deposited voids or do the stress fields associated with propagating cracks break up loose  $Al_2O_3$  conglomerations (seen then as voids in section) ahead of the crack, resulting in decreased resistance to crack propagation? There is no clear-cut way to get an answer without use of some form of stop motion experiment. However, micrographs, such as in Figs. 58 and 59, are *prima facia* evidence that the cracks come first, at least in many cases. It is noted that no cracks initiate in the Co at the Cr/Co interface. It is also noted that most cracks in the Cr do enter the Co and always have a short precursor void chain; so, for instance, no cracks are seen to have outrun an as deposited void chain. In fact, one is hard put to imagine a deposition source for a vertical void chain.

It is interesting to note in comparing Fig. 58 with Fig. 59, that the precrack voids are much larger in specimen AN (Fig. 59) which has the nonuniform  $Al_2O_3$  distribution. Another interesting observation is that the crack seen in Fig. 59 probably first initiated at an impurity inclusion in the Cr plate. Figure 60 shows the particle and an energy dispersive x-ray analysis of the particle composition. The main solid bar peaks are from the matrix (i.e., are Cr peaks), and the dotted spectrum is from the near region of the inclusion, showing a main peak of silicon.

On occasion, rather large void systems are seen in association with cracks in the Co. Figure 61 is an example. It is quite possible that some of these voids were plated in, but it should also be noted that they cou'd also be the consequence of a cracking array in three dimensions

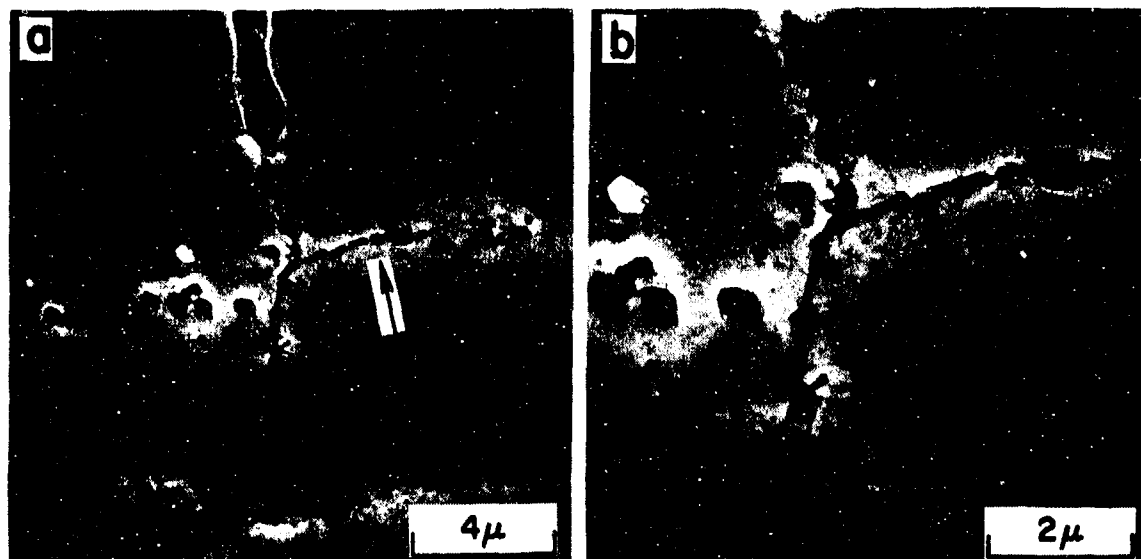


Fig. 56 Scanning electron micrographs of electropolished section of specimen BR. Arrow in (a) at plane of incipient Co debonding. Cr layer on top.

62-a

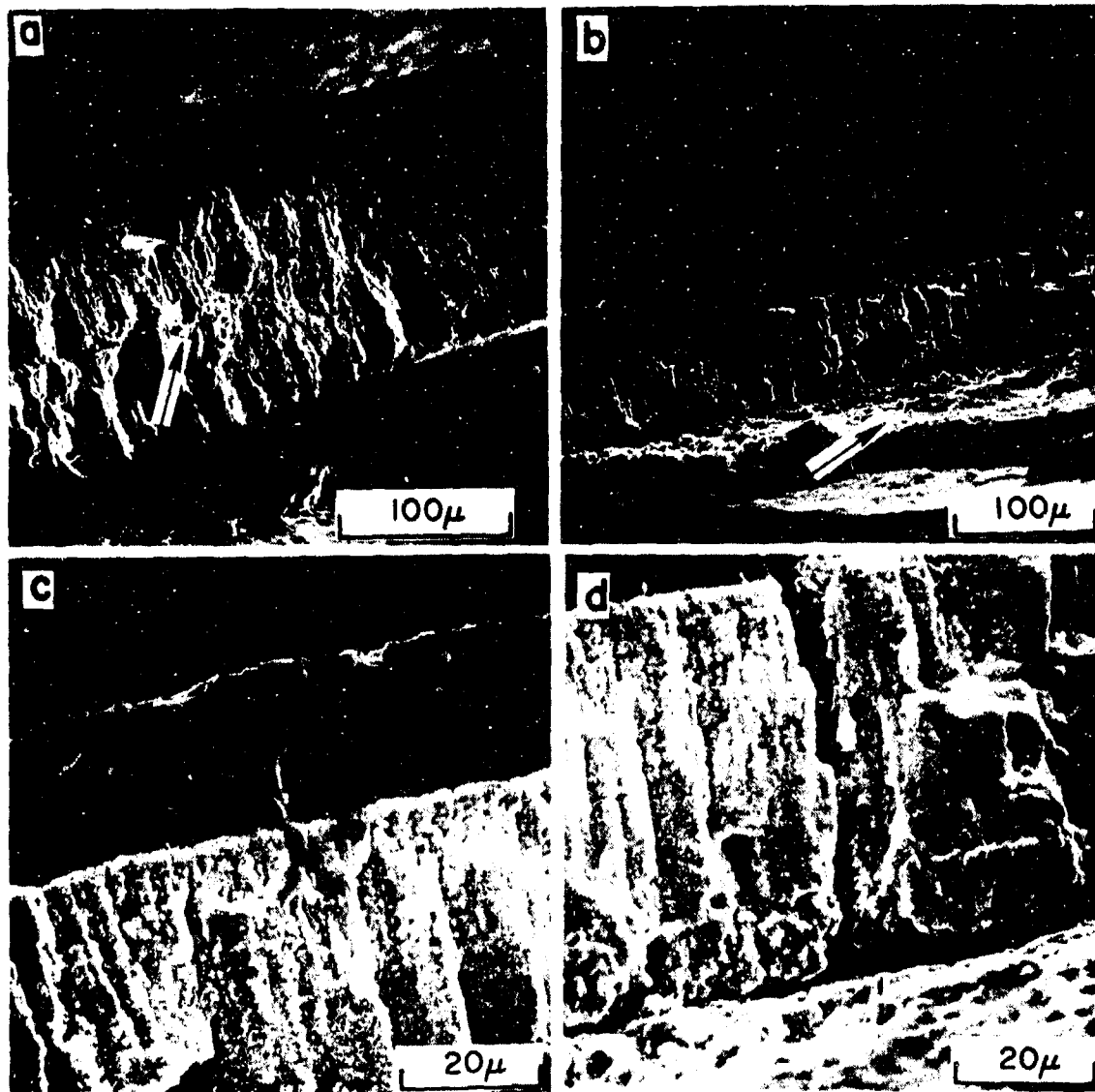


Fig. 57 Scanning electron micrographs of sections of fracture surface of specimen BS. Arrow at delamination crack in the Co in (a). Site b, c and d 180° opposite site (a) and complete Co delamination has occurred there. Arrow in (b) at plane of lower lamination.

62-8

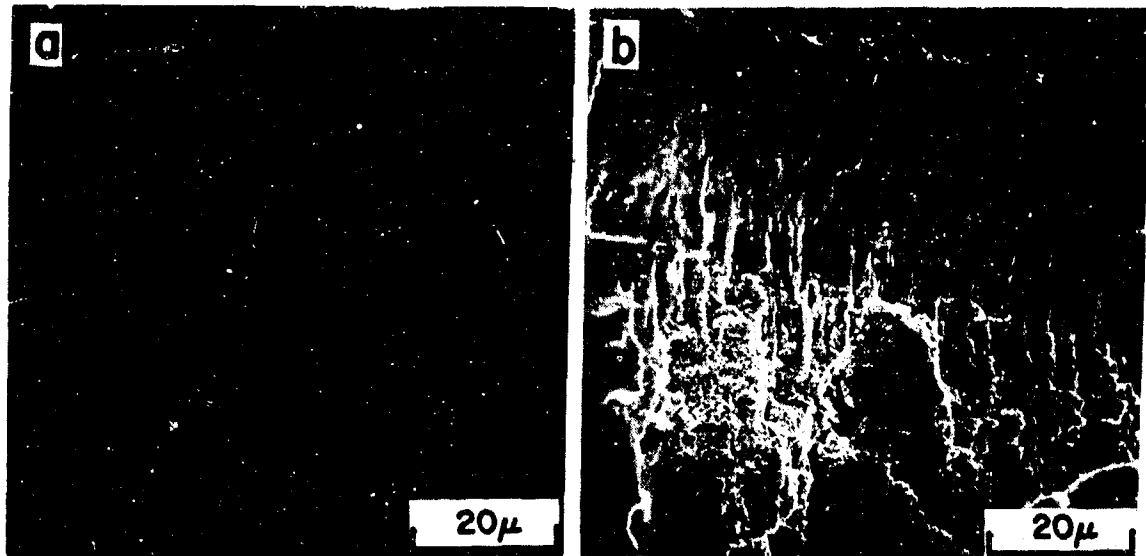


Fig. 58 Scanning electron micrographs of electropolished section of specimen BR illustrating void formation in the Co (a) and Cr/Co fracture surface in (b).

62-c

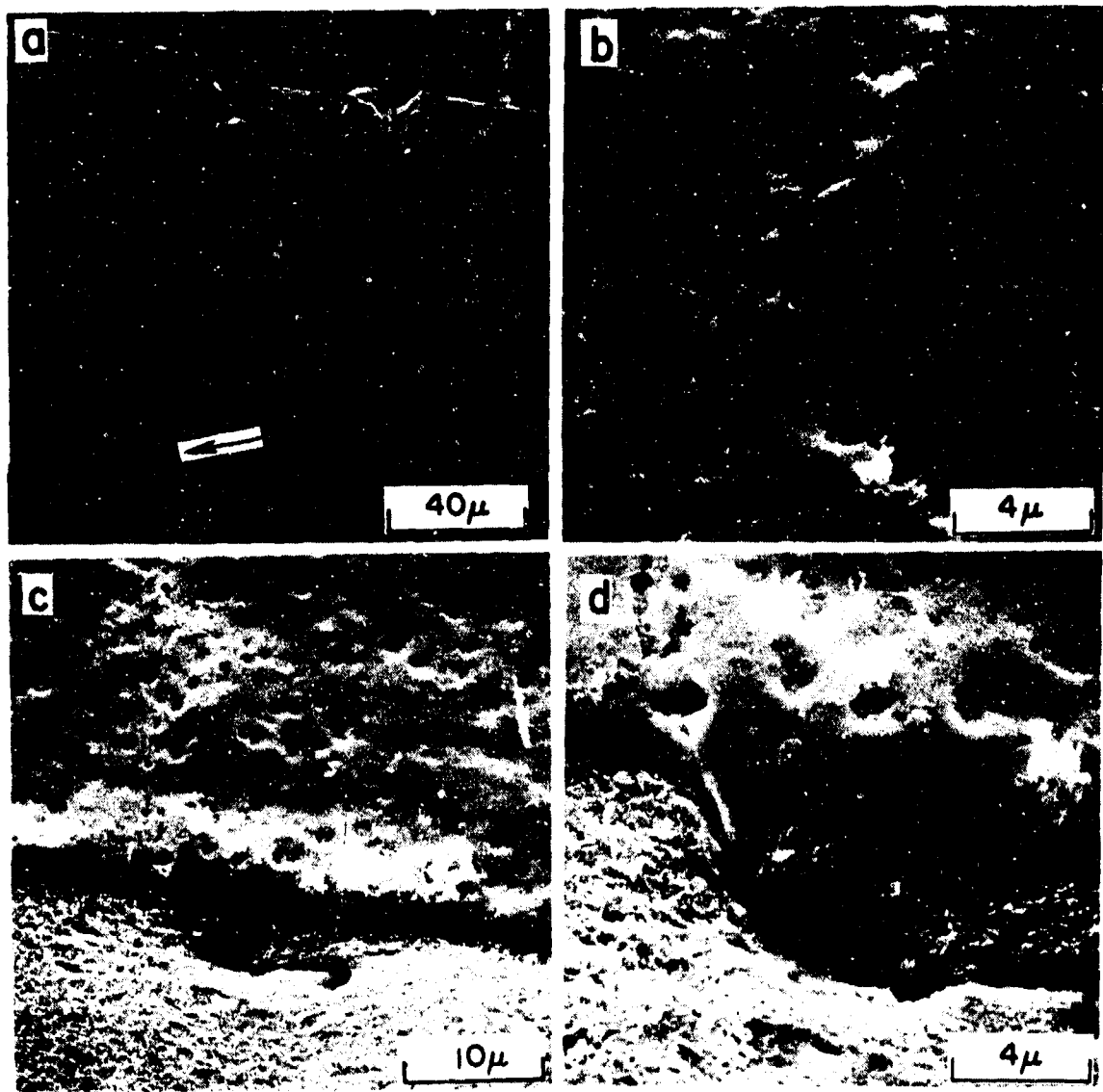


Fig. 59 Scanning electron micrographs of electropolished section of specimen AN illustrating void formation in the nonultrasonically deposited dispersion hardened Co. Voids are particularly associated with  $\text{Al}_2\text{O}_3$  aggregations.

62-d

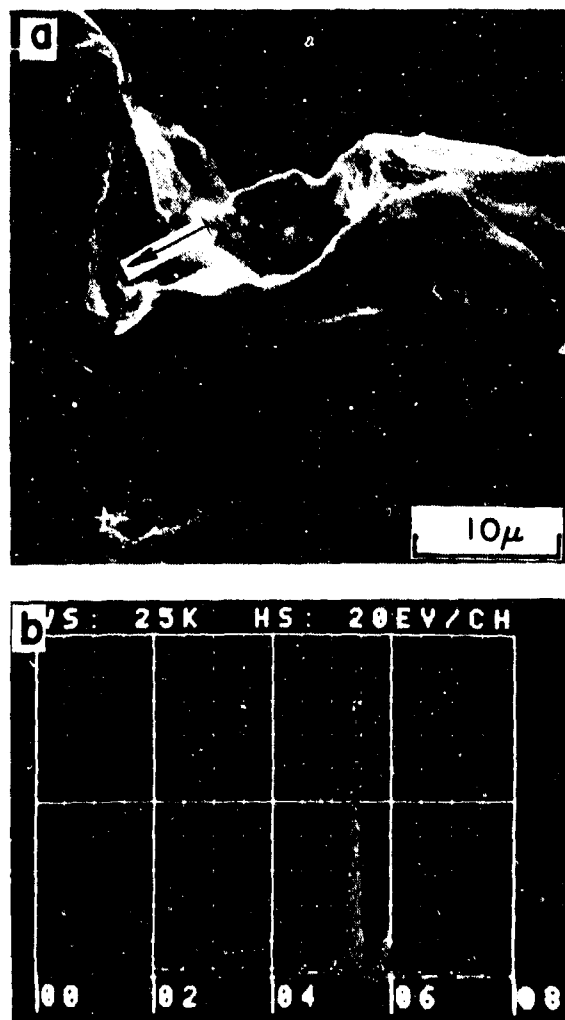


Fig. 60 Scanning electron micrographs of inclusion in Cr at initiation site of crack in Fig. 60 (a), x-ray analysis indicating the inclusion to be primarily silicon (b). The bar spectrum is the matrix, i.e., Cr and the dot spectrum is that in the region of the particle

62-21

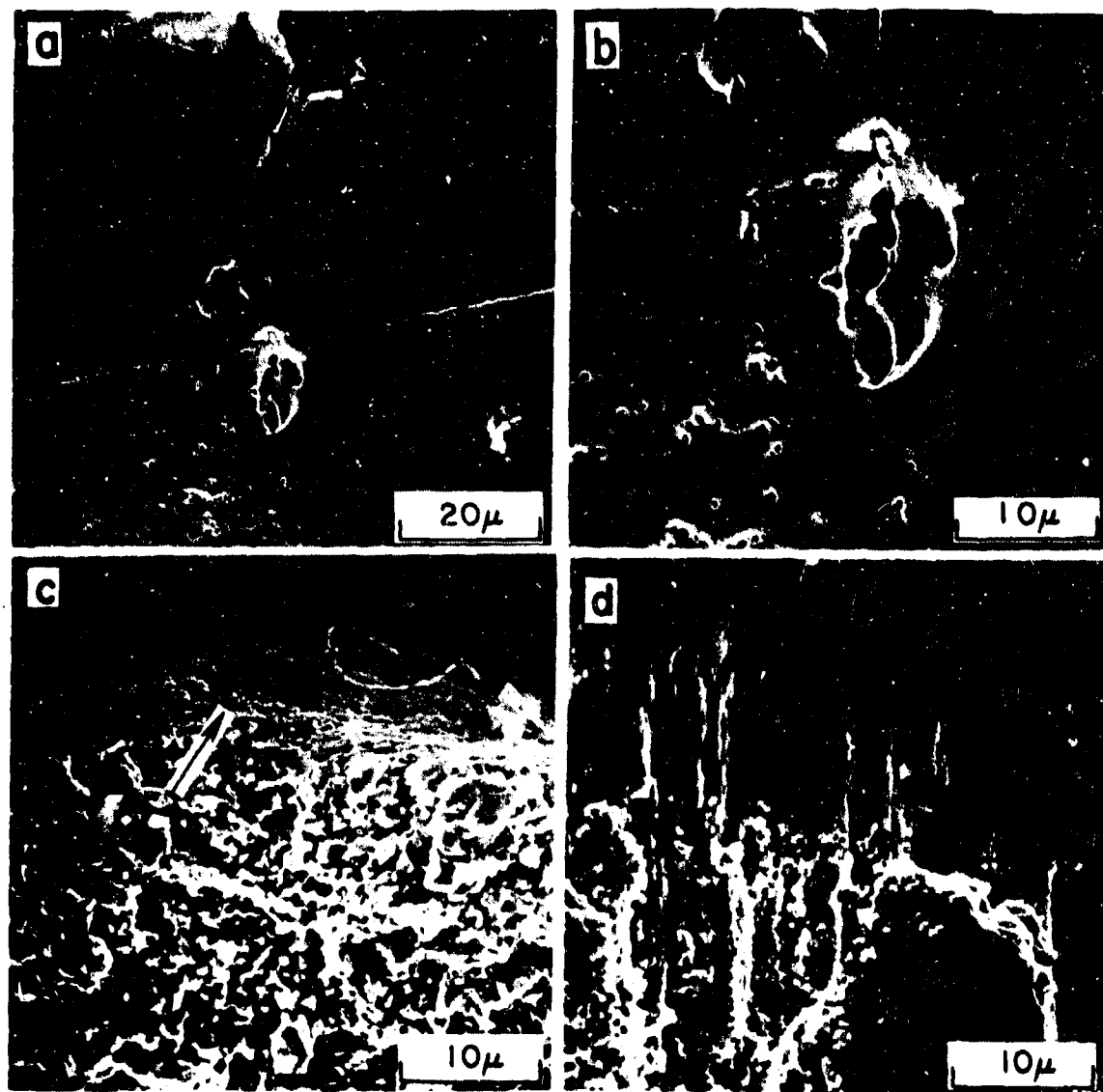


Fig. 61 Scanning electron micrographs of specimen BR: a) and b) electro-polished section; c) Co fracture and Co/steel delamination interface at arrow; d) Cr/Co fracture surface Cr on top illustrates void formation.

62-f

not seen in this section. By way of comparison, Micrographs 61c and 61d show the fracture surface of the Co layer which is rich in voids and belies the structure of this dispersion hardened composite.

3.4.4.5. The Co/steel Interface. No cracks initiate at the Co/steel interface, and furthermore, there is a complete absence of any apparent chemistry or differential thermal expansion related degradation of either material at the interface. Figure 62 is a case in point. Cracks that completely traverse the Co layer first blunt in the steel (Fig. 63). The subsequent failure of the steel substrate is by massive tearing rather than by cracking. Figure 64 shows such a tear. The particle at the arrow in 64a is a silicon particle as identified by x-ray analysis, and may have initiated, or at least have participated, in the development of this particular failure zone. The source of the particle is probably the sand blast honing of the steel given prior to Co plating. The deformation zone in the steel associated with the tear is magnified in Fig. 65, and delamination of the steel from the Co can be seen in association with the tear. This event is quite representative. No chemical alterations have been found in the Co at the Co/steel interface. Figures 66 and 67 are transmission electron micrographs of the Co made within 10  $\mu\text{m}$  of the interface of specimen BR. The  $\text{Al}_2\text{O}_3$  particles have been illuminated in the dark field micrograph, Fig. 67. The apparent structure differs little from that seen for an unfatigued disk specimen with the exception that the  $\text{Al}_2\text{O}_3$  content is higher. An electron diffraction pattern of the Co at the interface is shown in Fig. 68a.

#### 3.4.4.6. Cr Plate Quality and Deformation Structure.

Transmission electron microscopic analysis of the Cr layer from the Cr/Co interface to the Cr surface for specimen BR, shows the Cr to be uniform body

centered cubic chromium having a columnar structure. Figures 69 and 70 are representative micrographs and Fig. 68b is a typical electron diffraction pattern of the Cr layer. No Cr/Co interfacial chemical alteration has been detected. There appears to be significantly less deformation and associated degradation in the Cr over the Co than in the Cr over the steel for the same thermal fatigue environment. This is seen both in a comparison of fracture surface structures and in comparison of deformation highlighted in electro-polished sections. Compare the Cr fracture surface in Fig. 61d to that for Cr on steel in Fig. 48 - both are representative. Compare the electropolished section in Fig. 54c to that for Cr on steel in Fig. 47. Again, both are representative. Of course one essential difference is that the Cr layer over the Co is thinner than that utilized in steel. This makes precise comparison difficult. But, as seen in Fig. 54c, the Cr on Co is thick enough so that two cracking layers have formed in Cr. The absence of blocky fracture of the Cr, as seen for the Cr/steel case, could then indicate the presence of less deformation in the Cr on Co. This is another point which requires further study.

3.4.5. Tantalum - 10 Tungsten Thermal Fatigue Tests. Thermal fatigue tests were performed on two specimens of tantalum-10 tungsten. The fabrication and testing requirements for this material was found to be much different from that for the steels. The alloy is fairly difficult to machine, though it is not extremely strong and is considerably softer than heat treated gun steel. Because it is non-magnetic, it is more difficult to heat by induction. Specimens were successfully fabricated and tested late in the contract period. One specimen, CH, was used to check-out and calibrate the thermal fatigue apparatus as modified for testing this alloy. Two specimens, CI and CJ, were

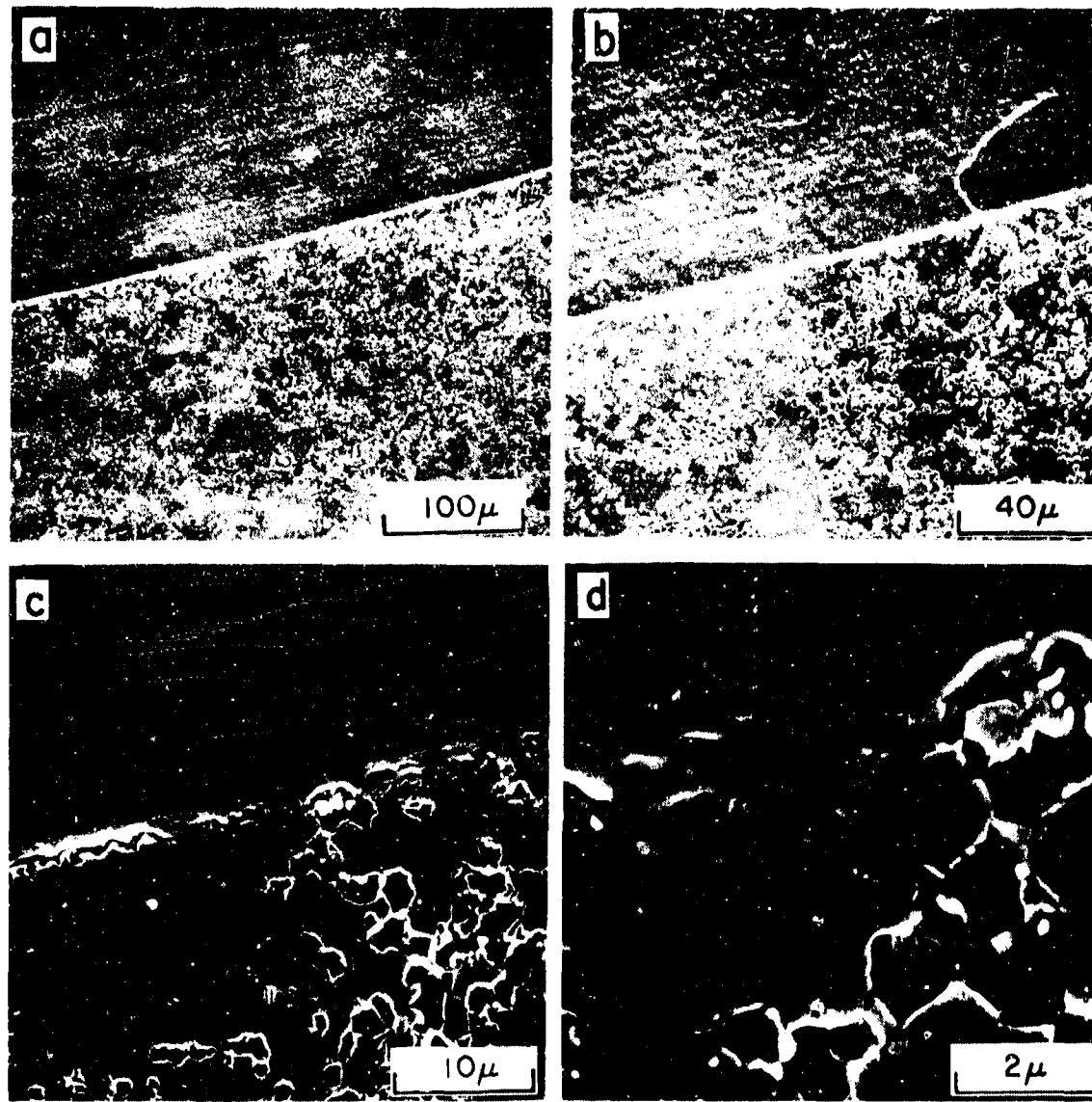


Fig. 62 Scanning electron micrographs of electropolished section of specimen BR at Co/steel interface. No interface degradation is noted. Co on top.

64-a

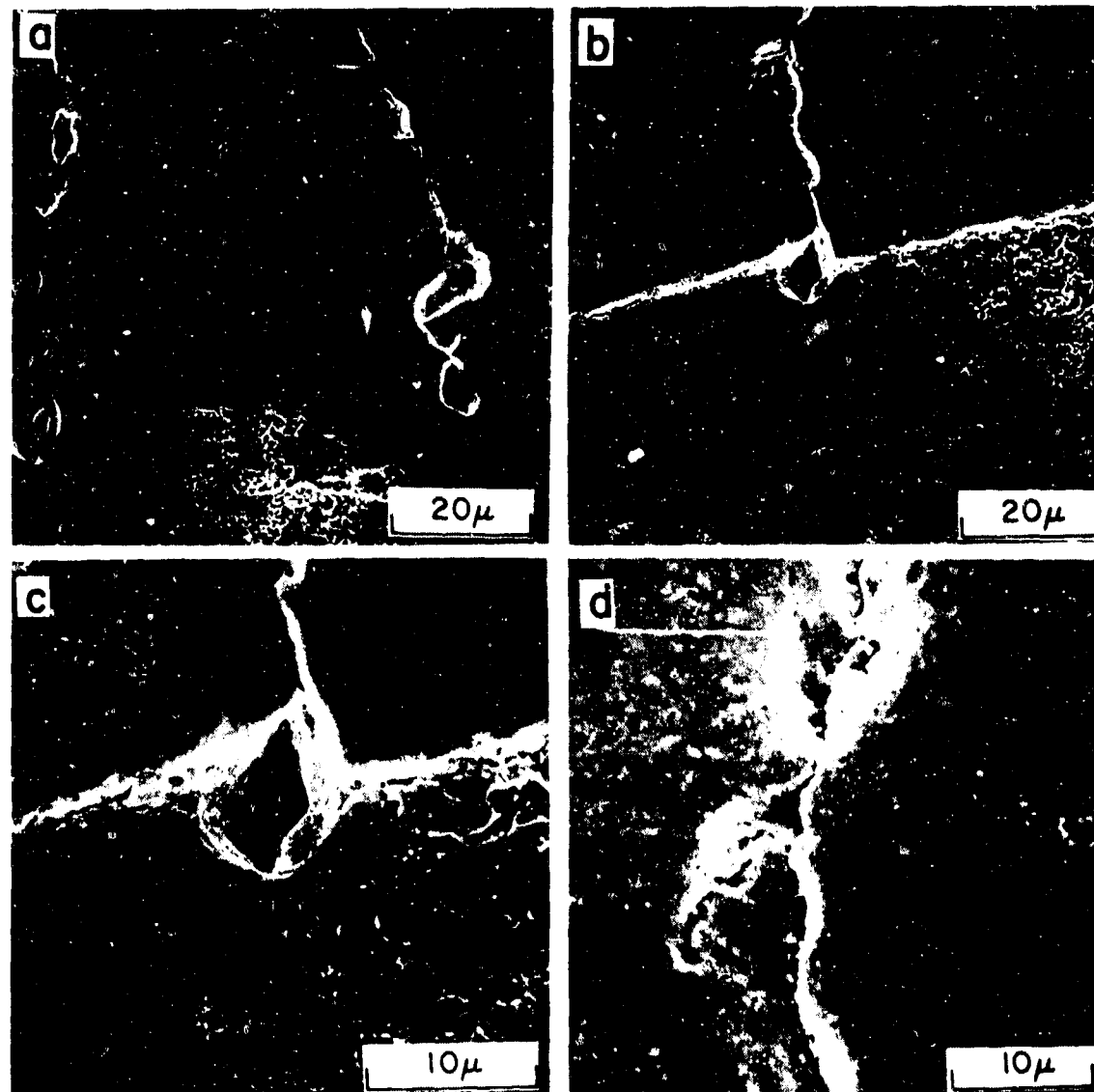


Fig. 63 Scanning electron micrograph of electropolished section of specimen BR at Co/steel interface showing crack blunting in steel. Co on top.

6.4 b

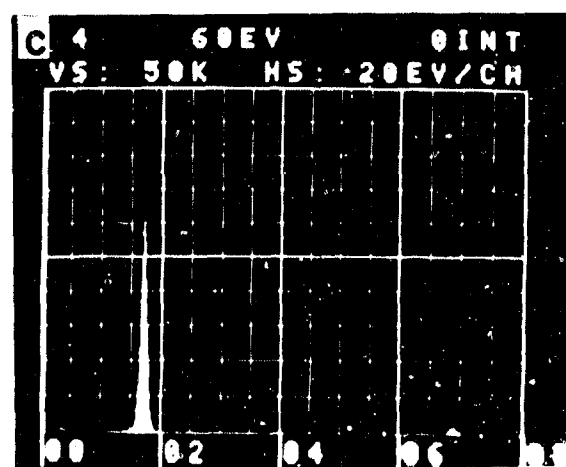
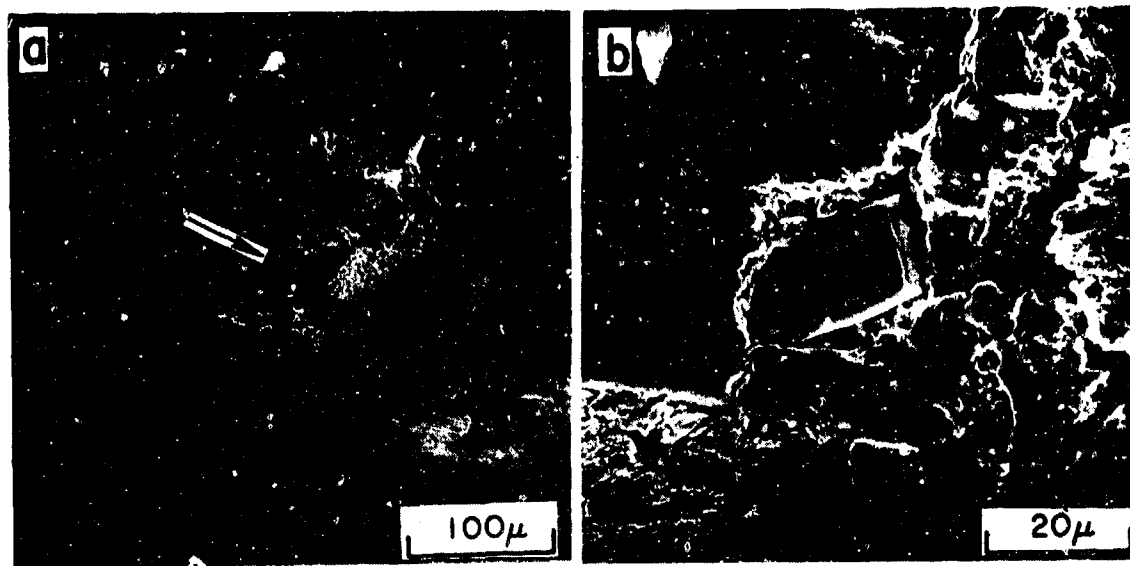


Fig. 64 Scanning electron micrographs of electropolished section and fracture surface of specimen BR at region of massive tear in the steel. Particle at arrow in (a) is silicon as shown by x-ray analysis (c).

64-C

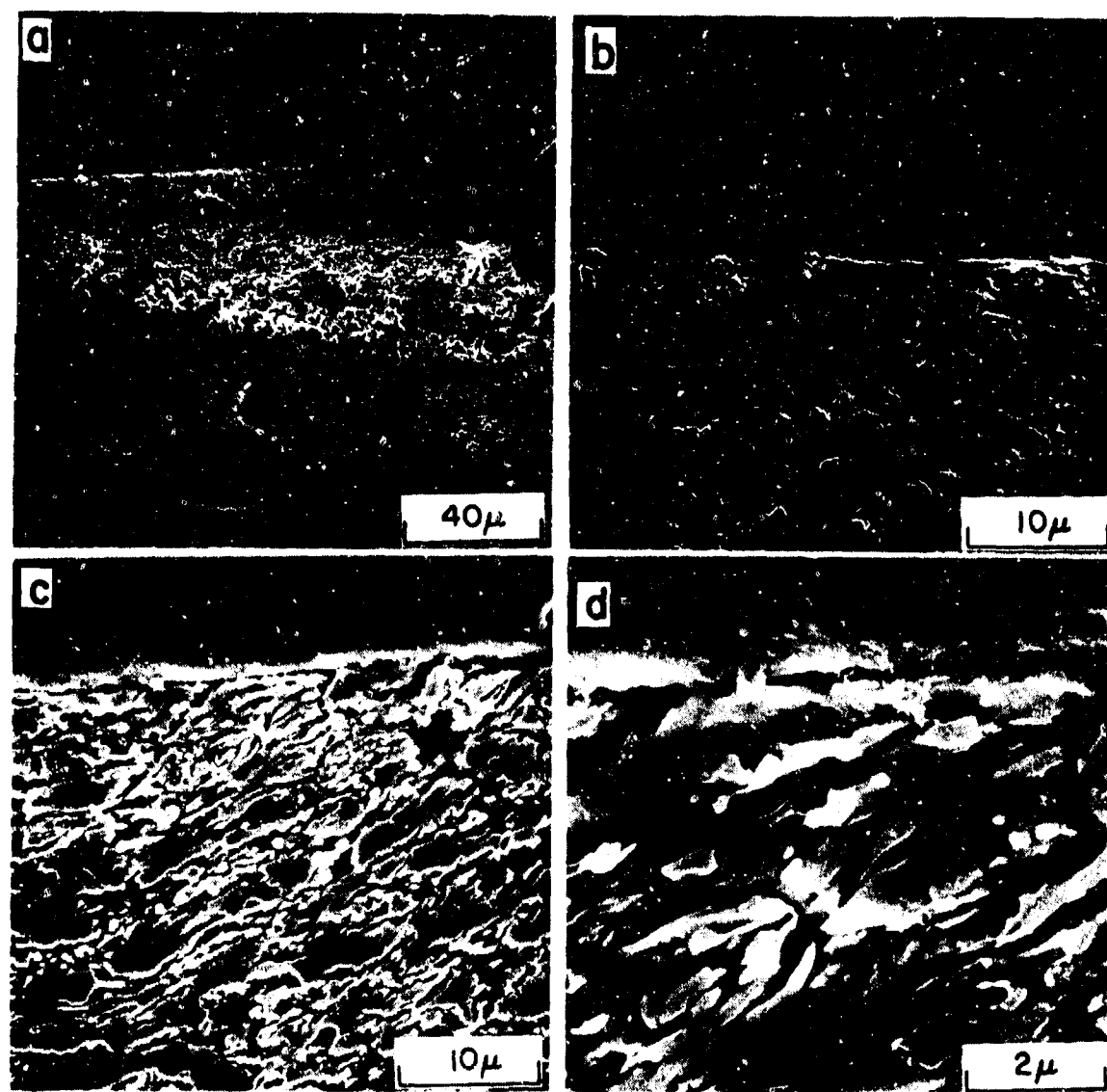


Fig. 65 Scanning electron micrographs of magnified region of tear in Fig. 64.

64-d

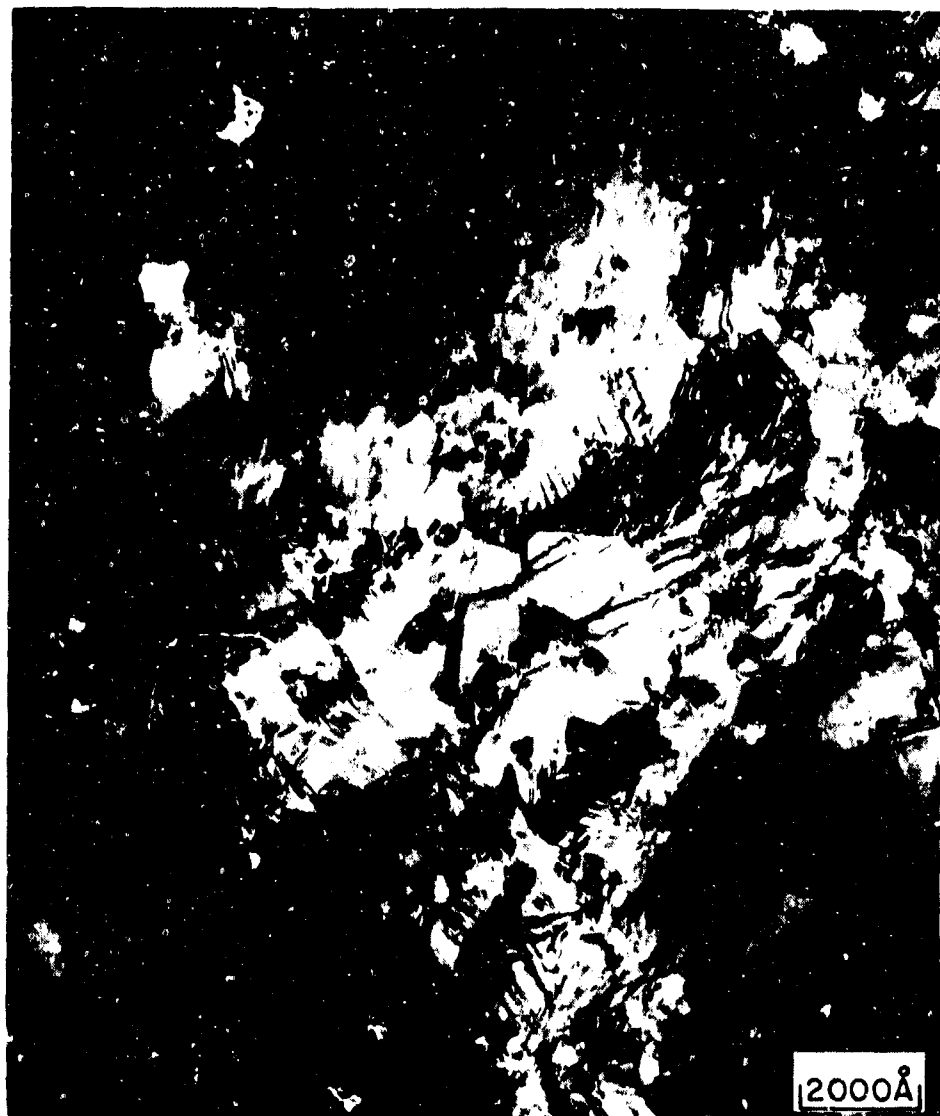


Fig. 66 Transmission electron micrograph of Co at Co/steel interface of specimen BR.

64-21

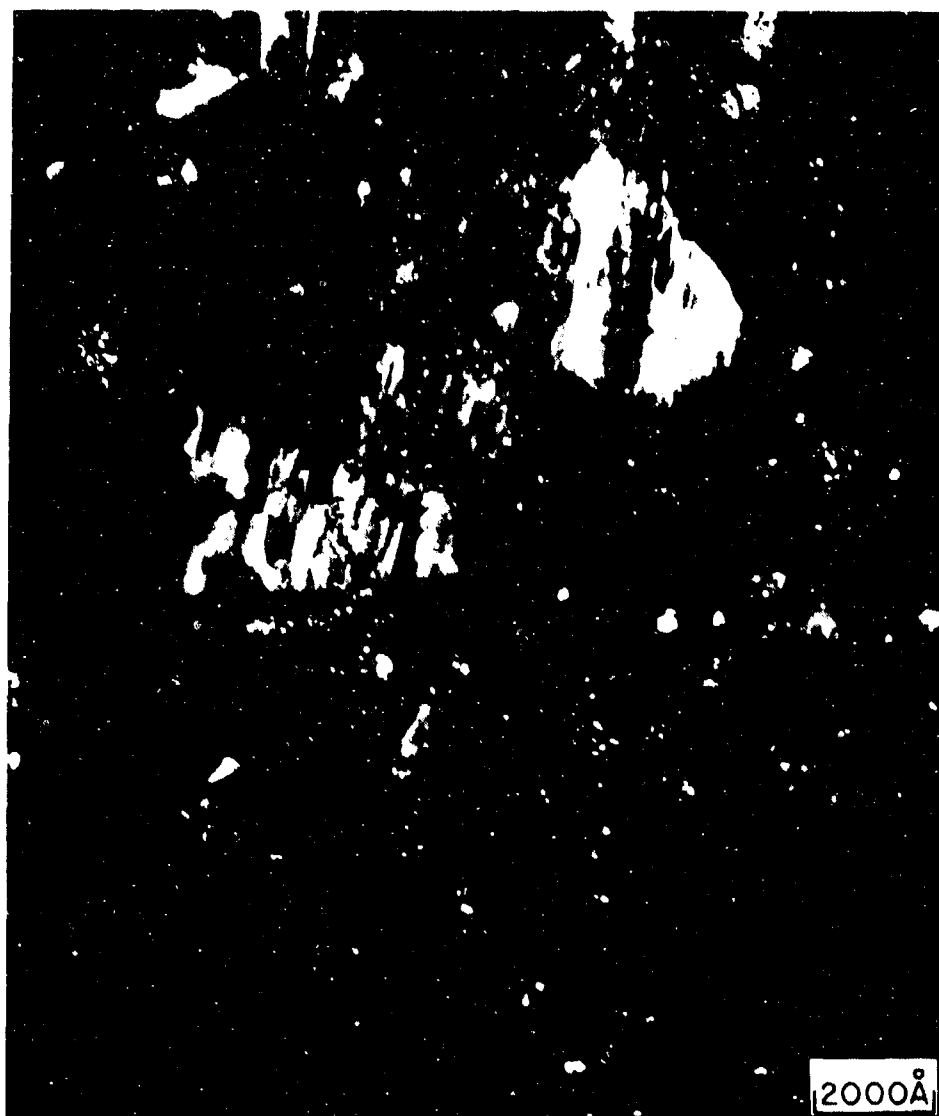


Fig. 67 Dark field micrograph corresponding to Fig. 66.  $\text{Al}_2\text{O}_3$  particles are illuminated.

64-f

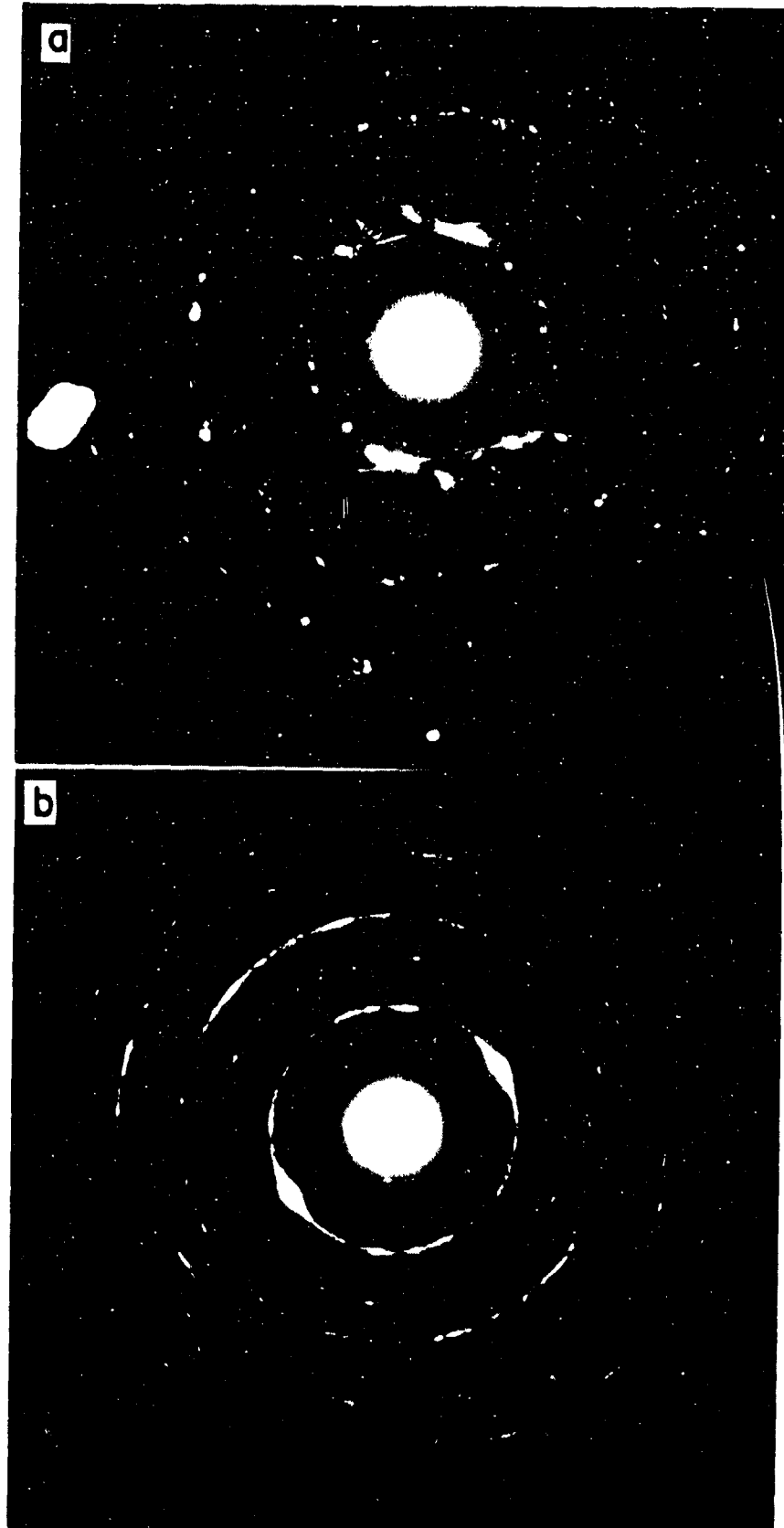


Fig. 68 Electron diffraction patterns: a) of Co at Co/steel interface of specimen BR; b) representative for Cr for specimen BR.

6.4-*g*

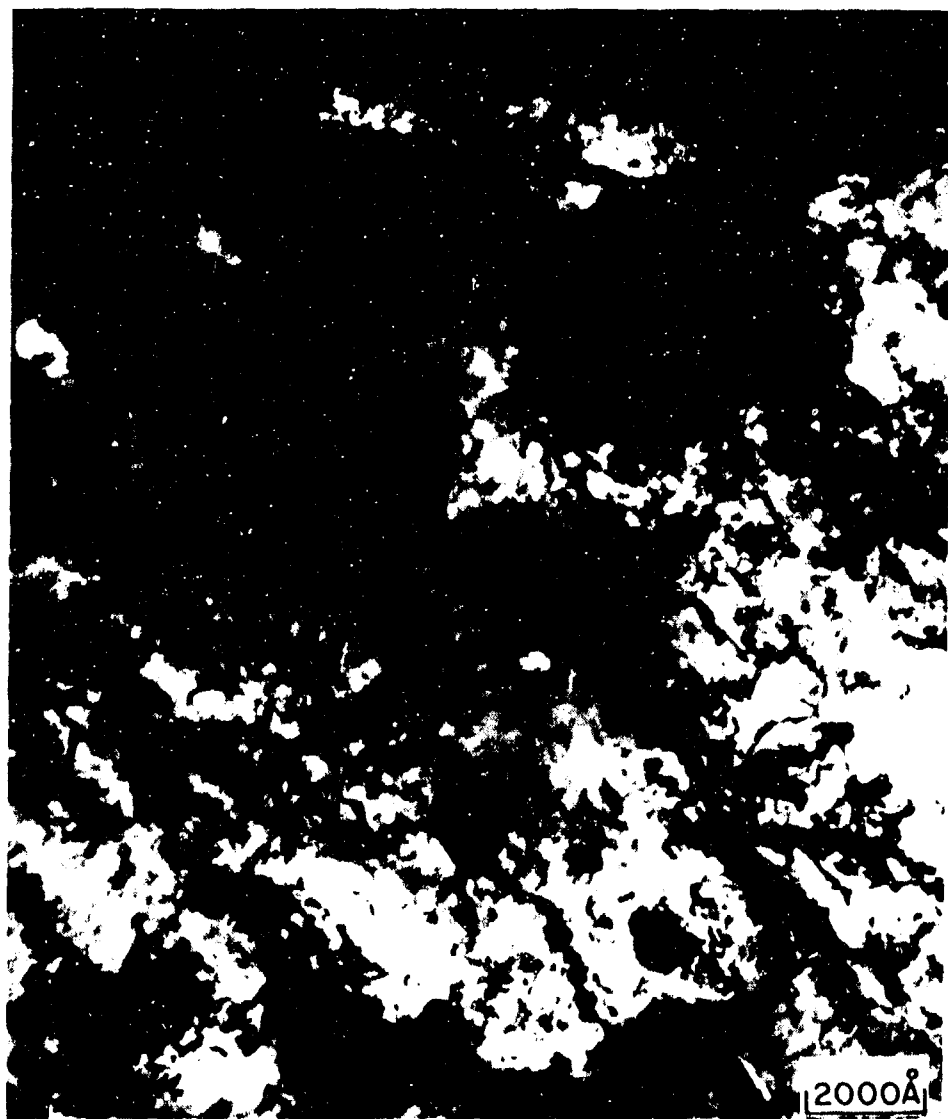


Fig. 69 Representative transmission electron micrograph of Cr on specimen BR.

64 h

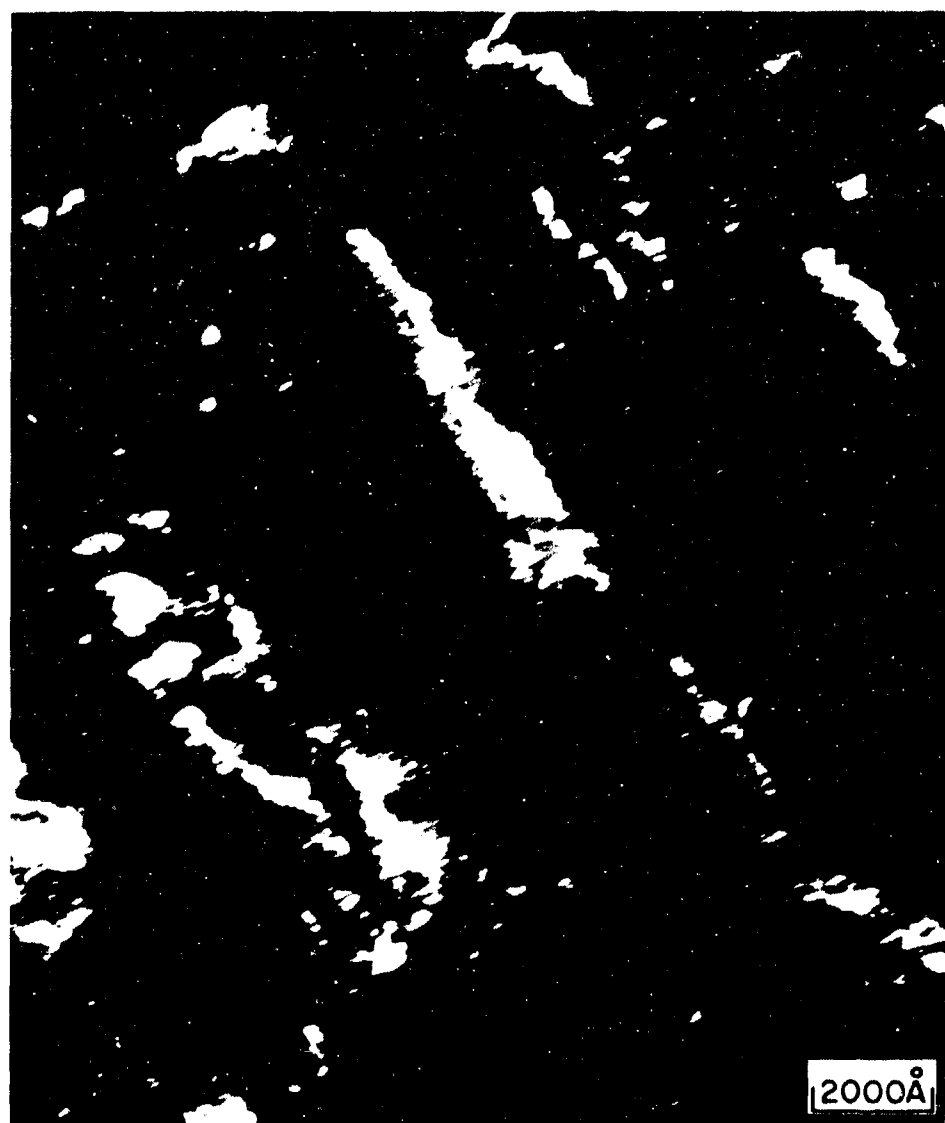


Fig. 70 Representative dark field micrograph of Cr of specimen Br showing columnar deposition structure.

successfully thermal fatigue tested over the temperature range of 600-1500°F and at nominal strains of 0.2% and 0.8%, respectively. Since tantalum-10 tungsten undergoes no phase transformations, its thermal expansion coefficient varies smoothly with temperature. The thermal fatigue cycle under constraint was very similar to that for steel cycled below  $A_1$ , for which an example is shown in Fig. 3. The parameters of the test results are presented in Table IX.

The test parameters for Ta-10W show several interesting effects. First, the total thermal fatigue life is quite sensitive to the applied strain. As the strain is increased from 0.2% to 0.8%, the life is reduced by a factor of 8. This result is consistent with the results found with steel. Second, since the high temperature strength of Ta-10W is quite high, quite large compressive loads are supported at the maximum test temperature. As can be seen from the last column of Table IX, the compressive loads at the highest temperature are nearly as large as the tensile loads at the lowest temperature.

The original microstructure of the Ta-10W is shown in section 3.2.1, Fig. 8. Microscopic observations of the microstructure, made during the later stages of writing this report, indicate that no marked recrystallization or other major microstructural changes occurred during the thermal cycling. Appreciable numbers of circumferential cracks were observed on both the inner and outer surfaces of the specimens. The final failure appeared to occur by propagation of a crack through the cross-section, principally from the inside surface. That this did not occur suddenly is shown by the fact that the load decreased quite markedly during the last few cycles before failure. Considerable microscopic work, including optical microscopy, scanning electron microscopy, and transmission electron microscopy, must be done to fully determine and document the failure mechanisms in this

TABLE IX

## Test Parameters for Tantalum-10 Tungsten Thermal Fatigue Tests

Specimens	Temp. Range (°F)	Cycle No.	Constraint (%)	Loads (1bs)	
				Tensile	Compressive
CI	620	4	0.19	1450	1175
	1535	70	0.17	1570	820
		129	0.17	750	300
Specimen fractured at start of cycle Number 130.					
CJ	605	1	0.75	1650	1350
	1530	8	0.75	1520	1200
		15	0.81	1280	1000
Specimens fractured on Cycle 16					

material. The limited observations made to date indicate that considerable progress could be made in understanding the failure mechanisms of this material with a moderate amount of further work.

#### 4. DISCUSSION

Several items are discussed in the following sections. These include a brief recapitulation of some of the experimental results, with some further interpretation and their interrelation. Suggestions of approaches to optimize erosion resistance of the plating/substrate combinations are presented, as well as some suggested direction for further work.

The items covered are: a discussion of chromium plate on steel; a discussion of composite cobalt-chromium plate on steel; some considerations with regard to the impact of test variables on the results, and the relation of these to gun barrel firing conditions.

##### 4.1 Chromium plate on steel.

4.1.1 Observations for Cr plate on gun steel. An alteration of near interface composition has been detected for this plating combination using transmission electron microscopy. Specifically, massive formation of  $\text{Cr}_7\text{C}_3$  in the Cr near the Cr/steel interface has been found in a specimen thermally fatigued through  $A_1$  and then above the  $M_s$  temperature. It is expected that a concomitant decarburization of the steel results at the interface. Aggregation of the metallic carbides in the steel near the interface has also been observed.

The process has also inferentially been identified as active for thermal fatigue through both  $A_1$  and  $M_s$ . This was concluded on the basis of preferential etching of electropolished sections of the test specimens. Comparison of preferentially etched zone sizes indicates that the region of alteration

is larger for cycling through both  $A_1$  and  $M_s$ . No altered zone is detected for specimens cycled below  $A_1$ , but could be present if quite shallow. These alterations are expected to significantly embrittle the interface region. The observations appear to be consistent with the diffusivity of carbon under the three thermal cycling conditions employed.

Some significant variations in cracking and associated deformation of the steel at the Cr/steel interface have been observed. Typically, when subjected to plastic strain during thermal fatigue, cracks in the Cr which blunt in the steel produce deformation in the steel which tends to undercut the interface. A rather subjective evaluation is that specimens cycled through  $A_1$  but above  $M_s$  fair slightly better in this regard, but a more direct measure of Cr adhesion under the test conditions employed would be required to test this claim. Additionally, for appropriate thermal fatigue conditions acceleration of the rate of cracking into the steel is observed which has the effect of moving the crack blunting stresses away from the interface and decreasing associated undercutting. Insufficient test data is in hand to establish if these observations are intrinsic to the strain and thermal cycling conditions imposed or if instead they are an artifact of specimen and plating geometry.

No significant debonding of the Cr from the steel has been seen for any of the test conditions employed. This suggests that, at least for gun firings in the several hundreds of rounds class, thermal fatigue as applied in the current test cannot alone be responsible for significant Cr erosion. The addition of impact projectile loading and associated shear forces could, however, provide the additional requisite insult to the material to hasten erosion.

Zones defined by bands of deformation have been observed in the Cr for all thermal fatigue test conditions with the exception of free expansion on unheat-treated 4340 steel. In regions of total fracture of the Cr it appears that the weaker deformation zone boundaries participate in the fracture. In no case has this led to significant chipping of the Cr for the test conditions employed, however.

#### 4.1.2 Cr Plate Analysis, Suggestions and Future Work.

Three degradation phenomena are identifiable for the Cr/steel combination: a) interface decarburization of the steel and formation of  $\text{Cr}_7\text{C}_3$ ; b) undercutting due to crack blunting at the Cr/steel interface; c) general deformation in the Cr in addition to cracks generated in electro-depositing the Cr. The structural degradation due to chemical changes at the Cr/steel interface would seem to be the ultimate weak link for this plating combination. Without changing materials, only lowering the peak steel temperature below  $A_1$  by greatly increasing Cr thickness would appear to have any real chance of success in reducing this effect. Ultimate success then hangs on the thermal/mechanical stability of thick Cr layers, untested in this work.

Operation at steel temperatures exceeding  $A_1$  but above  $M_s$  would appear to buy nothing in this regard as it matters little if a weak link is 0.5 mils thick or 5 mils thick - it's still a weak link. This problem may also be present even for fatigue below  $A_1$ . The insertion of a diffusion barrier between the Cr and steel could provide significant interface protection. Cobalt is, of course, a prime candidate and this concept is therefore discussed in the Cr/Co plate section.

Jockeying of the local interface stress constraints by such expedients as lowering the  $M_s$  temperature of the steel to 1) decrease the impact of crack blunting or 2) to promote through cracking of the interface - if acceptable by gun tube life requirements - might buy increased coating life. It would be a must, however, to quickly establish how dependent the interface cracking and deformation measurements are on specimen configuration and test condition, as the data must be used to design gun barrels not thermal fatigue specimens. A related option would be to try a soft steel liner between the gun steel barrel and the Cr. This is suggested by the results of one test made for Cr plate on unheat-treated 4340 steel which showed no interfacial damage. The thermal cycling was unconstrained, however, so further investigation of this is necessitated.

A third point of attack would be to reduce deformation of the Cr layer. Again the most effective approach is likely to be the insertion of an intervening Co layer. This is discussed in the next subsection.

To summarize points for future work:

1. The presence of an interfacial chemical alteration at the Cr/steel interface observed in our tests should be verified using fired gun tubes. If present, this alteration undoubtedly is the chief factor in controlling erosion resistance of Cr plate on steel and limits alternatives for further optimization of this combination.
2. The options of using thick Cr plate layers to lower the Cr/steel interface temperature and, hopefully, eliminate the interfacial chemical alteration should be considered. To support this:
  - a) The Cr/steel interface of plated specimens thermally fatigued at temperatures below  $A_1$  should be examined

using transmission electron microscopy to determine if an altered layer of reduced thickness is present.

- b) If the test in (a) is positive the rationale for using thick Cr layers is gone.
- c) If the test in (a) is negative thick plated Cr on steel should be thermally fatigue tested to see if any unexpected new degradation mechanisms are associated with the thick plate.

3. A second option is to attempt to change the Cr/steel interfacial constraints so as to either reduce interface undercutting due to crack blunting at the interface or to promote rapid cracking through the interface. Insufficient testing has been done to clearly define the alternatives but it is suggested that both

- a) Lowering the steel  $M_s$  temperature
- b) Use of a soft steel liner under the Cr

should be examined for their consequences.

If the test in 2(a) is positive none of those measures are likely to produce a major increase in resistance of Cr plate on steel to erosion, but they could be of significance in parallel with the use of thick Cr plate if 2(a) is negative.

4. Introduction of a diffusion barrier between the Cr and steel could provide protection from chemical attack at the interface and simultaneously give a better thermal match to reduce the stress experienced by the Cr. This is discussed further in the following section on the Cr/Co plating combination.

#### 4.2 Cobalt-Chromium plate on steel.

4.2.1 Observations on the Cr/Co plate combination. The major potential degradation mechanism for the Cr/Al<sub>2</sub>O<sub>3</sub> dispersion hardened Co combination is delamination of the Co. The delamination observed in this investigation has been attributable to nonuniformities in the deposited Co layer associated with fluctuations in the content of Al<sub>2</sub>O<sub>3</sub> with layer thickness. Other potential sources for delamination cannot be excluded, however, as void chains lying in the plane of deposition have also been seen in sections through the plate. While such void formation has definitely been associated with crack tip stress fields in certain instances they are also known to exist in the as plated material.

Uniformity of Al<sub>2</sub>O<sub>3</sub> distribution and Al<sub>2</sub>O<sub>3</sub> content are found to have a significant effect on deformation of and crack propagation in the Co layer. Significant deformation is seen in the Co at the Cr/Co interface if the Al<sub>2</sub>O<sub>3</sub> distribution is locally aggregated such as occurs in the absence of ultrasonic agitation of the deposition bath during plating, or if the Al<sub>2</sub>O<sub>3</sub> content at the interface is low. These deformation zones are seen both in conjunction with cracks in the Cr blunted at the interface and cracks which have penetrated the interface for a short distance. Particularly in the case of the non-ultrasonically deposited Co, voids are found to have formed in the sub Cr/Co interface deformation regions. For the non-ultrasonically deposited Co, principal sites of void formation are at the point of localized aggregation of the Al<sub>2</sub>O<sub>3</sub>. A comparison of sub Cr/Co interface degradation for the non-ultrasonically deposited Co with that for Cr plate on steel thermally fatigued under the same condition suggests that the Cr/Co

combination may actually be inferior to the Cr/steel combination in that it is more sensitive to Cr layer undercutting. This is not the case if  $\text{Al}_2\text{O}_3$  content is high and uniform, such as can be achieved with ultrasonic agitation during Co deposition. In this instance, no significant deformation is seen in the Co at either interface (Co/Cr or Co/steel) after extended thermal fatigue.

No degradation at either interface is seen which can be attributed to chemical activity or to differential thermal expansion. Unlike the Cr/steel, in the absence of cracking through the interface no interfacial region degradation is detected. The steel (4340) at the Co/steel interface is found to fail by tearing rather than cracking after a crack through the Cr and Co has reached the interface. This requires considerable total deformation of the steel substrate and even then the consequential degradation of the steel under the Co, at the point of crack entrance into the steel is small as compared to a similar situation for Co/Steel.

Crack propagation direction through the Co is found to be sensitive to gradients in the  $\text{Al}_2\text{O}_3$  content in the Co layer. Such gradients may therefore tend to act as crack stoppers in the Co as do other laminated structures particularly designed for such a purpose. Unfortunately such layered structures also increase the probability for the occurrence of delamination.

Insufficient data are at hand to define the dependence of Co properties upon deposition conditions and the initial surface properties of the steel, or to define the dependence of the quality of the plated Cr layer on the condition of its Co substrate. One observation suggests that, at least for a moderately low  $\text{Al}_2\text{O}_3$  content in the Co, the frequency of interfacial

cracking in the Cr at the Cr/Co interface, due to plating stresses, is higher than for Cr on steel. Effect of both Co surface roughness and  $Al_2O_3$  content on this cracking parameter needs further exploration.

There is also evidence that for the same thermal fatigue environment there is less significant deformation of the Cr for the Cr on Co combination than for the Cr on steel combination. Cr thickness may also be a factor here, however, in that the Cr on steel was 4-5 mils thick and the Cr on Co/steel only 1.5 mils thick. This observation also requires further clarification. An unexpected infolding of the cracks in the Cr into the Co at the Cr/Co interface has been seen for a specimen thermally fatigued at temperatures above  $A_1$  and below  $M_s$ . The cracks in the Cr are effectively blunted by this process. The deformation mechanics of this blunting process also requires further investigation.

As a final note, the last Cr/Co test specimen was run while this report was being prepared. Consequently, no complete failure analysis is available. It appears, however, that massive Co debonding and delamination occurred for the specimen in a relatively short number of cycles. As it happened, the last Alon C  $Al_2O_3$  powder on hand at the Science Center was used to plate this specimen, and as there was not quite enough Alon C, about 1/3 of the  $Al_2O_3$  added to the bath was from another batch simply marked "Alon." Although a discussion with the manufacturer seemed to indicate that this was indeed Alon C, the density of the two powders were obviously different. The resulting plating was not of uniform quality and this, then, is thought to be the cause of the quick demise of the plate. This observation as to type of  $Al_2O_3$  powder and its effect on Co integrity also deserves further investigation.

4.2.2 Cr/Co Plate Analysis, Suggestions and Future Work. It is clear that there is a greater potential for improvement of the Cr/Co/steel combination than for Cr plate on steel. The essential fault of the Cr/Co combination to be overcome is Co delamination. If this is successfully accomplished then several options are available for design of the Cr/Co/steel structure that can be expected to lead to major improvements in the erosion resistance of Cr/Co. Several potential sources for Co delamination can be identified including those that indirectly could effect delamination by altering Co deposition properties. These are:

1. Nonuniformities in  $\text{Al}_2\text{O}_3$  density forming a layered Co/ $\text{Al}_2\text{O}_3$  structure.
2. Void formation intrinsic to the plating process.
3. Variations in plating parameters during plating such as plating current, ultrasonic deposition conditions, etc.
4.  $\text{Al}_2\text{O}_3$  powder type and quality.
5. Quality of steel substrate (surface roughness, etc)

It is suggested that controlled thermal fatigue experiments can be performed to evaluate the effect of each of these factors in turn and in concert. This would require a combination investigation of plating processes and thermal fatigue and should include a study of simulated swaging of the Co to reduce as plated voids.

In any further work it is recommended that codeposition of Co and  $\text{Al}_2\text{O}_3$  without ultrasonic agitation of the plating bath be abandoned. On balance ultrasonic deposition yields clearly superior results and future effort should concentrate on removing any bugs associated with this approach.

At least three approaches to Cr/Co design with completely different rational can be considered:

### 1. Ultra thin Co-plate

The idea here is to use Co/Al<sub>2</sub>O<sub>3</sub> simply as a diffusion barrier to carbon, to stop the chemical reactions at the Cr/steel interface. It is expected that this layer would essentially not effect the deformation mechanics and cracking at the interface and as such could permit successful application of the techniques mentioned in the previous section for Cr/steel. To summarize the concept:

- a. Put an ultra thin layer of Co/Al<sub>2</sub>O<sub>3</sub> between the steel and the Cr to stop carbon diffusion. Localized carbon diffusion at cracks should not have a major effect in this case.
- b. Adjust the steel properties (as suggested in the Cr section) to minimize steel undercutting.
- c. Rely in part on the reduced Co thickness to decrease the tendency for Co delamination and make the job of effecting a Co plating procedure to eliminate delamination easier.

A combination plating and thermal fatigue testing series would be required to optimize the approach and would concentrate on defining Co thickness required to stop the carbon diffusion and the best approach to prevention of tendency to delamination of the Co at that thickness. Any success with decreasing steel undercutting would be just an additional bonus. Co plating thickness would likely be on the order of microns.

### 2. Thin Co plate.

The concept here is to use a thin Co Al<sub>2</sub>O<sub>3</sub> plate to simultaneously tailor the deformation at the Cr/Co and Co/steel interfaces to minimize

overall degradation due to cracking due to deformation associated with both the steel and the Cr. The problem with chemical attack is automatically taken care of. Questions to be answered to make this approach successful are as follows:

- a. Why is the deformation seen in the Cr on Co less than that seen for Cr on steel and what Co thickness plus  $Al_2O_3$  content will minimize this deformation?
- b. What is the optimum procedure to reduce uncercutting in the steel at the Co/steel interface at the point of intersection of a crack in the Co with the interface? Is it perhaps advisable to gradually reduce the  $Al_2O_3$  content in the Co layer as one approaches the steel so as to allow the Co to carry more of the deformation load?
- c. What is the Co cracking behavior if an  $Al_2O_3$  gradient is employed? Concomitant with this investigation would be the parallel study previously mentioned to defeat Co delamination. Co thickness for this approach would likely be less than 1 mil.

### 3. Ultra-thick Co layer

The concept here is to use an ultra-thick Co/ $Al_2O_3$  layer as a crack trap, i.e., to stop the majority of cracks passing through the Cr into the Co before they get into the steel. Evidence from the present study is that only a small fraction of the cracks in the Cr penetrate through the Co to the steel after several hundred cycles for a Co layer thickness of 6 mils. Questions to be answered include:

- a. For a constant  $\text{Al}_2\text{O}_3$  concentration how does crack propagation rate depend on Co layer thickness and applied temperature range and strain?
- b. What approaches such as gradients in  $\text{Al}_2\text{O}_3$  concentration are effective in slowing crack propagation?
- c. Most importantly, can Co delamination be defeated with ultra-thick Co?

It is the writer's conclusion, that on balance, method 2 has the best chance of success in that it retains some of the advantages of approach 1, adds new advantage and still gives a reasonable chance of coping with delamination. Again, on the basis of the delamination consideration approach 1 would appear to be the next most likely to succeed.

#### 4.3 Test Interpretation and Future Procedures.

The thermal fatigue tests that were conducted at the Science Center were not intended to be a simulation of a gun barrel firing cycle. Therefore one cannot expect and should not attempt to use these test data to calculate coating lifetimes. The testing did produce, however, several stringent environmental conditions that are of comparable severity in magnitude to those encountered in a typical gun firing cycle. The materials tested were those presently being used or contemplated for gun weapons, namely gun steel and chromium plated gun steel as well as tantalum-10 tungsten, and chromium over alumina-dispersed cobalt on gun steel. The temperature test ranges spanned the ~~temperature~~ gamut likely to be of importance to plated steels, and the stresses and strains encountered in the thermal fatigue cycling utilized are typical for a gun firing cycle.

The test parameters used put the tested materials through a rigorous thermal fatigue environment that can be expected to bring on many of the coating degradation and failure mechanisms that actually occur in gun firing. Furthermore this stringent test environment was applied in a well controlled manner. Consequently, although one cannot use the results to calculate coating life times for a particular gun system, the tests do give insight into major mechanisms controlling erosion and permit a measure of confidence in comparing their relative importance. It also offers a design tool which can be used to give a first test of approaches to coating optimization.

There are several approaches to modification of the thermal fatigue test environment as conducted at the Science Center which could be employed to more closely match the severity of gun firing environments while retaining complete control of the test environment. The rationale for these approaches is outlined below.

As one option the rate of temperature rise and concomitant strain rate can potentially be increased over that used in this effort by as much as a factor of 10. This would still be about a factor of 100 below rates typical for gun firings. Investigation of degradation as a function of temperature rise time might, however, give enough insight to permit a measure of extrapolation to higher rates for any rate sensitive degradation mechanisms identified.

As was noted in the results, sections 3.4.1 and 3.4.5, the strain range applied during the thermal cycle has a major effect on the thermal fatigue life. Because of time limitations it has not been possible to make a systematic study of the effect of strain range on the failure mechanisms. The

lower strain range tests gave longer specimen lives, and some of the differences in degradation observation may be due to longer exposure times rather than to strain range itself. A series of tests at various strain ranges with interruptions at intermediate points for evaluation would be required to separate the strain range from exposed time effects.

Another potential test variable that has not been examined during the current investigation is the effect of complex multiaxial stress states on the plating degradation mechanisms. In a barrel the internal surface containing the plate is highly constrained by the bulk of the gun tube. The inner surface is also subjected to a high normal stress due to the firing pressure as well as shear and impact stresses due to the motion of the projectile in the tube. The current thermal fatigue tests were performed using an applied uniaxial stress state. The only complex part of the stress present arose due to differential thermal expansion between the plated layer and the substrate material. It would be possible to increase the complexity of the stress state by flexing the specimen in torsion while it is being strained in tension. A straight forward modification of the test apparatus could be used to carry out tests under this more complex state of stress and strain.

In summary, the following suggestions for further tests address approaches to answer some unresolved questions relating to the present test results and to provide an expanded test environment for future efforts.

1. Thermal fatigue tests could be performed at heating and cooling rates that are much higher and much lower than those used in the present work and resulting data used to extrapolate degradation mechanism evaluation to faster rise times if indicated.

2. A systematic study of the effect of strain range on degradation mechanisms could be conducted with the strain ranging from tensile strain at high temperature through zero strain (free expansion) through compressive strain at high temperature.
3. Tests could be performed with the specimen flexed in torsion while simultaneously being strained in tension or compression. The two stresses could be applied at the same frequency, or the torsion could be applied statically, as well as at a much higher frequency than the axial load to sort out coupling effects between the two stresses.

## 5. CONCLUSIONS

This investigation has produced several conclusions which can have a significant impact on future efforts to further optimize the erosion resistance of two gun barrel coating materials. These are the chromium plate on gun steel currently in standard use by the U.S. Army and the composite chromium on dispersion harden cobalt coating material under consideration. The major conclusions of this work follow.

### 5.1 Bare Steel.

Bare steel has been observed to fail by cracking from the internal specimen surface when thermally cycled at temperatures below 1340°F. If the cycling is done in a temperature regime where the steel is entirely austenitic, specimen failures occur by crack propagation from the outer surface or by general necking of the cross-section. These observations provided an essential basis for interpretation of the test results of the plated steel specimens discussed in the two following subsections.

### 5.2 Chromium Plate on Steel.

1. Chemical changes have been detected at the chromium/steel interface as a consequence of carbon diffusion from the steel into the chromium. The consequence is the formation of Cr<sub>7</sub>C<sub>3</sub> in the chromium and a partial decarburization of the steel. The projected result is an embrittlement of the interface region, which is expected to be the ultimate limiting factor in the resistance to erosion of chromium plate on steel. This phenomenon has been verified only for thermal fatigue environments for which the temperature of gun steel exceeds 1340°F.

2. It is suggested that this observation be confirmed using actual fixed chromium plated gun tubes and that furthermore a test be made for the same effect, for thermal fatigue at steel temperatures somewhat less than 1340<sup>0</sup>F. If present for this temperature range the chemical alteration is expected to practically eliminate options for any major improvement of the erosion resistance of chromium plate.
3. In the advent that no alteration is seen for steel operational temperatures somewhat below 1340<sup>0</sup>F a remaining option would be to utilize ultra-thick chromium plating to lower the peak temperature seen by the bulk of the steel during gun firing. This, then, could be used in conjunction with steel treatment measures to decrease the sensitivity of the steel to undermining; an approach suggested by the results of the current effort.

### 5.3 Chromium/dispersion hardened cobalt plate on steel.

1. Further attempts to perfect this composite coating for the case of codeposition of the cobalt with alumina in the absence of ultrasonic agitation of the deposition bath should be abandoned in favor of the ultrasonic approach. The use of ultrasonic agitation is seen to have significantly better ultimate potential in providing erosion resistant coatings.
2. Delamination of the cobalt is the major degradation mechanism to be dealt with for this coating system. Several options and future work in this direction have been recommended.
3. Undercutting in the cobalt and steel is minimal when alumina content in the cobalt is uniform and high.

4. Three design options for the chromium/dispersion hardened cobalt coating combination have been suggested, each based on a different design rationale as identified by results of this study. These can be associated with the thickness of the cobalt layer required for each. Different approach to final optimization will be required for each option. In the most probable order of success they are as follows:

- a) Thin-cobalt layer (probably less than 1 mil) to simultaneous minimize crack tip related deformations in both the steel and chromium and the associated undercutting of the steel, and to stop chemical activity between the steel and chromium. An associated effort to defeat cobalt delamination would be required.
- b) Ultra-thin cobalt layer (probably on the order of microns) to stop chemical activity at the chromium steel interface. This option should require the least effort in dealing with cobalt delamination.
- c) Ultra-thick cobalt layer (probably in excess of 6 mils) to act as a trap for cracks and minimize crack penetration of the steel. This could require a major effort to deal with cobalt delamination.

#### ACKNOWLEDGMENTS

Thanks are extended to Dr. Fritz Sautter of Watervliet Arsenal, the contract technical monitor, for assistance in acquiring gun steel, for advice on setting up the electroplating baths and for plating some test specimens.

## APPENDIX A

## Diametral Extensometer Description

A quartz beam diametral extensometer has been developed for the purpose of controlling diametral strain of a metal specimen undergoing thermal cycling. A principal feature is the near absence of mechanical effects on soft materials at the point of contact with the extensometer.

The subject extensometer is an extensive modification of a device referenced in ASTM STP 465.

Two L-shaped quartz beams, hinged at "A" (see Fig. 1), are held against the gauge section of a cylindrical specimen by the spring force of a clip-on gauge. The contact edges of the quartz beams are ground to a 0.010-inch radius in order to eliminate errors due to any tipping of the plane of the extensometer. Cylindrical quartz shims, notched to accept the contact edges of the beams and of a diameter slightly greater than that of the specimen, distribute the load of the device and provide a response averaged over the length of the gauge section.

The extensometer is designed for use on a 0.25-inch diameter sample, but proper scaling would accomodate other sizes with no loss of sensitivity.

At the aft end of the beams is the clip-on gauge which responds to minute changes in sample diameter and which provides the key to the success of the extensometer.

The limiting factor in the use of this type of instrument on soft materials has been the force exerted by the bending of the arms of the clip-on gauge. Typical off-the-shelf gauges have bridge arms of steel

or titanium which measure 0.040-inch thick and 0.375-inch wide. When compressed to their working range they exert an unacceptably high load on the sample material. In some applications one may substitute an LVDT (a transformer with a movable core) which exerts no force on the sample. If, however, one is using a radio frequency generator for sample heating, as we are, the electrical noise induced in the LVDT is many times greater than the signal output.

As a consequence of the above, we have developed a clip-on gauge with a modulus of elasticity reduced by a factor of 100. The bridge arms are of Vespel, a thermoplastic polymer of high thermal and mechanical stability. The arms are thick, for high gauge sensitivity, and narrow to minimize the bending load.

The excitation voltage to the bridge strain gauges was reduced from the usual 10 VDC in order to reduce the  $I^2R$  heating not readily dissipated by the Vespel.

A simple, but extremely useful, change was made in the location of the bridge zeroing resistor, which was wired as an externally-located potentiometer. This provides a re-zeroing range approximately 10 times the usual working range, without physically disturbing the extensometer.

#### Specifications

Max. sensitivity:  $1.33 \pm 0.06$  volts/0.001 inch  
( $\sim 50 \mu$ inch noise level)

Linearity: <1%

Range: Real time  $\leftrightarrow \pm 10$  VDC/sensitivity  
with zero adjust  $\leftrightarrow 0.250 \pm 0.025$  in.

Drift: <50  $\mu$ inch/hour  
Response: 5 Hz  
Temperature range  
(of sample): 1500 $^{\circ}$ C

